Electronic Properties of Bi Nanowires

by

Stephen B. Cronin

B.S., New York University (1996)

Submitted to the Department of Physics
in partial fulfillment of the requirements for the degree of

Doctor of Philosophy

at the

MASSACHUSETTS INSTITUTE OF TECHNOLOGY

June 2002

Author .....
Department of Physics
May 3, 2002

Certified by .....
Prof. Mildred S. Dresselhaus
Institute Professor of Electrical Engineering and Physics
Thesis Supervisor

Accepted by .....
Prof. Thomas Greytak
Associate Department Head for Education

Electronic Properties of Bi Nanowires

by

Stephen B. Cronin

Submitted to the Department of Physics
on May 3, 2002, in partial fulfillment of the
requirements for the degree of
Doctor of Philosophy

Abstract

Transport properties are reported for Bi nanowires, which have been prepared by the filling of an alumina template with molten Bi. Lithographic processes are devised to pattern 4-point electrodes on single Bi nanowires that have been removed from the alumina template. High resistance non-ohmic contacts are attributed to a thick oxide layer formed on the surface of the nanowires. The non-linear 2-point $i(V)$ response of these contacts is understood on the basis of a tunneling model. Techniques are developed for making ohmic contacts to single bismuth nanowires through the thick oxide coating using a focused ion beam (FIB) to sputter away the oxide and then deposit contacts. By combining the FIB techniques with electron beam lithography we achieve contacts stable from 300K to 2K for nanowires less than 100nm in diameter. Annealing in H_2 and also NH_3 environments is found to reduce the oxide completely. However, the high tempertures required for this annealing are not compatible with the lithographic techniques. A method for preventing the burnout of nanowires by electrostatic discharge is developed. A lithographic scheme for measuring the Seebeck coefficient of a single Bi nanowire is devised. Techniques are also developed for measuring a single Bi nanowire inside the template. The electronic band structure of Bi nanowires is modeled theoretically based on the quantum confinement of electrons. 4-point resistivity data on single Bi nanowires are reported and understood on the basis of the theoretical model of the quantized electronic band structure and considering the wire boundary and grain boundary scattering not present in bulk bismuth.

Thesis Supervisor: Prof. Mildred S. Dresselhaus
Title: Institute Professor of Electrical Engineering and Physics

Acknowledgments

I would like to thank my parents Rosemary and Bill Cronin for providing an exceptionally strong foundation of love and support for me. I am forever grateful to them for never having pushed me to do well but instead encouraging me to pursue something I love and to do it with passion.

My six years at MIT have been the best years of my life. Being able to work in an environment with so many talented and enthusiastic people was a great pleasure. First and foremost I would like to thank my supervisor Prof. Mildred Dresselhaus for being a perfect mentor. Her broad aptitude and astonishing capacity were inspiring. The grace with which she handles an overwhelming amount of work and still manages to be continuously available for her students is truly exceptional. I also feel very fortunate to have worked with Dr. Gene Dresselhaus who was always able to point me in the right direction. I will never forget Gene's unique wit. Together the Dresselhaus' make an amazing team, and create a unique environment that has opened up a world of possibilities to me.

The Dresselhaus group has drawn a wide range of talented individuals during my years here. I met some of the most interesting people and I would like to thank them all for making MIT such an enjoyable experience; Dr. Xiangzhong Sun, Dr. Takaaki Koga, Yu Ming Lin, Marcie Black, Oded Rabin, Prof. Zhibo Zhang, Dr. Manyalibo Matthews, Dr. Sandra Brown, Dr. Alessandra Marucci, Prof. Marcos Pimenta, Dr. Ado Jorio, Dr. Antonio Souza Filho, and Dr. Hao Xin. I would especially like to thank Laura Doughty for all she has done for me and for her support over the years.

Most of the techniques in this thesis were not learned from a book, but from people, and it is them that I have to thank. I am grateful to many people who spent the time to explain their expertise to me; Dr. Gale Petrick, Prof. Jean-Paul Issi, Dr. Joseph Heremans, Dr. Theodore Harman, Dr. Jagadeesh Modera, Prof. Gang Chen, Dr. Pratibha Gai, and Dr. James Goodberlet. There are many technicians at MIT who did more than maintain equipment. Their care for science really showed through. Mark Mondol, Michael Frongillo, Kurt Broderick, Libby Shaw, and Dr. Fang-Cheng

Chou all had significant impact on my work.

Finally, I would like to thank all of my friends and family for providing support and encouragement over the past six years.

Contents

List of Figures

List of Tables

Chapter 1

Introduction

In this thesis we study the electronic properties of Bi nanowires with a particular focus on the measurement of the temperature dependences of the transport properties (resistivity, magnetoresistance and Seebeck coefficient) of a single Bi nanowire. The unique properties of bulk Bi make this system attractive as a fundamental investigation of classical and quantum size effects that are becoming more and more relevant to the semiconductor industry as devices become smaller and smaller.

The fabrication of nanowires inside porous alumina templates has recently become a very popular area of research. During the past few years researchers have filled these templates with a number of materials ranging from carbon nanotubes to superconductors to magnetic materials.

1.1 Why Bi?

Our motivation for studying the Bi nanowire system is based on the unique properties of bulk bismuth. Bi has the smallest effective mass of all known materials. As will be discussed in detail in chapter 2, components of the effective mass tensor are as small as $0.001m_e$. The small effective masses of Bi make it easy to observe the effects of quantum confinement. Because of the small effective masses in Bi, the energy separations between the subbands of the quantum energy levels are large. Inside a nanowire the energy bands split into subbands with the approximate energy separa-

tion $\approx \hbar^2\pi^2/m^*d^2$, where m^* and d are the effective mass and nanowire diameter, respectively. (This relation assumes isotropic masses and a square wire cross-section. More detailed calculations are given in chapter 2.) In Bi, the variations of these energy levels with diameter are large enough to induce a semimetal-to-semiconductor transition at a relatively large wire diameter, $\sim$ 50nm. This transition occurs because the conduction subbands are shifted to higher energies relative to the bulk bandedge, while the valence subbands are shifted to lower energies. When the subband shifts are larger than the band overlap between the conduction and valence bands in bulk Bi, there will be a bandgap between the lowest conduction subband and the highest valence subband, thus forming a semiconductor. Bi also has a very long mean free path ($\sim$0.4mm at 4K and 100nm at 300K), which makes the Bi nanowires a suitable system for the study of low-dimensional transport. Since the diameter of the nanowires is much smaller than the mean free path of the electrons, the electrons will feel the confinement of the boundary of the nanowire, thereby resulting in a reduction in mean free path as the wire diameter decreases.

In addition to the fundamental study of electron transport in the quantum limit, the Bi nanowires have been predicted to have a high thermoelectric efficiency. The enhancement is based on the sharp features in the one-dimensional density of states of the nanowires [1, 2], the increased boundary scattering of phonons which results in a lowered thermal conductivity, and the semimetal-semiconductor transition. Since bulk Bi is a semimetal, the coexistence of electrons and holes in Bi approximately cancel each other in the thermopower. In a semiconducting Bi nanowire, however, nanowires can be made n and p type, thus eliminating this cancellation. Bismuth on a one carrier basis has been predicted to be an excellent thermoelectric material [3].

1.2 The Importance of a Single Nanowire Measurement

The Bi nanowires, as will be discussed in chapter 3, are prepared in the pores of a host alumina template. Transport measurements of this composite do not yield any quantitative information about the resistivity of the nanowires since the number of nanowires contributing to the transport is unknown. Instead, only the normalized resistance and magnetoresistance ($R(T)/R(300\text{K})$ and $R(B)/R(B = 0\text{T})$) can be measured, and not the absolute resistivity. The absolute resistivity can only be measured by determining the cross-sectional area and length of the nanowires and by eliminating the effect of the contact resistance. This can be done by performing a 4-point measurement of the resistance on a single Bi nanowire. In bulk and two-dimensional conductors, Hall effect measurements are the standard method for determining the carrier density and carrier scattering relaxation time. In a 1D conductor, however, Hall effect measurements are not possible and thus 4-point measurements are the most direct way of determining these extremely important quantities. In order to monitor the effects of doping and impurities quantitatively, 4-point measurements are essential. Also, the determination of the absolute resistivity is essential to evaluate the potential of bismuth nanowires for thermoelectric applications.

1.3 Outline of Thesis

This thesis is organized in the following fashion. In chapter 2 the quantized electronic band structure of Bi nanowires is derived. Chapter 3 discusses how the nanowires are made and how electrical contacts are attached to individual Bi nanowires using lithographic techniques. In Chapter 4 the 2-point $i(V)$ response of the electrical contacts to the nanowires is presented and understood on the basis of a tunneling model. 4-point resistivity data are presented in chapter 5 along with various strategies for removing the thick oxide layer to achieve ohmic contacts. In chapter 6, techniques for measuring the transport properties of a single Bi nanowire inside the alumina

template are developed. In the final chapter the results and achievements of this work are summarized and some suggestions for future work are made.

Chapter 2

Theory

In this chapter we present the very unique electronic band structure of bismuth. From this we calculate the density of electronic states in bulk Bi. By applying quantum mechanics to electrons confined to the nanowires we calculate the density of states for the electrons in Bi nanowires.

2.1 Band Structure of Bismuth

Bismuth is a semimetal crystallizing in the A15 rhombehedral structure [4] with a band overlap between the conduction band at the L-points in the Brillouin zone and the valence band at the T-point in the Brillouin zone. The Brillouin zone of Bi is illustrated in figure 2-1, showing the location of the electron and hole carrier pockets as indicated.

Perhaps the most striking feature of Bi is it's highly non-parabolic electronic energy bands at the L-points. These bands are mirror images of each other and are separated by a small energy gap, $E_g = 13.6meV$ at T=0K. It is the strong coupling between these L-point bands that gives rise to the non-parabolicity. As can be seen in figure 2-2 the L-point bands are only parabolic very close to the band edge. The

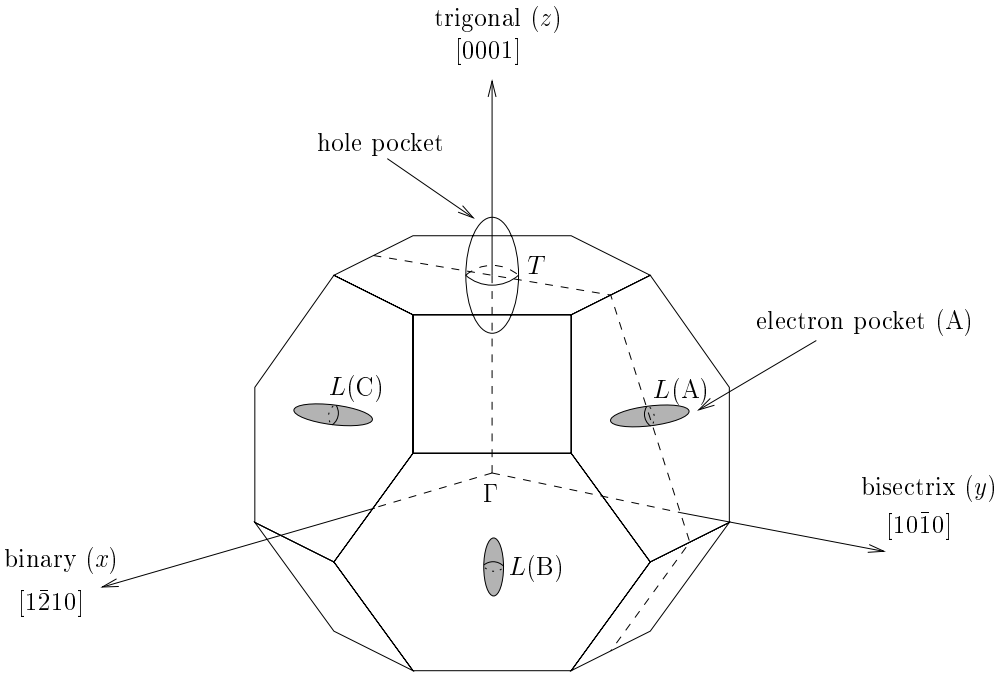

Figure 2-1: The Brillouin zone of Bi, showing the Fermi surfaces of the three electron pockets at the L-points and one T-point hole pocket.

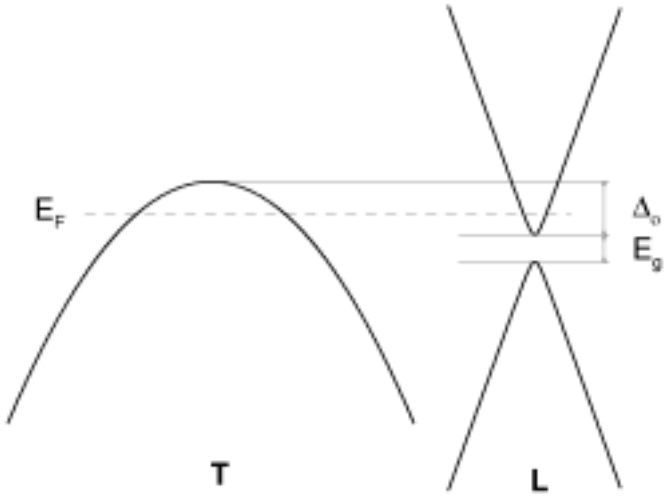

Figure 2-2: Schematic diagram of the Bi band structure at the L-points and T-point near the Fermi energy level, showing the band overlap Δ_0 of the L-point conduction band and the T-point valence band. The L-point electrons are separated from the L-point holes by a small bandgap E_{gL}. At $T = 0\,\mathrm{K}$, $\Delta_0 = -38\,\mathrm{meV}$ and $E_{gL} = 13.6\,\mathrm{meV}$ [5, 6].

dispersion relation for the L-point carriers is given by the Lax model [7]

$$E_L(\mathbf{k}) = -\frac{E_g}{2} \pm \frac{E_g}{2}\sqrt{1 + \frac{2\hbar^2}{E_g}\left(\frac{k_x^2}{m_x} + \frac{k_y^2}{m_y} + \frac{k_z^2}{m_z}\right)}. \tag{2.1}$$

Here the $-$ sign is for L-point holes and the $+$ sign is for L-point electrons, and E_g is the direct band gap at the L-point. The effective masses in this equation, m_x, m_y, and m_z, must be calculated from the effective mass tensors of Bi. For the carrier pocket labeled **A** in figure 2-1 the effective mass tensor is

$$\mathbf{M}_{\mathbf{e},\mathbf{A}} = \begin{pmatrix} m_{e1} & 0 & 0 \\ 0 & m_{e2} & m_{e4} \\ 0 & m_{e4} & m_{e3} \end{pmatrix}. \tag{2.2}$$

The effective mass tensors for the other L-point carrier pockets are obtained by rotating the effective mass tensor of pocket **A** about the trigonal axis by 120° and

Table 2.1: Effective mass components perpendicular and parallel to the nanowire axis for carrier pockets in Bi nanowires with various crystalline orientations at 77K. The z-axis is taken to be along the nanowire axis. This table was taken directly from [1, 2].

Mass Component		Trigonal	Binary	Bisectrix	(012)	(101)
e^- pocket A	m_x	0.1175	0.0023	0.0023	0.0029	0.0024
	m_y	0.0012	0.2659	0.0012	0.0012	0.0012
	$\tilde{m}_z$	0.0052	0.0012	0.2630	0.2094	0.2542
e^- pocket B	m_x	0.1175	0.0023	0.0023	0.0016	0.0019
	m_y	0.0012	0.0016	0.0048	0.0125	0.0071
	$\tilde{m}_z$	0.0052	0.1975	0.0666	0.0352	0.0526
e^- pocket C	m_x	0.1175	0.0023	0.0023	0.0016	0.0019
	m_y	0.0012	0.0016	0.0048	0.0125	0.0071
	$\tilde{m}_z$	0.0052	0.1975	0.0666	0.0352	0.0526
hole pocket	m_x	0.0590	0.6340	0.6340	0.1593	0.3261
	m_y	0.0590	0.0590	0.0590	0.0590	0.0590
	m_z	0.6340	0.0590	0.0590	0.2349	0.1147

240°. At T=0K the effective mass components of the L-point conduction band are $m_{e1} = 0.00118m_o, m_{e2} = 0.263m_o, m_{e3} = 0.00516m_o$, and $m_{e4} = 0.0274m_o$, where m_o is the free electron mass [8]. Notice the very high anisotropy of the ellipsoids, $m_{e2} \gg m_{e1}$, and the very small values of the m_{e1} and m_{e3} mass components. These small mass components lead to very large quantum bound state energies that will be discussed later in this chapter. The effective mass components perpendicular and parallel to the nanowire axis are calculated for nanowires with various crystalline orientations in reference [1, 2], and are listed in table 2.1.

In addition to being non-parabolic, most of the band parameters in Bi are strongly temperature dependent. The effective masses of the electrons and holes in the L-point bands vary by a factor of almost 6 between 0 and 300K, and are given by [9]

$$(\mathbf{m}_e(T))_{ij} = \frac{(\mathbf{m}_e(0))_{ij}}{1 - 2.94 \times 10^{-3}T + 5.56 \times 10^{-7}T^2}. \tag{2.3}$$

The large temperature dependence of the effective mass arises from the strong cou-

pling between the L-point conduction and valence bands. Since the L-point carriers arise from a very slight distortion in the crystal lattice from two inter-penetrating FCC lattices, the slight changes in the lattice constants due to thermal expansion affect the effective masses very strongly.

The direct bandgap at the L-point, E_g, also varies significantly with temperature [9]

$$E_g = 13.6 + 2.1 \times 10^{-3} T + 2.5 \times 10^{-4} T^2 \text{ (meV)}. \tag{2.4}$$

And finally, the energy overlap of the bands, Δ_0, varies as a function of temperature from -38 meV for temperatures below 80K to -104meV at 300K. The temperature dependence of this band overlap is given by [10]

$$\Delta_0 = \begin{cases} -38 \text{ (meV)} & (T < 80\text{K}) \\ -38 - 0.044(T - 80) & \\ +4.58 \times 10^{-4}(T - 80)^2 & (T > 80\text{K}) \\ -7.39 \times 10^{-6}(T - 80)^3 \text{ (meV)}. & \end{cases} \tag{2.5}$$

The T-point valence band is quite simple in comparison to the L-point bands. The T-point valence band contains one carrier pocket, which has its principal axis along the trigonal axis of the Brillouin zone. Its effective mass tensor is diagonal with the components, $m_{e1} = m_{e2} = 0.059 m_o$ and $m_{e3} = 0.634 m_o$ [6]. This is in contrast to the electron carrier pockets, which do not have their principal axes along the symmetry axes of the Brillouin zone. The T-point valence band is taken as parabolic with no temperature dependence.

2.2 Density of States of Bulk Bi

The density of states is central to all transport calculations. In this section we will derive expressions for the bulk density of states of the parabolic valence band and the non-parabolic conduction band. In the following section (section 2.3) we derive the density of states for Bi nanowires with discretely quantized states.

We will start by calculating the density of states of the bulk valence band since it is the most simple of the bands in Bi. We will then extend this approach to the non-parabolic conduction band of bulk Bi and then to the one-dimensional bands of Bi nanowires.

2.2.1 Parabolic T-Point Valence Band

Given a parabolic dispersion relation we consider an ellipsoid of energy E described by

$$E(\mathbf{k}) = \frac{\hbar k_x^2}{2m_x} + \frac{\hbar k_y^2}{2m_y} + \frac{\hbar k_z^2}{2m_z}. \tag{2.6}$$

The volume of this ellipsoid in k-space is

$$V_k = \frac{4\pi}{3} k_x^E k_y^E k_z^E, \tag{2.7}$$

where

$$k_i^E = \frac{\sqrt{2m_i E}}{\hbar}. \tag{2.8}$$

The total number states of this ellipsoid is equal to the total volume in k-space divided by the volume factor $(2\pi)^3/V$ (where V is the volume in real space) multiplied by a factor of 2 for the spin degeneracy

$$N(E) = \frac{4\pi}{3} k_x^E k_y^E k_z^E \frac{V}{(2\pi)^3} 2. \tag{2.9}$$

Plugging eq. (2.8) into (2.9) to eliminate k we get

$$N(E) = \frac{2\sqrt{2}V}{3\pi^2\hbar^3}(m_x m_y m_z)^{1/2} E^{3/2}, \tag{2.10}$$

and taking a derivative we get the three-dimensional density of states per unit volume

$$D(E) = \frac{1}{V}\frac{dN}{dE} = \frac{\sqrt{2}}{\pi^2\hbar^3}(m_x m_y m_z)^{1/2}E^{1/2}. \tag{2.11}$$

2.2.2 Non-Parabolic L-Point Conduction Band

For the L-point conduction band we have the non-parabolic dispersion relation given by the Lax model

$$E_L(\mathbf{k}) = -\frac{E_g}{2} + \frac{E_g}{2}\sqrt{1 + \frac{2\hbar^2}{E_g}(\frac{k_x^2}{m_x} + \frac{k_y^2}{m_y} + \frac{k_z^2}{m_z})}. \tag{2.12}$$

The volume in k-space at energy E is still given by

$$V_k = \frac{4\pi}{3}k_x^E k_y^E k_z^E, \tag{2.13}$$

however, now the wavevector is given by

$$k_i^E = \sqrt{\frac{2m_i}{\hbar^2}(\frac{E^2}{E_g} - E)}. \tag{2.14}$$

Plugging this expression into eq. (2.9), we get the total number of states for energy E

$$N(E) = \frac{2\sqrt{2}V}{\pi^2\hbar^3}(m_x m_y m_z)^{1/2}(\frac{E^2}{E_g} - E)^{3/2}. \tag{2.15}$$

Note that there is an additional degeneracy factor of 3 here to account for the multiple carrier pockets. Taking a derivative of $N(E)$ with respect to energy, we get the density of states for the non-parabolic L-point conduction band

$$D(E) = \frac{1}{V}\frac{dN}{dE} = \frac{3\sqrt{2}}{\pi^2\hbar^3}(m_x m_y m_z)^{1/2}(\frac{E^2}{E_g} - E)^{1/2}(\frac{2E}{E_g} - 1). \tag{2.16}$$

The energy dependence of the non-parabolic density of states, derived above, is quite different from the parabolic density of states of eq. (2.11). This difference can be seen in figure 2-3, where the density of states of the L-point conduction band and

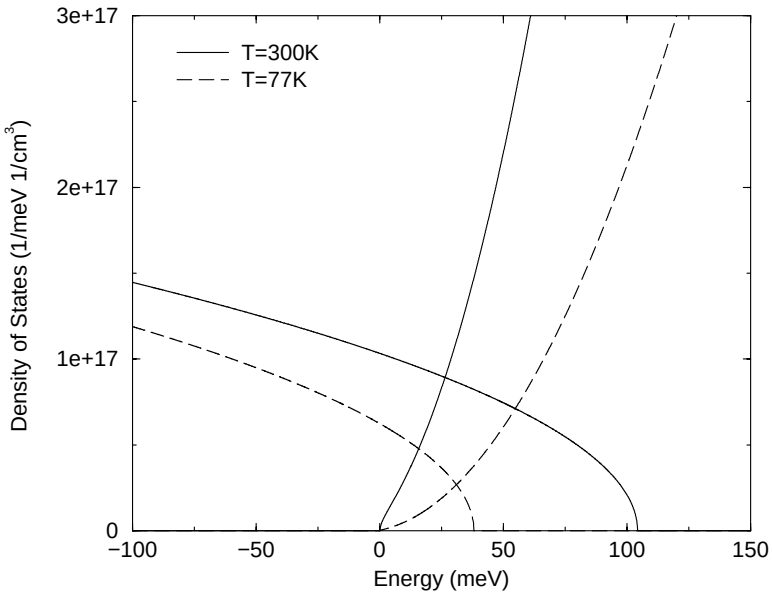

Figure 2-3: Bulk density of states of the L-point conduction band and the T-point valence band plotted together at both 77K and 300K. Note that the zero of energy is taken as the bottom of the L-point conduction band.

the T-point valence band are plotted together at both 77K and 300K.

2.3 Density of States of Bi Nanowires

Because of the very small effective mass components of Bi, the quantized energy levels of electrons confined to a nanowire, which go as $1/m^*$, can be quite large for relatively large wire diameters. Because of this, the density of states of the Bi nanowires are quite different from that of bulk Bi. In this section we derive expressions for the density of states in Bi nanowires.

2.3.1 Energy of the Quantized States in Bi Nanowires

In calculating the quantized subband energies of Bi nanowires we will assume that the nanowire is square in cross-section instead of circular. An analytical solution to the case of a circular wire cross-section is not possible because of the effective mass anisotropy in Bi. Detailed calculations for the Bi nanowires have been carried out

by Lin, *et. al.* [1, 2], assuming a circular wire cross-section by solving Schrödinger's equation numerically. However, for the following calculation we will assume a square wire cross-section, which will give reasonable results for the quantum energy levels and allow us to calculate many more subbands quickly. At the end of this section a comparison is made between the square wire and circular wire models.

As a convention, we take the nanowire axis to be along the z-axis. The effective mass components perpendicular to the nanowire, m_x and m_y, which determine the quantized energy levels depend on the crystalline orientation of the nanowire, and are given in table 2.1. Assuming a square wire cross-section the quantized bound state energies can be written in the simple form

$$\epsilon_{i,j} = \frac{\pi^2\hbar^2}{2a^2}[\frac{i^2}{m_x} + \frac{j^2}{m_y}], \tag{2.17}$$

where $i, j = 1, 2, 3....$ This result comes directly from solving Schrödinger's equation for a particle confined by an infinite potential. We take a to equal the nanowire diameter because, as will be shown in section 2.3.5, this assumption yields results that are in good agreement with those of a circular wire cross-section model.

The subband energies are shifted relative to the bulk band edges in Bi by the amount given in equation (2.17). For the conduction band the subband energies are shifted up and for the valence band the energy is shifted down. Since the lowest subband energy is non-zero, this quantization has the effect of splitting the conduction and valence bands apart. For a small enough wire diameter in Bi, this splitting is enough to transform the material from a semimetal to a semiconductor. The semimetal-to-semiconductor transition will be discussed in section 2.3.4.

2.3.2 Parabolic T-Point Valence Band

We treat each subband in the nanowire as a one-dimensional conductor. The density of states of a 1D subband can be derived from the dispersion relation

$$E(k_z) = \Delta_o - \epsilon_{i,j} - \frac{\hbar^2 k_z^2}{2m_z}, \tag{2.18}$$

where Δ_o is the energy of the bulk valence bandedge relative to the conduction bandedge (taken as zero by convention) given in eq. (2.5) and $\epsilon_{i,j}$ is the subband energy of the i,j^{th} band. Consider a volume in k-space at energy E, which in 1D is simply $2k_z^E$, where $k_i^E = -\sqrt{2m_i(\Delta_o - \epsilon_{i,j} - E)}/\hbar$. Since the energy in the valence band is always less than $\Delta_o - \epsilon_{i,j}$ the expression under the square root is always positive. The total number states, again, is equal to the total volume in k-space divided by the volume factor $(2\pi)/L$ times 2 for the spin degeneracy

$$N(E) = 2k_z^E \frac{L}{(2\pi)} 2 = \frac{2\sqrt{2}L}{\pi\hbar}(m_z)^{1/2}(\Delta_o - \epsilon_{i,j} - E)^{1/2}. \tag{2.19}$$

Taking a derivative we get the density of states per unit length

$$D(E) = \frac{1}{L}\frac{dN}{dE} = \frac{\sqrt{2m_z}}{\pi\hbar}(\Delta_o - \epsilon_{i,j} - E)^{-1/2}. \tag{2.20}$$

This expression for the one-dimensional density of states demonstrates singularities at each subband edge, brought about by the quantum confinement in the nanowire, and results in a very different density of states than that of bulk Bi.

2.3.3 Non-Parabolic L-Point Conduction Band

The problem becomes more difficult when dealing with the non-parabolic bands of Bi. The subband energies are no longer given by the simple expression of eq. (2.17). Since the Lax model, eq. (2.12), can be rewritten as

$$\frac{E_L(\mathbf{k})^2}{E_g} + E_L(\mathbf{k}) = \frac{\hbar^2}{2}\left(\frac{k_x^2}{m_x} + \frac{k_y^2}{m_y} + \frac{k_z^2}{m_z}\right), \tag{2.21}$$

the Schrödinger equation can be written as

$$-\frac{\hbar^2}{2}\left(\frac{1}{m_x}\frac{\partial^2}{\partial x^2} + \frac{1}{m_y}\frac{\partial^2}{\partial y^2} + \frac{1}{m_z}\frac{\partial^2}{\partial z^2}\right)\Psi(\mathbf{r}) = \left(\frac{E_L(\mathbf{k})^2}{E_g} + E_L(\mathbf{k})\right)\Psi(\mathbf{r}) = (\epsilon_{i,j} + E(k_z))\Psi(\mathbf{r}). \tag{2.22}$$

Therefore, the true energy of the non-parabolic subbands is given by equating $\epsilon_{i,j}$ from eq. (2.17) with right side of the Schrödinger equation for $k_z = 0$

$$\frac{E^L_{i,j}(k_z = 0)^2}{E_g} + E^L_{i,j}(k_z = 0) = \epsilon_{i,j}. \tag{2.23}$$

We can then solve for the true subband energies of the non-parabolic L-point conduction band

$$E^L_{i,j}(k_z = 0) = -\frac{E_g}{2} + \frac{E_g}{2}\sqrt{1 + \frac{4\epsilon_{i,j}}{E_g}}, \tag{2.24}$$

where $\epsilon_{i,j}$ is given in equation (2.17). Since $\epsilon_{i,j}$ is non-zero and positive for the conduction band, the quantized subbands will lie higher in energy than the bulk band edge, which is defined as the zero in energy.

Now that we have the subband energies for the L-point conduction band, we will attain their density of states by assuming that each subband is parabolic. This is justified because the L-point bands in Bi are nearly parabolic close to the band edge, and for the 1D density of states, the largest contribution is near the band edge. However, because of the strong non-parabolicity of the band, the transport effective mass is energy dependent and becomes larger as you go deeper into the band. So for each subband (i, j) we will use the corrected mass

$$m^z_{i,j} = m^z\sqrt{1 + \frac{4\epsilon_{i,j}}{E_g}}, \tag{2.25}$$

where m^z is the effective mass at band edge of bulk Bi along the transport direction of the nanowire, z. From this equation we can see that the effective mass is significantly increased for subbands with high energies. This is because the coupling between the L-point conduction and valence bands is decreased as their separation in energy increases.

Figure 2-4 shows the density of states of a 40nm diameter Bi nanowire with the (012) crystalline orientation along the nanowire axis, plotted together with the bulk density of states of Bi at T=77K. At each subband edge the density of states has an $E^{-1/2}$ singularity. Also notice that the energy of the conduction subband edges lie

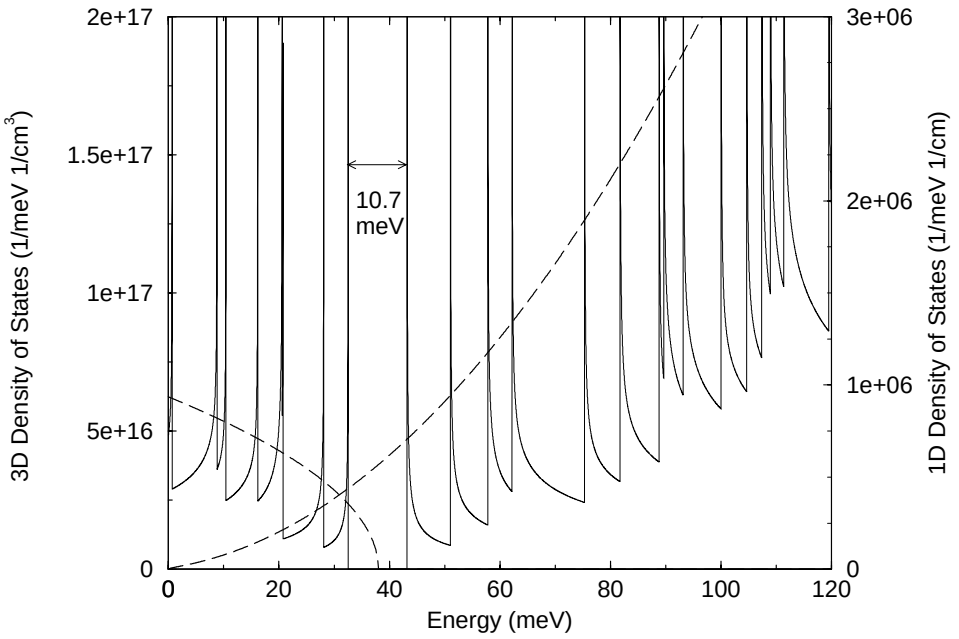

Figure 2-4: One-dimensional density of states of the L-point conduction band and the T-point valence band of a 40nm diameter Bi nanowire with a (012) crystalline orientation along the nanowire axis (solid curves) plotted with the bulk density of states (dashed curves) at 77K.

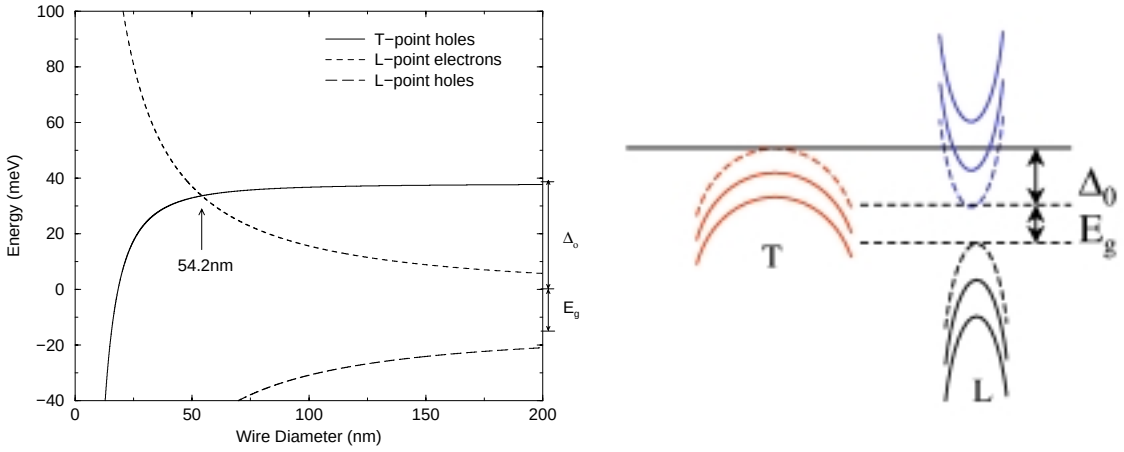

Figure 2-5: Right: Schematic diagram of the quantized band structure of a Bi nanowire. Left: Calculation of the lowest conduction and highest valence subband energies as a function of wire diameter at 77K for a nanowire with the trigonal crystalline orientation along the wire axis.

higher in energy than the bulk conduction bandedge and the valence subband edges lie lower in energy than the bulk valence bandedge. The shifts in energy of the 1D bandedges relative to bulk give rise to the 10.7meV bandgap which will be discussed in the next section.

2.3.4 Semimetal-to-Semiconductor Transition

As the nanowire diameter gets smaller, the energy separations of the subbands increase. For a small enough wire diameter the lowest conduction subband will no longer overlap with the highest valence subband in energy, and the material becomes a semiconductor with a bandgap. This is known as the semimetal-to-semiconductor transition. The diameter at which this takes place is called the critical diameter, d_c. Figure 2-5 shows the highest valence subband energy and lowest conduction subband energy plotted as a function of nanowire diameter for a Bi nanowire with the trigonal crystalline orientation along the nanowire axis calculated at 77K. The critical diameter of 54.2nm is indicated in the figure.

Table 2.2: Calculated critical diameters in nm for the semimetal-to-semiconductor transition for square nanowires compared to those of ref. [1, 2] for circular nanowires.

Calculation Assumption	Trigonal	Binary	Bisectrix	(101)	(012)
circular cross-section	55.1	39.8	48.5	48.7	49.0
square, $d = w$	54.2	39.2	46.1	47.1	48.7
square, $\pi(d/2)^2 = w^2$	61.2	44.2	52.0	53.1	55.0

2.3.5 Comparison of Square and Circular Cross-Section Models

The critical diameters, d_c, for the semimetal-to-semiconductor transition for nanowires of various crystalline orientations are listed in table 2.2 calculated assuming a square nanowire cross-section, in comparison to those of ref. [1, 2] which were calculated numerically assuming a circular nanowire cross-section. Two assumptions are made in the square cross-section model. In the first assumption, the square width w is equated to the diameter of the nanowire d ($w = d$). In the second assumption the area of the square is equated to the area of the circle ($\pi(d/2)^2 = w^2$). As can be seen from table 2.2 the first assumption ($w = d$) yields better agreement with the circular wire cross-section results. This may seem counter-intuitive that the unequal area assumption would yield better agreement than the equal area results. However, because the wavefunction goes to zero at the edges of the square it is almost negligible in the corners of the square, and therefore resembles the wavefunction of the circular assumption very closely.

The left images in figure 2-6 show the two square wire assumptions depicted graphically. From the figure we expect the assumption of equating the square width to the diameter ($w = d$) to be underconfined relative to the circular nanowire cross-section, resulting in an overestimate of the critical diameter. Conversely, we expect the equal areas assumption ($\pi(d/2)^2 = w^2$) to overconfine the carriers, resulting in an underestimate of the critical diameter. This is indeed what we find from our calculations, shown in table 2.2.

The anisotropy of the effective masses in the nanowire is also an important factor

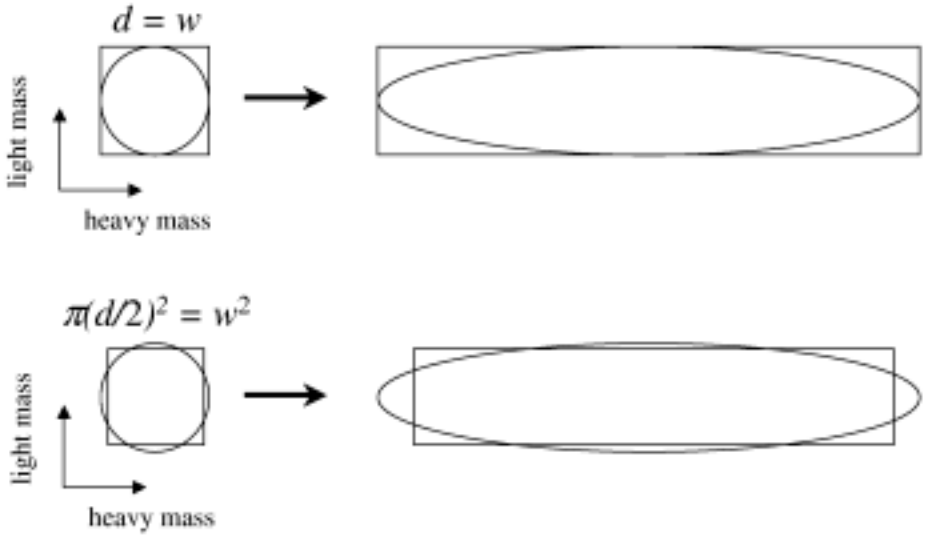

Figure 2-6: Square nanowire cross-section assumptions for anisotropic effective masses(left) and effective masses normalized by scaling the length (right).

in the agreement between the square and circular models. The dimension with the smaller mass will dominate the ground state energy. Therefore, a small change in the confinement length in the small mass dimension will have a large change in the confinement energy. The problem can also be visualized by normalizing the effective masses and scaling the lengths by the appropriate anisotropy. This is shown schematically in the right images of figure 2-6. Since the energy is proportional to the curvature (the second derivative) of the confined wavefunction, the critical dimension in determining the energy is the small mass dimension. In the $d = w$ square wire assumption we expect the result to be in best agreement with the circular wire for highly anisotropic masses. Looking at the results in table 2.2 we find that this is indeed the case. The square wire cross-section model is extremely accurate, especially for nanowire orientations with highly anisotropic m_x and m_y components. For the trigonal, binary and (012) orientations, where the $m_x : m_y$ anisotropies are, 98, 116, and 8, respectively, the results are within 1nm of the circular cross-section model. However, for the bisectrix and (101) orientations, where the $m_x : m_y$ anisotropies are, 2 and 4, the results are within 3nm of the circular model result.

Chapter 3

Fabrication of Bi Nanowires and Lithographic Contacts

In this chapter we discuss how the nanowires are made and how electrical contacts are attached to individual Bi nanowires using lithographic techniques.

3.1 Fabrication of Bismuth Nanowires

In this work, bismuth nanowires are prepared by filling the cylindrical pores of an anodic alumina template with Bi. The fabrication process of the nanowires is shown in figure 3-1. First an alumina template is grown electrochemically on a polished aluminum substrate. The final template thickness is typically about 50μm. The alumina templates contain a nearly hexagonal array of tiny cylindrical channels whose diameters can be controlled by varying the parameters in the electrochemical growth process. Templates with pore diameters between 7 and 200nm have been prepared. Details of this fabrication process and of the alumina template electrochemistry are given elsewhere [2, 11, 12]. Once the template is fabricated, the pores of the template can then be filled with Bi by one of three ways; high pressure injection of molten Bi [2, 11, 12], vapor injection of Bi [13], or electrochemical deposition of Bi [14]. Figure 3-2 shows an SEM (scanning electron microscope) image of an alumina template before and after filling with Bi. The regularity of the array and uniformity of the

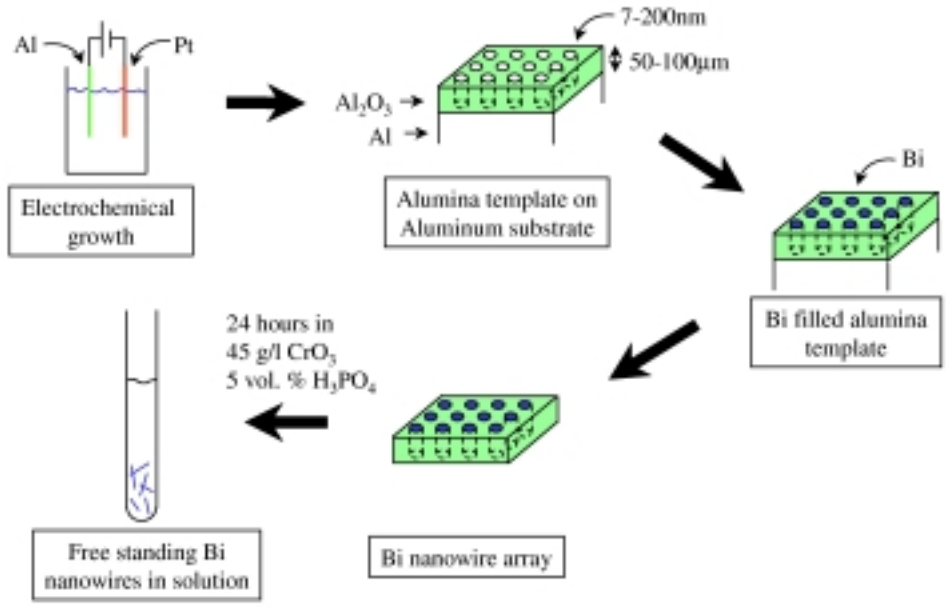

Figure 3-1: Schematic diagram of the fabrication process of Bi nanowires in arrays and as free standing wires.

pore diameters of the templates can be seen from the figure. Once the template is filled with Bi, and allowed to crystallize, the aluminum substrate can be removed by dissolving it in 0.2 M $HgCl_2$. At this point, we have a 50μm thick membrane which contains a well ordered array of Bi nanowires ($\approx 10^{10}$ wires/cm^2 for 50nm-diameter wires). We can also dissolve away the alumina template in a solution of 45g/l CrO_3 and 5 vol. % H_3PO_4 to get a solution of free-standing Bi nanowires.

2-point resistance measurements have been performed on Bi nanowire array samples as a function of temperature and magnetic field for a variety of wire diameters. However, because the number of nanowires making good contacts to the electrodes and therefore contributing to transport is unknown, only the normalized resistance ($R(T)/R(300\text{K})$ and $R(B)/R(B = 0\text{T})$) can be measured, and not the absolute resistivity. The absolute resistivity can only be measured by removing the nanowires from the template and performing a 4-point measurement of the resistance. 2-point measurements on Bi nanowire arrays have demonstrated the semimetal-to-semiconductor

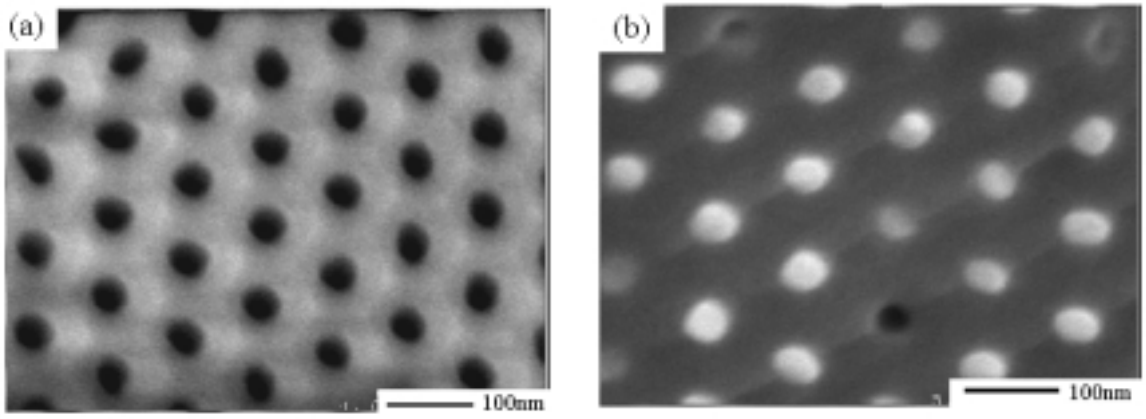

Figure 3-2: (a.) Unfilled alumina template with pore diameter of 40nm. (b.) Bi filled alumina template with pore diameter of 40nm. The dark circles indicate pores that are not filled at the surface.

transition [13], discussed in the previous chapter. However, to monitor the effects of doping and impurities, 4-point measurements are essential. In bulk and 2D conductors, Hall effect measurements are the standard method for determining the carrier density and carrier scattering relaxation times. In a 1D conductor, however, Hall effect measurements are not possible, and 4-point measurements are the most direct way of determining these extremely important quantities.

For a majority of the samples in this work the alumina templates were filled by the high pressure injection of molten Bi. A schematic diagram of the experimental setup is shown in figure 3-3. The empty template on the aluminum substrate is placed in a beaker with some chunks of bulk Bi. The beaker is put into a reaction chamber, which is first evacuated, then heated above the melting point of Bi. Once the Bi is molten, the pressure is increased to 4500PSI (pounds per square inch). The high pressure gas forces the molten Bi into the small pores of the alumina template. The system is then allowed to cool and the Bi crystallizes. Details of this high pressure filling method are given in [2].

The template for the sample shown in figure 3-2 has been filled by the pressure injection of molten Bi. The bright spots indicate pores that are filled with Bi and the

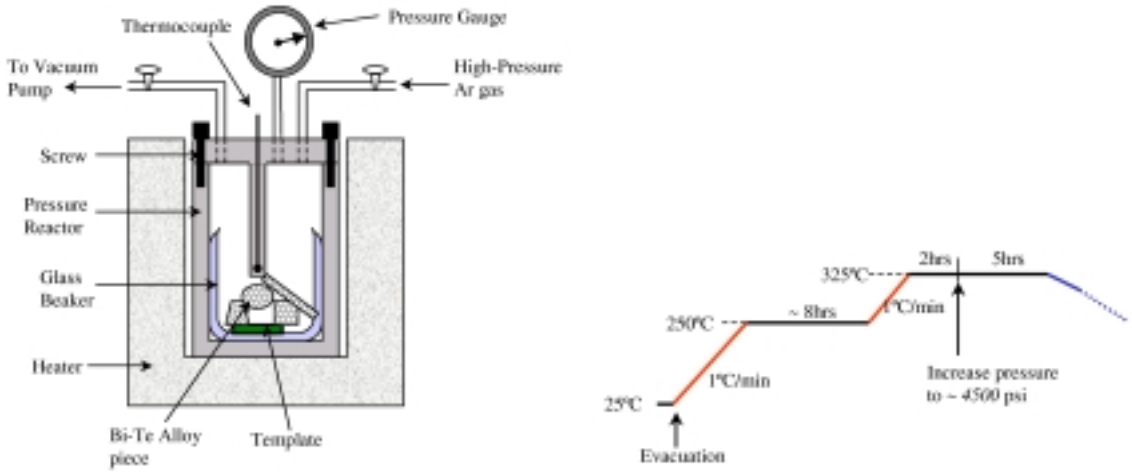

Figure 3-3: Left: Experimental setup for the high pressure injection of liquid Bi into the pores of an alumina template. Right: Temperature profile of pressure injection scheme.

dark spots indicate unfilled pores. From the figure we can see that the filling factor is around 80%. For templates with pore diameters much smaller than 40nm, however, the filling factor becomes much lower. This is because the pressure required to fill the pores depends inversely on the diameter of the pores, as specified by the Laplace relation,

$$P \geq -\frac{4\gamma cos\theta}{d_w}. \tag{3.1}$$

Here P is the pressure required to fill a pore of diameter d_w, and γ and θ are the surface tension and wetting angle, respectively. For a template with a pore diameter of 10nm, the filling factor can be significantly lower than 50%, making other methods of filling more attractive. In fact most filling methods become more difficult as the pore diameter decreases.

3.1.1 Structural Characterization of Bi Nanowires

X-ray diffraction (XRD) spectra show that the Bi nanowires formed in these templates, either by vapor or liquid phase injection, are highly crystalline with a common

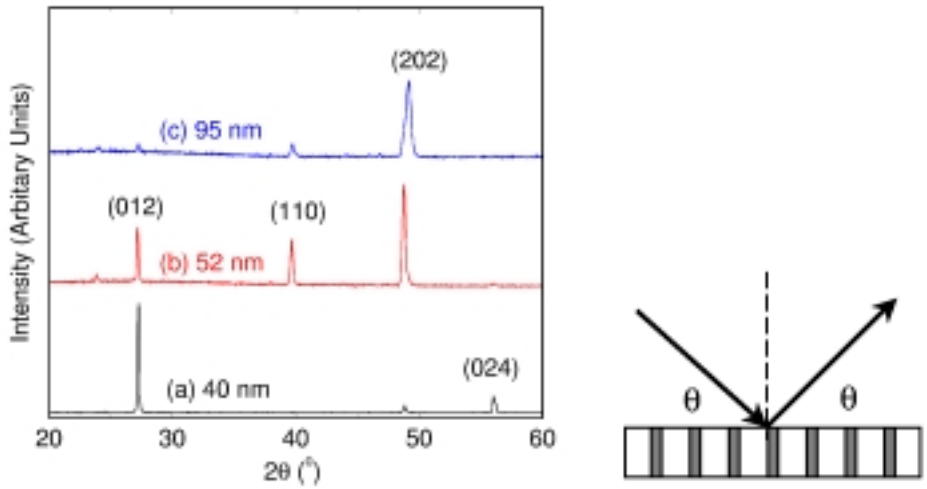

Figure 3-4: X-ray diffraction patterns of Bi nanowire arrays for various diameters.

crystalline orientation along the axis of the nanowire. Diffraction patterns also indicate that the lattice constants in the Bi nanowires are the same as those of bulk Bi. Figure 3-4 shows X-ray diffraction spectra for Bi nanowire arrays. For Bi nanowires less than 40nm in diameter, the preferred growth orientation is with the (012) crystalline direction along the axis of the nanowire, and for Bi nanowires larger than 60nm in diameter the preferred orientation is (101).

We can relate the crystalline orientations observed from XRD to the principal axes of the Brillouin zone. In a hexagonal coordinate system, the binary, bisectrix and trigonal axes are given by $[1\bar{2}10]$, $[10\bar{1}0]$ and [0001], respectively. The observed crystalline orientations (012) and (101) can also be expressed in the hexagonal coordinates as $[10\bar{1}1]$ and $[01\bar{1}2]$, respectively. Taking the direction perpendicular to these planes in real space, we find that the observed orientations (012) and (101) lie in the bisectrix-trigonal plane at an angle of 56.5° and 71.87° from the trigonal axis, respectively. The effective mass components were calculated for these observed crystalline orientations in the previous chapter (section 2.1).

Figure 3-5 shows the high resolution transmission electron microscope (HRTEM) image of an individual 40nm Bi nanowire that was removed from its template (see sec-

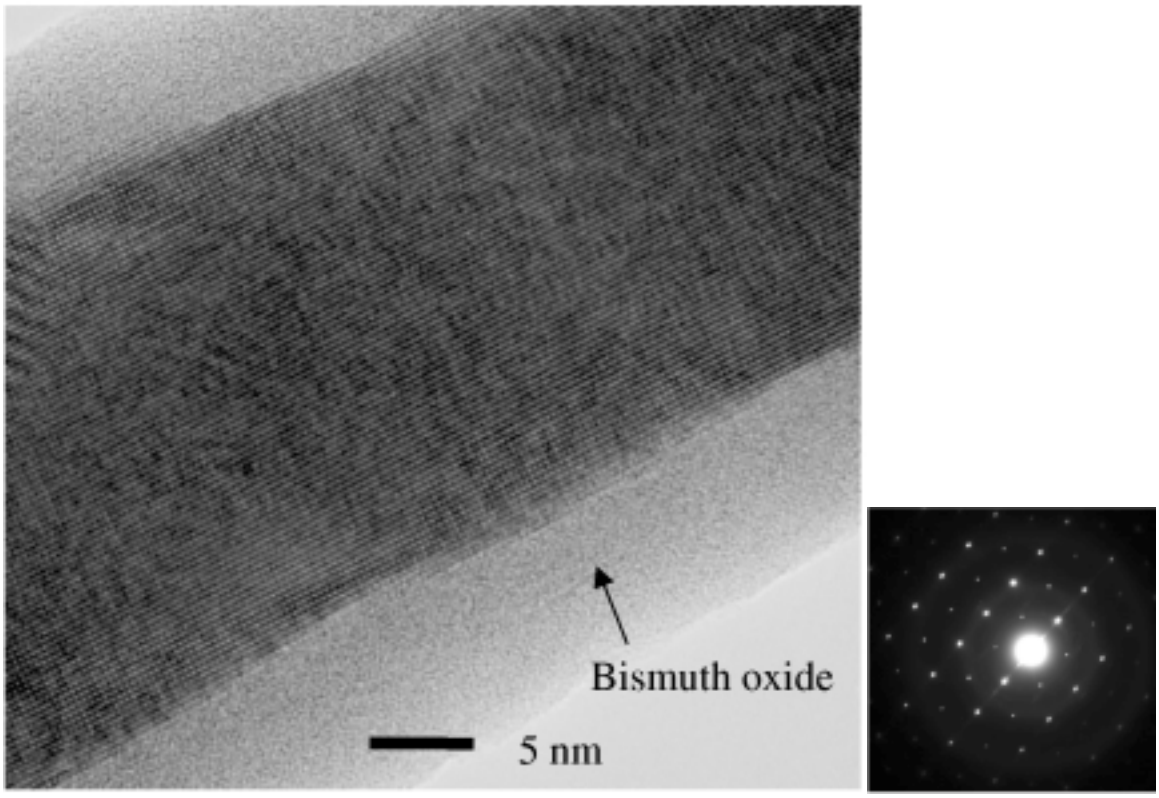

Figure 3-5: Left: High resolution transmission electron microscope (HRTEM) image of a 40nm diameter Bi nanowire. Right: Selected area electron diffraction of a single Bi nanowire. Microscopy was done in the MIT CMSE (Center for Materials Science and Engineering) microscopy facility by Michael Frongillo.

tion 3.2). From this micrograph, we can see the atomic lattice fringes, which demonstrate that the nanowire is single crystal throughout the diameter of the nanowire. Selected area electron diffraction and dark field TEM imaging of free-standing individual nanowires show that these wires have grains with sizes similar to the diameter of the nanowires, and the X-ray diffraction results imply that the crystallites have a common orientation along the wire direction.

3.2 Removing the Bi Nanowires from the Alumina Template

Removing the Bi nanowires from the alumina template turns out to be quite a formidable task. Because of the strong chemical resilience of the alumina and the chemical sensitivity of the Bi, it is very difficult to find a chemical that will selectively etch the alumina and not the Bi. We use a solution of 5% H_3PO_4 and 45g/l CrO_3. The acidic pH of the H_3PO_4 reduces the alumina and the CrO_3 acts as a strong oxidizer. Without the CrO_3 the Bi nanowires are dissolved by the acid. With the CrO_3, however, the nanowires, once out of the template, are oxidized before the acid can dissolve them.

It should be noted that in early experiments we did not realize the roles of these two chemicals with respect to the generation of single Bi nanowires. We inherited this recipe for dissolving the alumina template from the anodic alumina literature, and it was very successful in removing the nanowires from the alumina templates. It was not until after we observed the thick oxide layer shown in figure 3-5, and started experimenting with alternative chemistries that we realized the crucial role of the CrO_3's oxidizing power in generating solutions of single isolated Bi nanowires. More will be said about this subject in section 5.3.6.

To generate a solution of nanowires[1] from a Bi-filled alumina template we put a small piece of template in the H_3PO_4/CrO_3 mixture. A very small piece will yield

[1]The nanowires are not dissolved in the solution, but are free to float around individually.

many nanowires. Pieces of template that are essentially useless dust can be used for this purpose. Once the template has been dissolved, after 24 hours or more, the nanowires clump together in a small black chunk, which sits on the bottom of the vial. We then want to replace the acidic solution with a mild organic (isopropyl alcohol) which will allow the nanowires to be deposited on a substrate with a minimum of residue. Since the isopropyl alcohol reacts with the CrO_3 we must first replace the solution with distilled water twice. In this rinsing process the H_3PO_4/CrO_3 solution must be removed from the vial with a pipette. Care must be taken not to disturb the black chunk which can dissociate prematurely. Once the nanowires dissociate it is not possible to rinse the solution of its acidic constituents. We then fill the vial with distilled water. This rinsing process is repeated with distilled water twice, and then with isopropyl alcohol twice, leaving the second solution of isopropyl alcohol to host the nanowires. To reduce the amount of oxidation taking place in the solution, argon is bubbled through the distilled water and isopropyl alcohol prior to the rinsing process to reduce the amount of oxygen in solution.

Now the vial contains isopropyl alcohol with a black chunk of Bi nanowires. An SEM (scanning electron microscope) image of this chunk is shown in figure 3-6. We can clearly see a bundle of nanowires that are no longer bound to the alumina template. Sonicating the vial for about 5 seconds will cause the black chunk to dissociate into a gray cloud. Excessive sonication will cause the nanowires to break into shorter and shorter pieces. Lengths after the initial sonication can be as long as 20-30μm.

The solution of nanowires is typically good as a source of individual nanowires for a few days. Over time, the nanowires will agglomerate, presumably by Van der Waals bonding, and it will not be possible to separate them by sonication. In addition, the nanowires appear to accumulate a thick coating of organic residue which will subsequently make it difficult to make good electrical contacts to the nanowires.

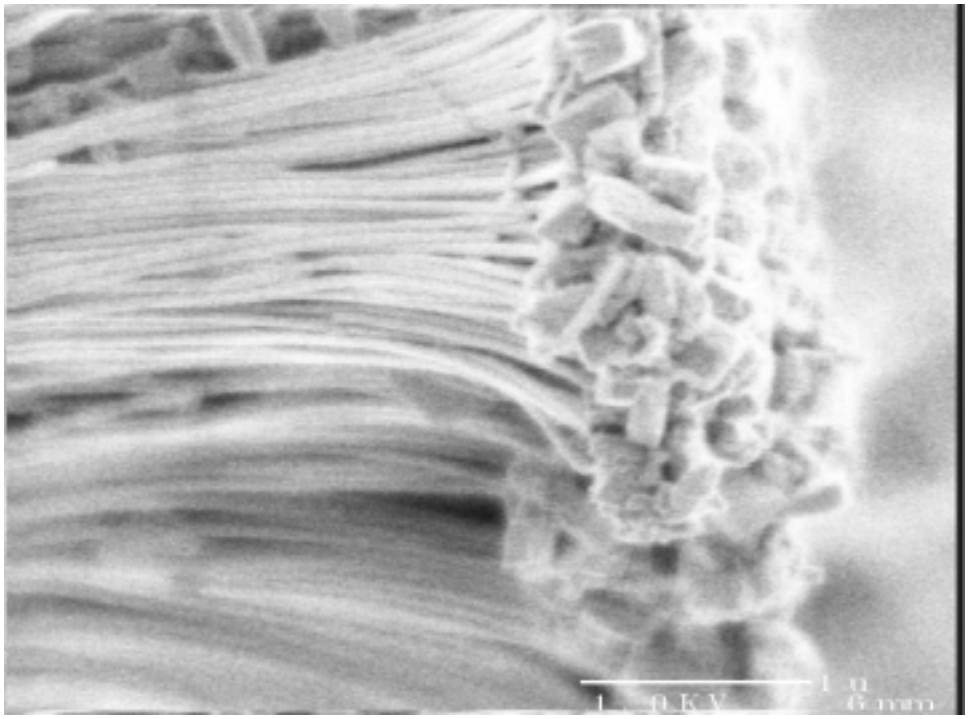

Figure 3-6: SEM image of a bundle of Bi nanowires after the alumina template has been dissolved in the H_3PO_4/CrO_3 solution for 4 days. The Bi chunks on the right of this image are the remnants of a thin Bi film left over from the Bi melt used to inject Bi into the pores.

3.3 Making Metal Contacts to Bi Nanowires using Lithographic Techniques

This section describes the lithographic processes by which metal electrodes are attached to a single Bi nanowire on a substrate. The methods developed here are explained for Bi nanowires. However, the methods are more general and can be applied to almost any nanowire system.

The first subsection describes electron-beam lithography, which is an expensive technique, but can be used to make sub-micron electrodes and with very high alignment accuracy. The second subsection describes an approach using photolithography, which is much cheaper than electron-beam lithography, but can only be used on nanowires that can be seen with an optical microscope (at least 10μm long). The third subsection describes an ultra-violet lithography process which can be used for larger nanowires (at least 10μm long) that are sensitive to strongly basic photodevelopers.

3.3.1 Electron-Beam Lithography

In this work, electrodes were patterned on top of the nanowires using electron-beam lithography techniques. Figure 3-7 shows an SEM image of a 4-point electrode pattern on a 70nm Bi nanowire. The electrodes consist of 1000$\mathring{A}$ thick gold with a 50$\mathring{A}$ adhesion layer of chromium. The processing of these electrodes follows a standard lift-off method. Figure 3-8 shows how a lift-off process is used to pattern a thin layer of metal using a PMMA lithographic mask. After the metal is evaporated everywhere on the sample, the PMMA mask can be dissolved in a strong solvent, removing the metal from all the unwanted areas. Because the metal layer on top of the PMMA is not touching the layer on the substrate, the top layer with the PMMA can be removed without disturbing the substrate layer.

The electron-beam lithography system used in this work was an IBM VS2A in Prof. H.I. Smith's Nanostructures Laboratory at MIT. Before exposing the PMMA

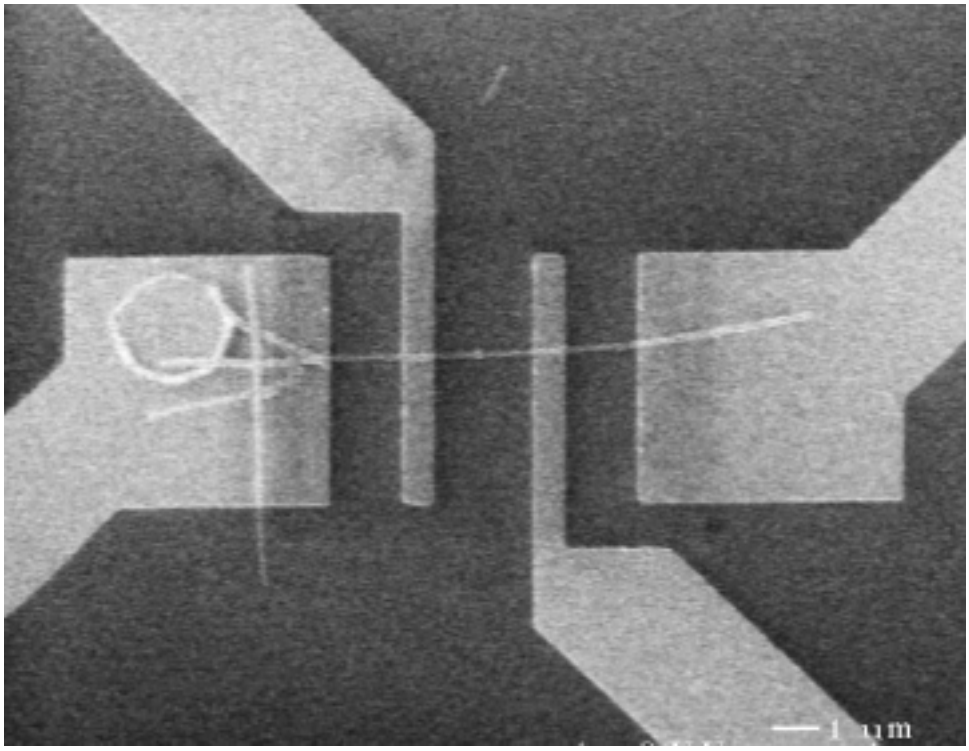

Figure 3-7: SEM image of a 70 nm diameter Bi nanowire with four gold electrode contacts. Under the leftmost electrode are smaller segments of Bi nanowires and a 2μm circular dot that is part of a grid used to locate specific nanowires.

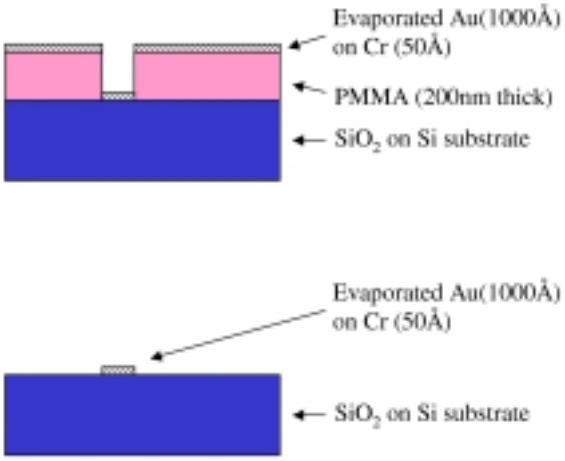

Figure 3-8: Schematic diagram of the lift-off procedure used to pattern thin layers of metal on a substrate using a lithographic mask.

to electron radiation, we first align our coordinate system to the grid of points on the substrate using the *in situ* SEM of the VS2A system.

Figure 3-9 shows the step-by-step process for patterning electrodes on a nanowire. (a.) The first step in preparing the electrodes is to fabricate a grid of points on a Si substrate using standard photolithography techniques. We used a grid of circular dots 2μm in diameter with a spacing of 40μm. One of these dots can be seen in figure 3-7 underneath the leftmost electrode. (b.) We then deposit Bi nanowires by applying a drop of solution containing free standing nanowires and allowing the solution to dry. (c.) We then locate a single isolated nanowire relative to the photolithographically defined grid of points using an optical microscope or otherwise[2]. (d.) A layer of PMMA (poly-methyl methacrylate) is then spin coated on top of the wires. The PMMA is chemically sensitive to electron radiation, and will serve to define the electrode pattern. (e.) Before exposing the electrode pattern with e-beam radiation, we first align our coordinate system to the grid of points on the substrate. Care must be taken not to expose the resist in the area near the wire, as the SEM electron beam will also expose the PMMA resist. This is avoided by first finding reference markers in the photolithographically-defined grid of points near the edge of the substrate, away from the selected nanowire. (f.) We then turn off the electron beam and move the sample stage by the relative distance between the reference point and the desired nanowire, which was previously recorded in the optical microscopy step, so that the electron beam will be centered on top of the wire. (g.) A computer file containing the desired electrode pattern is loaded into the VS2A. This file controls the deflection of the electron beam, and traces out the desired electrode pattern, writing the pattern into the PMMA. By setting the speed of the trace and the beam current, the desired electron radiation dosage can be selected. For the smallest features of this pattern, 250nm, an electron beam of 100pA at 50kV was used, with a beam size of 80-90nm in diameter, scanned at a frequency of 660,000 pixels/second at a field size of $120\mu\text{m}^2$.

[2]Despite the fact that the diameters of the Bi nanowires are much less than the wavelength of light, they can be seen with an optical microscope because of their large lengths (20μm). For nanowire systems that cannot be seen optically, scanning electron microscopy (SEM) or atomic force microscopy (AFM) can be used to locate the nanowire with respect to the underlying grid.

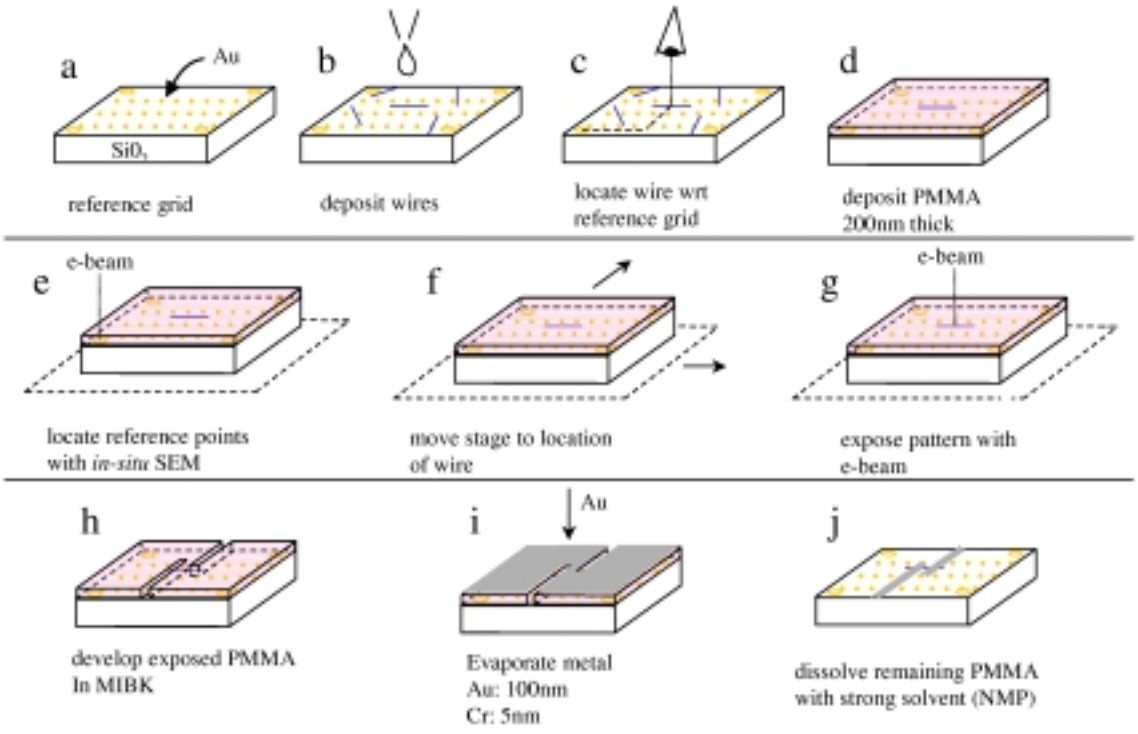

Figure 3-9: Fabrication of 4-point electrode pattern illustrated here for two point contacts (see text). (wrt = with respect to)

(h.) After the electron beam exposure is completed, the PMMA is then developed, using a solution of 2:1 iso-propanol:MIBK (methyl-iso-butyl-ketone), which dissolves the exposed PMMA, while leaving the unexposed PMMA in place. This yields very steep side-walls that are good for the lift-off process. (i.) Then we evaporate the metal for the contacts (in this case we used 100nm gold, with a 5nm adhesion layer of chromium) using an electron-beam evaporator. (j.) Finally, the remaining unexposed PMMA is removed using NMP (1-methyl-2-pyrrolidinone) at 90°C. At this point all that is left on the substrate is the evaporated metal, only in those regions where the electron beam had been exposed, and the desired Bi nanowire underneath these electrodes.

Electron beam lithography is ideal for patterning electrodes to nanowires. The fine resolution of the electron beam is capable of writing electrodes that are much smaller than other forms of lithography. Also, the precision with which lithographic

patterns can be aligned to the nanowires is much higher than that of other forms of lithography.

Chemically, the e-beam lithography process is much more inert to the nanowire surface. All of the chemicals in the e-beam processing are neutral solvents. This has some advantages over the strongly basic developers of photolithography, as will be discussed in section 3.3.3. The only disadvantage of e-beam lithography is that it is significantly more expensive than other forms of lithography, and requires a skilled technician to run the apparatus.

3.3.2 Photolithography

Perhaps the most tedious part of the process of making contacts to the nanowires lies in locating a single isolated nanowire and recording its location with respect to the reference grid. Hundreds of μm^2 must be surveyed in this process to find a nanowire that is long, straight, isolated and away from any debris. Since the nanowires are long enough to be seen optically, a lot of time (and money) is saved by doing this part of the experiment using an optical microscope. The precision of the alignment that can achieved optically is approximately 2μm, which is acceptable for nanowires $> 10\mu$m in length.

Since the 4-point electrode pattern need only be aligned to the nanowire with $\pm 2\mu$m precision, photolithography can also be used to pattern electrodes. This is, however, pushing the limits of this type of lithography in more ways than one. Since the smallest feature size that can be written is 2μm, the size of the electrode pattern must be expanded, requiring longer nanowires. Also, the large particles of debris generated during the sonication process make it difficult to obtain close contact between the photomask and the sample.

Figure 3-10 shows electrodes patterned on top of a 40nm diameter Bi nanowire using photolithography. Notice that the edges of the pattern are rough, especially around the corners of the pattern. Ignore for the moment, the indentations in the four contact regions. This will be discussed in section 5.3.3. In this work, the photoresist AZ5214E (manufactured by Clariant) was used with an image reversal processing

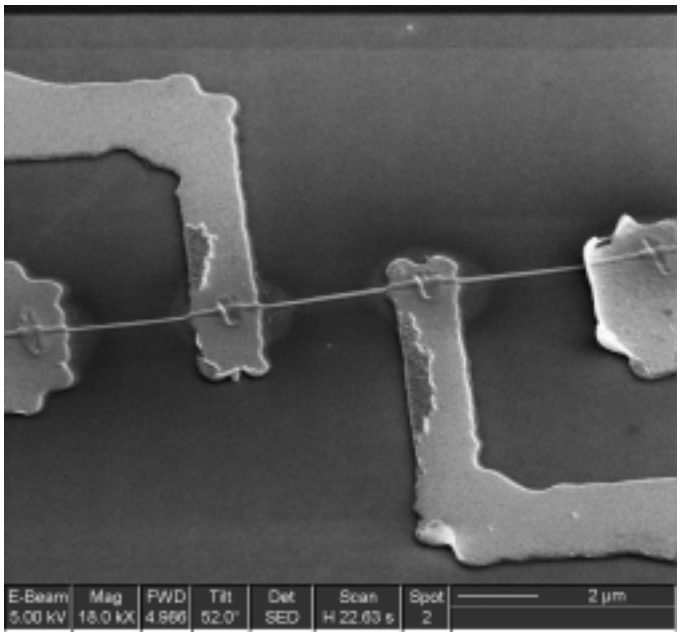

Figure 3-10: SEM image of a 40nm Bi nanowire with four gold electrodes prepared by photolithography.

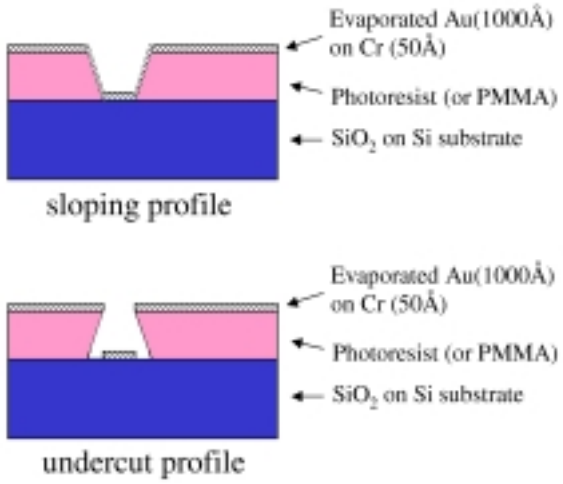

Figure 3-11: Comparison of *undercut* and *sloping* resist profiles used for a 'lift-off' lithographic process.

technique to pattern the inverse of the photomask pattern. This enabled us to use a photomask that is predominantly clear (bright field), thereby allowing us to image the nanowires through the mask to align the electrode pattern on top of the desired nanowire. Another advantage of the image reversal process is that it gives an *undercut* resist profile, which is ideal for the lift-off procedure. Figure 3-11 compares a *sloping* photoresist profile to an *undercut* profile. From this figure it is clear that for good lithographic features it is advantageous to have an *undercut* profile. If the profile of the photoresist is not steep enough, the metal layer will be continuous and there will not be a good lift-off with sharp features.

Typical parameters for the photolithography process were as follows. First AZ5412E photoresist was spin coated on the wafer with nanowires at 4000RPM for 30 seconds, then baked at 90°C for 30 minutes. With the photomask in place, the initial exposure was 2.75 seconds at 6.0mW/cm^2, with a 356nm light source. This is the most critical step. The sample was then baked on a hot plate for 52 seconds, and then flood exposed (without the photomask) for 1 minute at 6.0mW/cm^2. The sample was developed for 1.5 minutes in AZ442 developer (also made by Clariant).

Photolithography lacks the high resolution and precision of electron beam lithography. In fact, the size scale of the Bi nanowires are very close to the limits of standard photolithography techniques. However with photolithography, samples can be prepared in less time, and at a much reduced cost, relative to the e-beam process described in section 3.3.1.

3.3.3 UV Lithography

One very large difference between PMMA and photoresist lies in their developers. PMMA is developed in MIBK (methyl-iso-butyl-ketone), which is a neutral solvent. Photoresist, however, is developed in TMAH (tetramethyl ammonium hydroxide), which has a pH of 12-13. As will be shown in later chapters, very small amounts of Bi are dissolved rapidly in such highly basic solutions. And it is therefore necessary to use PMMA because of the chemical sensitivity of the Bi nanowires. However, the photolithography technique, discussed in the previous section, had proved to be

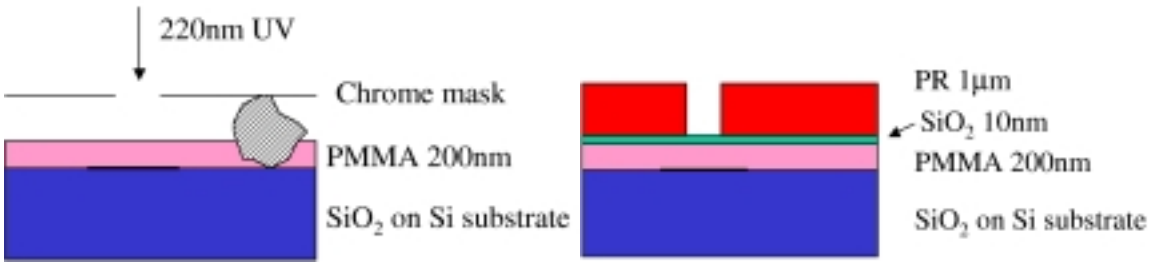

Figure 3-12: Left: Schematic diagram of UV lithography utilizing a chrome on quartz photomask. Right: Schematic diagram of UV lithography using a patterned photoresist (PR) layer as a lithographic mask.

attractive from the standpoints of money, time, and equipment availability, so instead of reverting back to electron-beam lithography, we chose to expose the PMMA with ultraviolet light using a quartz photomask. This work was carried out with Dr. James Goodberlet in Prof. H.I. Smith's Nanostructures Laboratory at MIT.

Two UV techniques will be discussed. The first uses a contact lithographic mask. Since glass is opaque to UV light, we must use a chromium-on-quartz photomask. Using this lithography on a clean substrate with PMMA, it is possible to attain features smaller than 110nm with a radiation source having a wavelength of $\sim$ 220nm [15]. However, because of the aggressive sonication required to prepare the Bi nanowires solution, the solution is fraught with many large debris particles, mostly excess Bi from the bottom side of the template. This problem is common to self-assembly techniques, and results in a solution containing large debris particles that are not up to the clean room standards for contact lithographic techniques. This debris can be as large as a few microns, causing a separation between the mask and the PMMA, which leads to interference patterns that destroy the desired lithographic pattern. This is illustrated schematically in the left image of figure 3-12.

The debris had not been a problem with the previously described lithographic techniques for a number of reasons. The electron-beam lithography exposure does not require contact. It was not a problem with the photolithography technique because the contact is a hard contact, that is, the contact is forced instead of vacuum

driven, as is the case for the UV exposure. Since Bi is very soft, and the debris particle is very small in cross-section, the Bi particles are easily squashed by the macroscopic force applied to the photomask. Also, the photoresist is not as sensitive to interference patterns created by the gap between the mask and the sample, because as it is exposed, its index of refraction changes significantly, causing the fringes to shift. And finally, the 220nm light source is more monochromatic than the 365nm light source, and therefore more prone to these interference effects. To correct this problem, we tried centrifuging out the debris particles, but we were ultimately unsuccessful with this approach. We also tried to eliminate the interference problems by using transparent substrates, but we were unable to reduce the effect of interference.

The second UV lithography scheme we used is illustrated in the right image of figure 3-12. Here we use the photoresist as a lithographic mask for the exposure of the PMMA. To prevent the intermixing of the PMMA with the photoresist, a thin layer of SiO_2 is deposited between the layers. This approach proved to be successful for the following reasons: 1.) The photolithography process has already been established and is robust to the debris particles of the nanowire solution. 2.) Since the photoresist is almost completely opaque to the 220nm ultraviolet radiation, it serves as a good mask for the exposure of the underlying PMMA. 3.) The PMMA will protect the nanowire from the TMAH photodeveloper, as well as the HF acid used to strip off the SiO_2. Because PMMA is the bottom layer, the wire only comes in contact with the MIBK, which is a neutral solvent.

Because of the multilayered structure, the development process is now quite complex. The step-by-step process is described below. 1.) deposit nanowires on the substrate from solution, 2.) spin coat and bake the PMMA layer (200nm), 3.) evaporate SiO_2 (10nm), 4.) spin coat and bake the photoresist layer ($\sim 1\mu$m), 5.) align the photomask and expose the photoresist using parameters from the previous section (section 3.3.2), 6.) develop the photoresist in TMAH developer (AZ422), 7.) expose with 220nm UV radiation at 5mW/cm^2 for 15-20 minutes, 8.) strip the photoresist with acetone. (It is important that the acetone not touch the PMMA, which will cause it to become over-developed in seconds.), 9.) strip off the SiO_2 layer in HF, 10.)

develop the PMMA in MIBK, 11.) evaporate metal for contacts, and 12.) lift-off the remaining PMMA in NMP (1-methyl-2-pyrrolidinone) at 90°C.

One problem with this procedure is that the SiO_2 has a compressive strain, when deposited by electron-beam evaporation, which causes crinkling in the film stack. This crinkling causes pinholes in the layers of the stack, causing problems with the complex development process, and leads to a low sample yield.

3.4 Preventing Burnout of Nanowires

Once the four electrodes are patterned on a Bi nanowire, care must be taken to prevent the nanowire from being burned out by unwanted electrical currents. The small diameter of the nanowires and the low melting point of Bi (271°C) make the Bi nanowires especially prone to burn-out by static discharge. If care is not taken to prevent unwanted currents from passing through the wire, the sample will be damaged, as shown in figure 3-13. To prevent this from happening, the sample must be kept shorted at all times, until right before the measurement is taken. To achieve this, the nanowire is shorted twice.

The four electrodes shown in the SEM image of figure 3-7 are connected to four large bonding pads (300x300μm), shown in figure 3-14, which, in turn, are connected to a current source and voltmeter. The four bonding pads are shorted on the wafer by thin conducting strips that run along the perimeter of the pattern, as can be seen in the figure. After the meters are hooked up, the sample is shorted externally by a circuit of switches and potentiometers. The circuit diagram for the external shorting of the sample is shown in figure 3-15. Now that the sample is shorted twice, it is safe to remove the *on-wafer* shorts. This is done using a small diamond scribe (Techni-Tool's Diamond MicroScribe, part number 244PR100). The scribe is also shorted to the sample before use, to assure that no charge is transferred to the sample. Because of the small distance between bonding pads (100μm), the scribing is done under a stereoscopic microscope with a working distance of several inches. It is important that the scribing of the *on-wafer* shorts is done while the sample is mounted on the

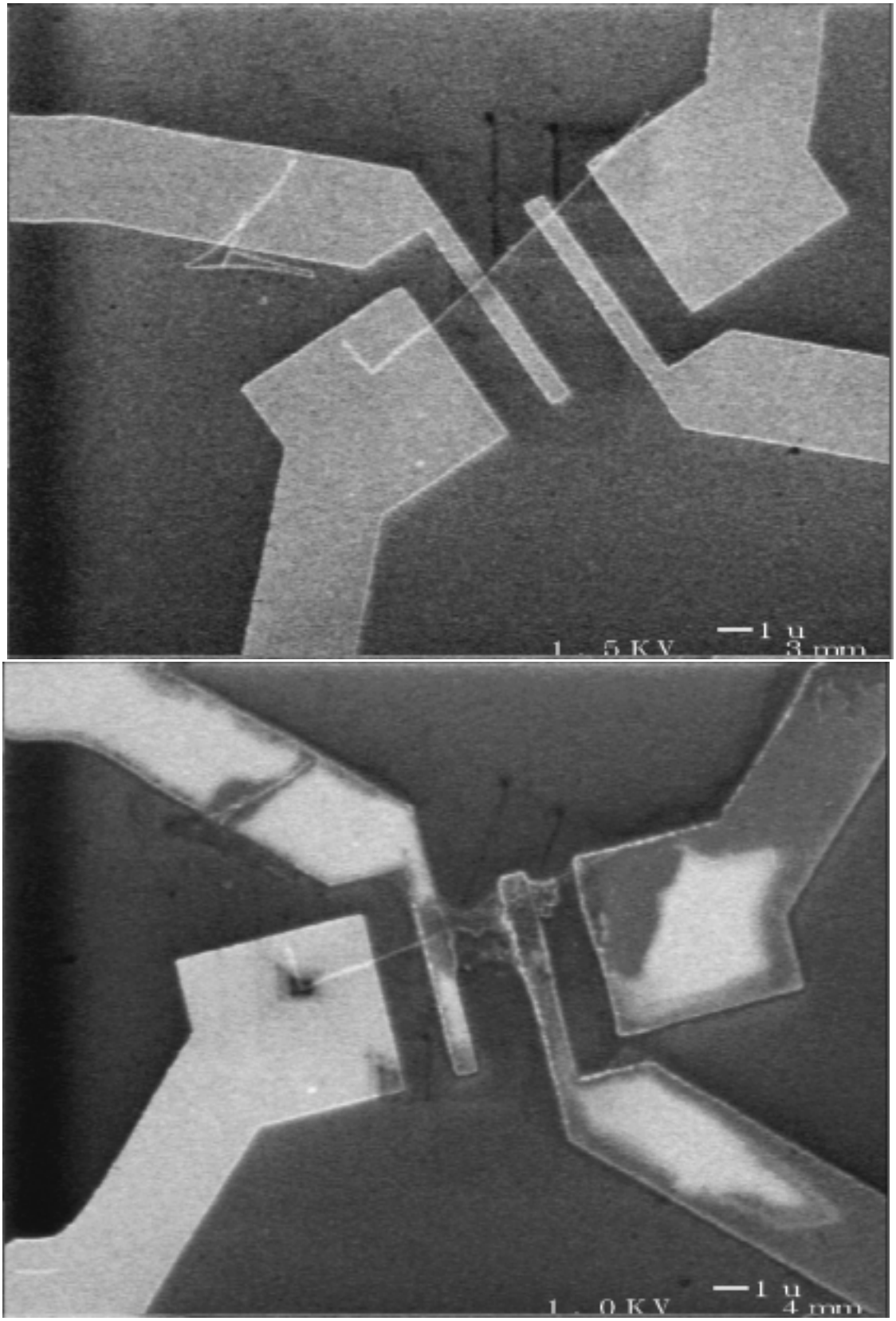

Figure 3-13: SEM image of a 70nm diameter Bi nanowire with four gold electrodes before (top) and after (bottom) the nanowire was burned out by an electrostatic discharge.

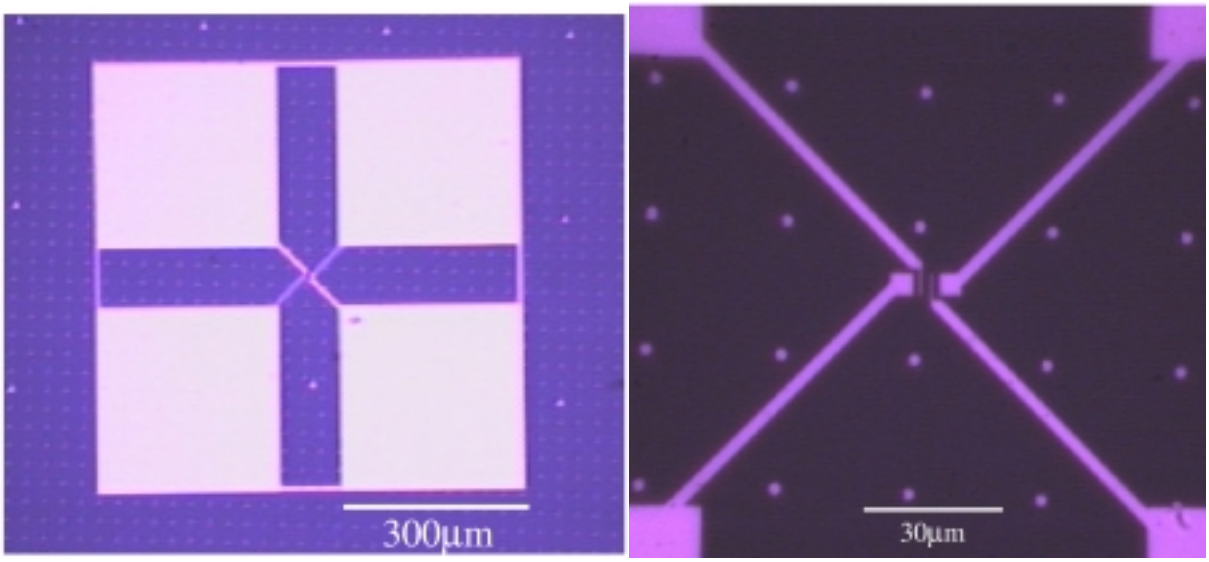

Figure 3-14: Optical image of the 4-point electrode pattern with its four large bonding pads that are shorted along the perimeter. Right image shows a close-up of the electrode region.

probe and connected to the meters. Once the *on-wafer* shorts have been scribed, all measurements must be performed. Removing the sample from the probe will remove the external shorts and cause the sample to be burned out. Hence, once the sample is scribed, it cannot be moved from one probe to another.

We can estimate the amount of current that will cause a nanowire to be burned out by equating the energy of joule heating in the nanowire to the energy required to melt the nanowire. We first calculate the number of moles of Bi in a given nanowire based on its volume and the density of Bi. The energy required to melt the nanowire is equal to the number of moles times the heat capacity (25.5 J/mol K) times the change in temperature required to reach the melting of Bi (271°C) plus the latent heat of fusion (11 kJ/mol). For a 100nm diameter nanowire 20μm in length, this energy is calculated to be 1.29 x 10^{-10} Joules. The energy per second for Joule heating is equal to the current squared times the resistance of the nanowire, i^2R. For a 100nm diameter nanowire 20μm long, the 4-point resistivity was measured to be 7 x $10^{-4}\Omega$-cm (discussed in section 5.3.3), implying a resistive value of 18kΩ. From ex-

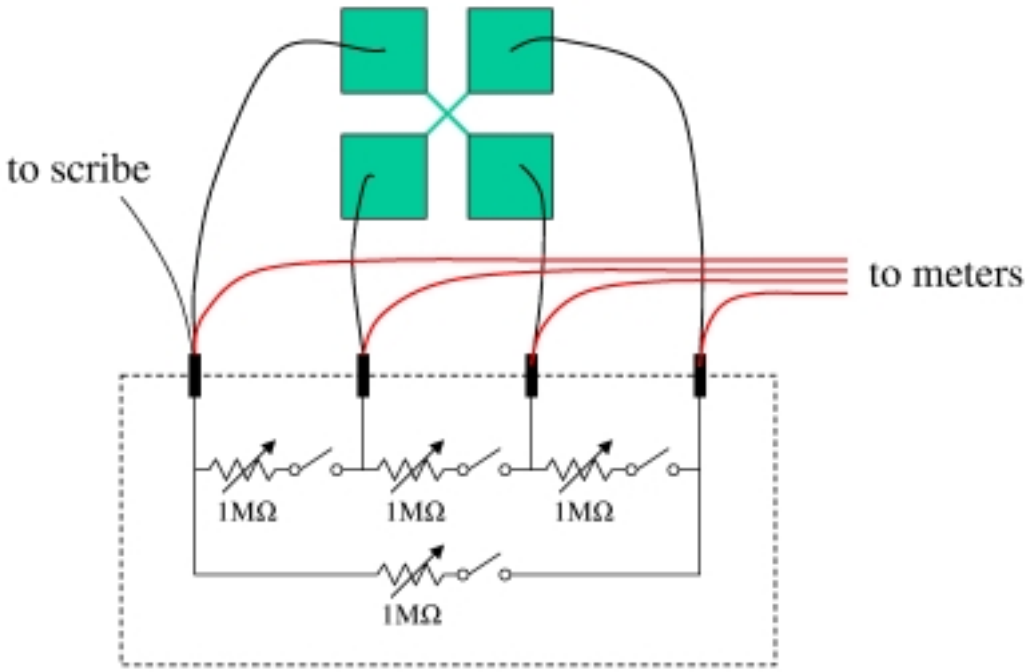

Figure 3-15: Circuit diagram for externally shorting a nanowire sample.

periments where two thermocouples where patterned 10μm apart on a substrate near a small heater (discussed in section 4.3), we observed that temperature gradients were equilibrated with their surroundings in milliseconds. From these values we estimate the amount of current required to melt the nanowire to be 2.7μA. This is consistent with our experiments in which we apply currents up to 1μA without damaging the nanowires.

Chapter 4

2-Point Measurements of Single Bi Nanowires

In this chapter we discuss 2-point resistance measurements of single Bi nanowires with lithographically patterned contacts. The 2-point measurements characterize the quality of the electrical contacts which, as will be shown, are extremely important even for a 4-point measurement. First, experimental results for 2-point measurements are discussed, and then a theoretical model is presented to explain the highly non-ohmic $i(V)$ responses of the contacts to bulk Bi and to Bi nanowires.

4.1 Experimental Results

Now that we have attached metal contacts to the nanowires and have taken precautions to prevent static discharge through the nanowires, we are ready to take electrical measurements. In order to characterize the $i(V)$ behavior of the contacts, $i(V)$ curves are first measured across two electrodes instead of four. The contact resistance was found to be typically on the order of MΩs with a very non-linear $i(V)$ response. A typical $i(V)$ curve for a 70nm nanowire with Cr-Au contacts is shown in figure 4-1. This non-linear $i(V)$ response is believed to be due to the interface of the metal contacts, chromium, with the Bi nanowire, separated by a thin insulating oxide layer. This insulating layer would provide a tunnel barrier for the electrons passing through

the contact to the nanowire.

Generally, a 1MΩ contact resistance is not too high to perform 4-point measurements, even at the very low currents required to prevent burnout of the nanowires ($\sim 1\mu$A). However, the voltage measured across the inner two electrodes was found to be too noisy to get any meaningful data. This proved to be the case even when alternating current measurements were done using a function generator and a lock-in amplifier. This is believed to be due to the non-ohmic behavior of the contacts, which have a very high contact resistance for very low currents (as is the case for a measurement of the voltage across the inner two electrodes).

Improvement of the contacts by annealing is not feasible because of the low melting point of Bi (271°C). We therefore cannot anneal at a high enough temperature for significant diffusion of the electrode material (in this case chromium) through the oxide.

Another strategy for improving the signal from the nanowire is to use the back gating of the doped Si substrate to apply an electric field to the nanowire. This has the effect of altering the Fermi level in the nanowire and thus varying the carrier density. A decrease in the carrier density will result in an increase of the resistance of the nanowire. For high enough applied fields, the resistance of the nanowire can, in principle, be made to exceed the contact resistance, making the nanowire the most resistive element of the circuit. In our experiments, however, no changes in the $i(V)$ characteristics were observed when a gate voltage was applied. This could be due to the semimetallic nature of the nanowires measured, making them less sensitive to changes in the Fermi level, or to the insufficiently doped substrate, incapable of providing large enough electric fields.

The 2-point $i(V)$ responses for Bi nanowires were found to vary widely from sample to sample, and even between different electrodes of the same sample. Figure 4-2 shows two more such $i(V)$ curves. The left curve shows similar behavior to that of figure 4-1, but has a large discontinuity near zero current (high resistance) indicating increased tunneling relative to the sample of figure 4-1. The right $i(V)$ curve of figure 4-2, however, appears to be quite linear. Also, the $i(V)$ curve of figure 4-1 is not symmetric

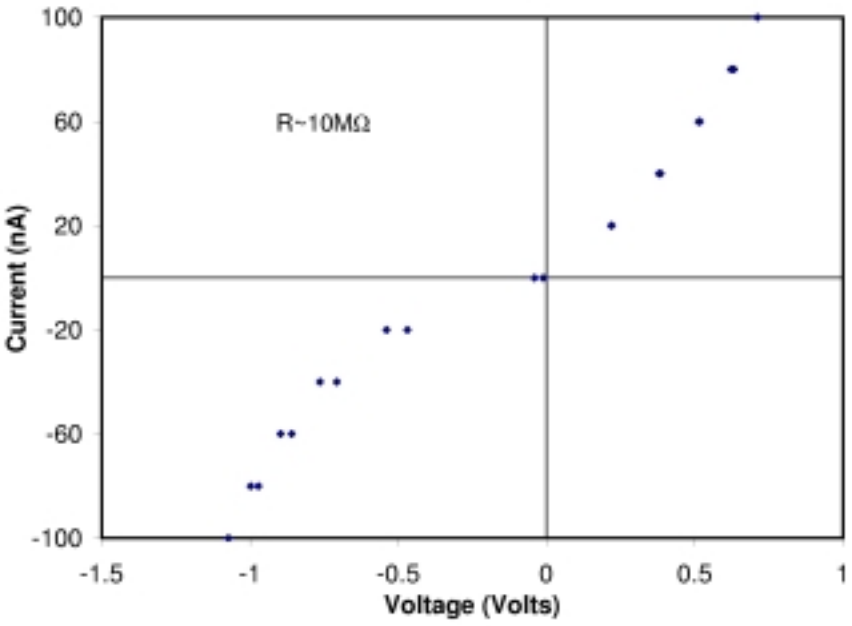

Figure 4-1: Non-linear $i(V)$ response of a 2-point resistance measurement of a 70nm Bi nanowire with Cr-Au contacts.

about V=0, whereas the curves of figure 4-2 are. This asymmetry is believed to be due to dissimilar tunneling contacts of the two electrodes. The non-linearity of the $i(V)$ response of the samples is found to increase dramatically as the temperature is decreased. The temperature dependence of a typical $i(V)$ curve is shown in figure 4-3. The curves become steeper and more linear as the temperature is increased. To understand this $i(V)$ behavior, we do the following calculation, described in section 4.2.

4.2 Theoretical Modeling

4.2.1 Tunneling Contacts to Bulk Bi

In this section we attempt to model the metal-oxide-Bi contact to generate $i(V)$ curves with the same shape as those observed. By doing this modeling we hope to understand the physics at the contact interface. In the following section (section

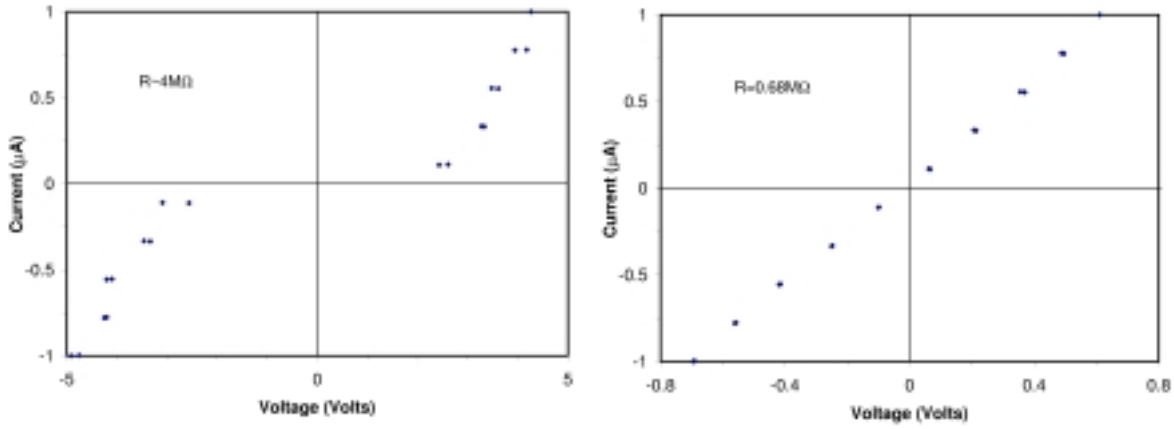

Figure 4-2: 2-point $i(V)$ response for two different 70nm diameter Bi nanowires with Cr-Au contacts.

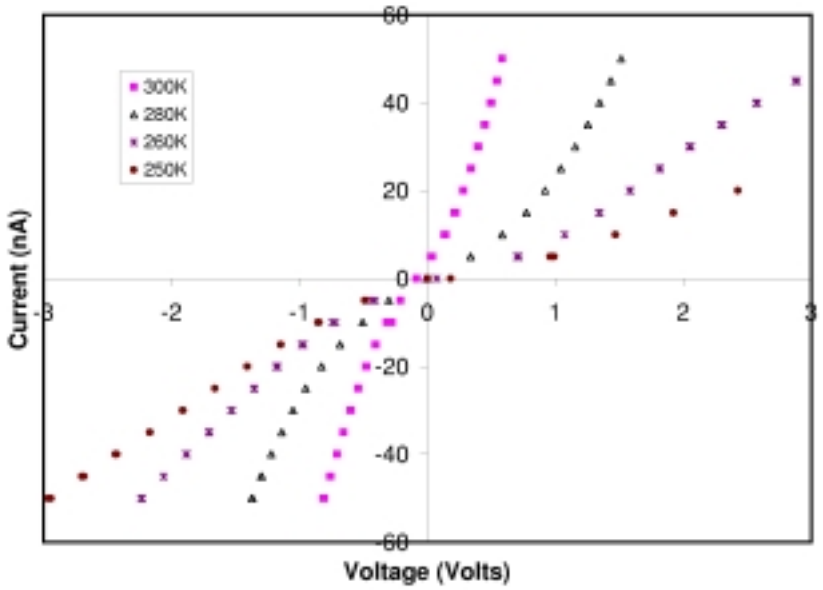

Figure 4-3: Temperature dependence of 2-point $i(V)$ curves of a 70nm Bi nanowire.

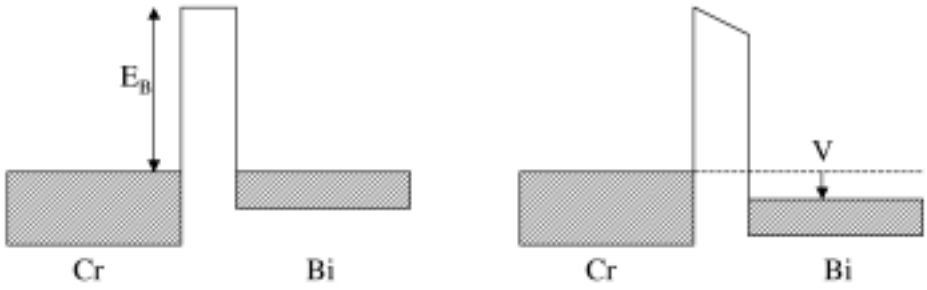

Figure 4-4: Energy band diagram of the metal-oxide-Bi junction with (right) and without (left) an applied forward bias voltage V, and E_B is the barrier height of the oxide.

4.2.2), we will extend this calculation to nanowires with a quantized band structure to gain insight into the possibility of obtaining information about the nanowires using these contacts, for example, by carrying out tunneling spectroscopy measurements of the nanowire subband structure.

In figure 4-4 the energy bands of the contact region are depicted schematically, both with and without an applied voltage V. In a typical measurement, the metal contact is made of chromium separated from the Bi by a few nanometers of oxide. The tunneling current through this junction can be expressed in terms of the occupied density of states of the Cr electrode, $D_{Cr}(E)f(E)$, the unoccupied states of the Bi, $D_{Bi}(E)(1 - f_{Bi}(E))$, and the tunneling probability, $T(E, V)$

$$i_{forward}(V) = \int D_{Cr}(E)f_{Cr}(E) \cdot D_{Bi}(E)(1 - f_{Bi}(E)) \cdot T(E, V)dE. \tag{4.1}$$

Here, $D_{Cr}(E)$ and $D_{Bi}(E)$ are the density of states of the Cr electrode and Bi, respectively, $f_{Cr}(E)$ and $f_{Bi}(E)$ are the Fermi functions for Cr and Bi, respectively, and $T(E, V)$ is the tunneling probability.

At zero applied voltage, the Fermi levels of the two conductors are aligned, as shown in the left image of figure 4-4. When a voltage V is applied in the forward bias direction (see figure 4-4), the Fermi levels of the two conductors become offset from one another, creating an offset between the occupied states of one material with the

unoccupied states of the other, resulting in a tunneling current.

In eq. (4.1) we consider the tunneling of electrons from the Cr electrode to the Bi. However, when calculating the $i(V)$ of a junction, we must also consider the reverse tunneling current, that is, tunneling from the Bi to the Cr, which will dominate when a negative voltage is applied. Since the tunneling is from the Bi to the Cr, the reverse current is proportional to the occupied density of states of the Bi, $D_{Bi}(E)f_{Bi}(E)$, and the unoccupied density of states of the Cr electrode, $D_{Cr}(E)(1 - f_{Cr}(E))$,

$$i_{reverse}(V) = \int D_{Bi}(E)f_{Bi}(E) \cdot D_{Cr}(E)(1 - f_{Cr}(E)) \cdot T(E, V)dE. \qquad (4.2)$$

The resulting $i(V)$ response of the junction can now be expressed as the difference of the forward and reverse currents,

$$i_{junct}(V) = i_{forward}(V) - i_{reverse}(V). \qquad (4.3)$$

Figure 4-5 shows the occupied and unoccupied density of states for Cr and Bi plotted as a function of energy. The Fermi energy for Cr is taken as 1660meV, yielding 10^{22} electrons/cm^3. The relatively small size of the Bi Fermi energy, 25.7 meV relative to the Bi band edge, makes it difficult to see the deviation of the unoccupied states from the total density of states of Bi. As was mentioned in section 2.3.3, the non-parabolic nature of the electrons in Bi gives rise to the strange looking density of states, figure 4-5. When a positive voltage is applied, the Bi band is shifted to the left (relative to the Cr band), causing the product of the density of states, $D_{Bi}(E)f_{Bi}(E) \cdot D_{Cr}(E)(1 - f_{Cr}(E))$, to be increased. Likewise, for a negative applied voltage, the Bi band is shifted to the right, leading to a decrease in the product of the density of states.

To calculate an expression for the tunneling probability, $T(E, V)$, we will assume that the tunneling barrier potential in an applied electric field is rectangular, rather than triangular, and that the height of this potential be $E_B - V/2$, rather than E_B. This simplification is depicted schematically in figure 4-6. Using the semi-classical

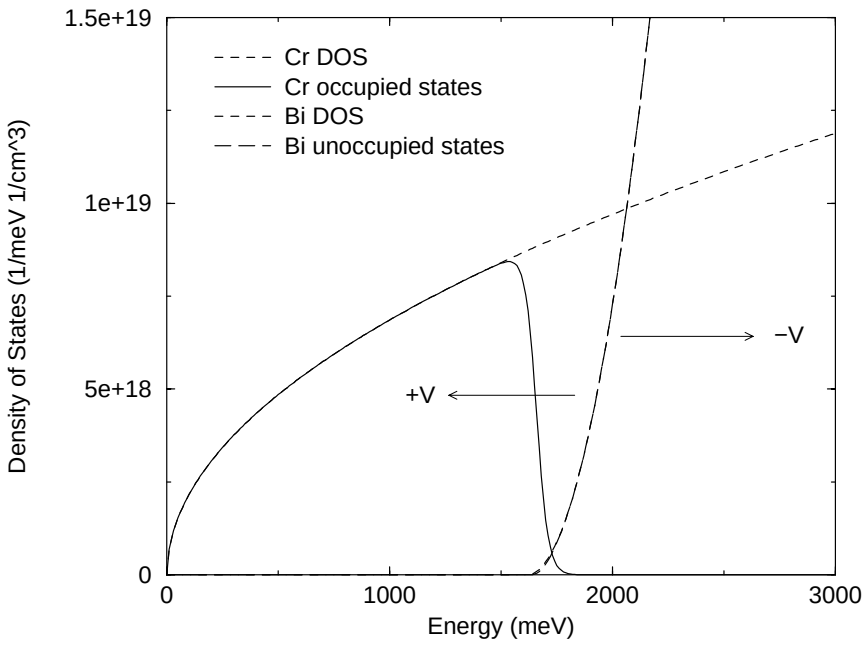

Figure 4-5: Occupied and unoccupied density of states for bulk Cr and Bi.

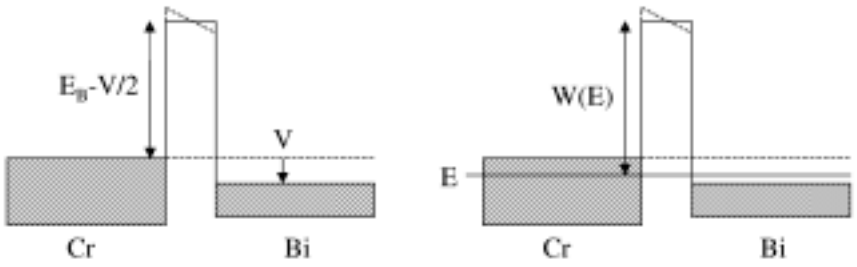

Figure 4-6: Energy band diagram of the Cr-oxide-Bi junction with the rectangular barrier approximation. Shown on the right diagram is the barrier height W relative to a state of energy E.

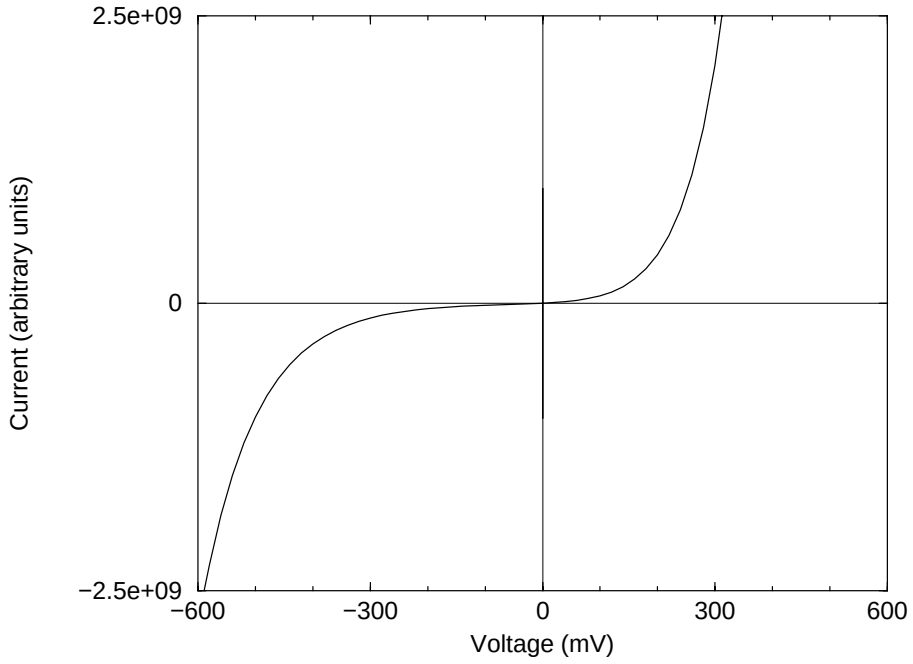

Figure 4-7: $i_{junct}(V)$ response of a Cr-oxide-Bi tunnel junction, assuming an oxide barrier height of 2eV and thickness 5nm. The current axis is plotted on a linear scale in arbitrary units.

WKB approximation, we determine the tunneling probability to be

$$T(E,V) \simeq e^{-2\sqrt{2mW/\hbar^2}a} = e^{-2\sqrt{2m(E_B - V/2 + E_F^{Cr} - E)/\hbar^2}a}. \tag{4.4}$$

Here W is the energy of the top of the barrier with respect to the state to be tunneled into. W can also be expressed as $E_B - V/2 + E_F^{Cr} - E$, where E_F^{Cr} is the Fermi energy of Cr and E is the energy of the tunneling state with respect to the bottom of the Cr conduction band.

Now that we have expressions for the integrands of eqs. (4.1) and (4.2), $i(V)$ of the Cr-oxide-Bi tunnel junction can be calculated. Results of $i_{junct}(V)$ are shown in figure 4-7, assuming the bulk Bi density of states and an oxide barrier of height 2eV and thickness 5nm. Because the exact geometry of the contact is not known, $i_{junct}(V)$ is in arbitrary units.

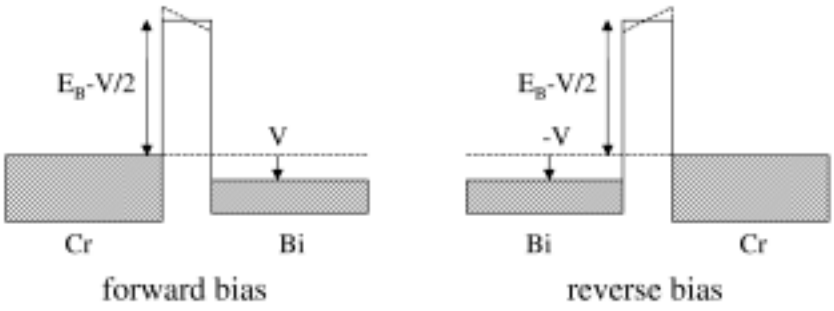

Figure 4-8: Energy band diagrams of the Cr-oxide-Bi junction and the Bi-oxide-Cr junction.

The asymmetry of $i_{junct}(V)$ is due to the dissimilarity of the Cr and Bi density of states. With a positive voltage applied, electrons tunnel from the very large Cr band into an essentially empty Bi band, resulting in a large current. Likewise, when a negative voltage is applied, the electrons tunnel from the very small Bi band to an essentially full Cr band, resulting in a small tunneling current.

In the actual 2-point measurements, discussed earlier in this chapter, there are two tunnel junctions in series, first a Cr-oxide-Bi junction at one end of the nanowire and then a Bi-oxide-Cr junction at the other end of the nanowire. As will be shown below, the series combination of two junctions will produce a symmetric $i(V)$ curve, as was observed experimentally. We could write down the forward and reverse tunnel currents for the Bi-oxide-Cr junction to get $i_{junct}^{\mathrm{Bi-ox-Cr}}(V)$, but that is not necessary. By recognizing the symmetry between the two junctions, we note that when the voltage offset between the Bi and Cr bands is reversed ($V \rightarrow -V$) and the density of states factors are reversed (forward $\leftrightarrow$ reverse), the two junctions are equivalent (see figure 4-8). So, $i_{junct}^{\mathrm{Bi-ox-Cr}}(V)$ is equal to the mirror image of $i_{junct}^{\mathrm{Cr-ox-Bi}}(V)$, that is,

$$i_{junct}^{\mathrm{Bi-ox-Cr}}(V) = -i_{junct}^{\mathrm{Cr-ox-Bi}}(-V). \tag{4.5}$$

Now that we have the $i(V)$ curves of both junctions, we take their series sum to get the $i_{total}(V)$ curve, which is equivalent to the 2-point $i(V)$ measurement. In

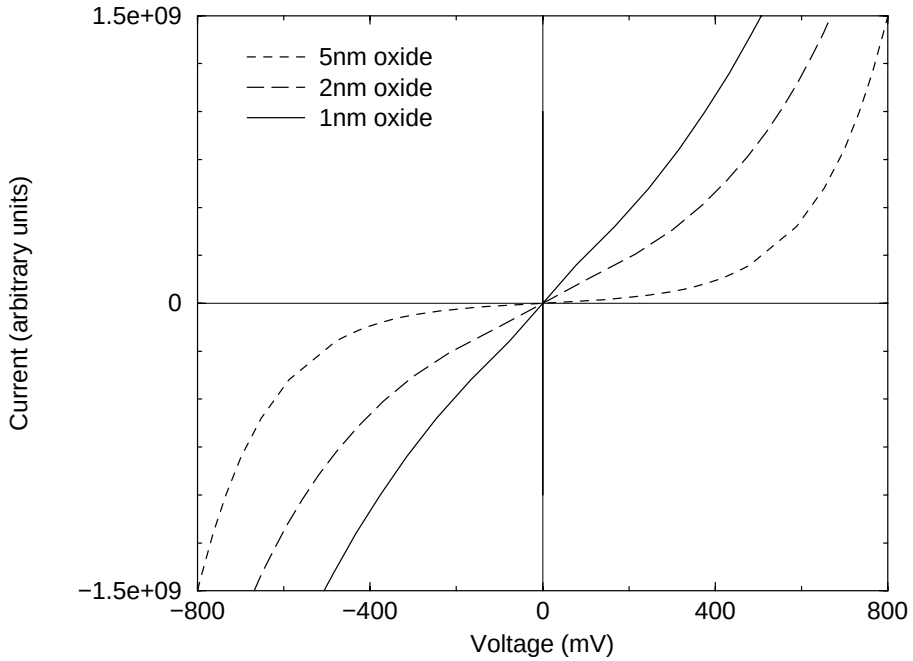

Figure 4-9: $i(V)$ response of two tunnel junctions, Cr-oxide-Bi and Bi-oxide-Cr, in series, for various oxide thicknesses.

series we equate the currents of the two junctions and sum the voltages. Doing this, we see the resulting $i_{total}(V)$ shown in figure 4-9. These $i(V)$ curves are symmetric, despite the fact that the $i(V)$ curves of the individual junctions are not. This is because the $i(V)$s of the junctions are mirror images of each other and so their series sum is symmetric. Both symmetric and asymmetric $i(V)$ responses are observed experimentally. If one considers two tunnel junctions with dissimilar oxide thicknesses the $i(V)$s of the junctions are no longer mirror images of each other and therefore result in an asymmetric $i(V)$ curve.

These calculated $i(V)$s have many of the features observed in the experimental 2-point measurements shown in figures 4-1, 4-2 and 4-3. For a thick oxide (5nm), we see a large flat region near zero current, as in the left graph of figure 4-2. For a 2nm oxide, we see an *S*-like curve similar to that of figure 4-1. And for a thin oxide (1nm) we see a nearly linear behavior, as in the experimental curve on the right of figure 4-2. The wide variation in the experimentally observed $i(V)$ curves can be explained

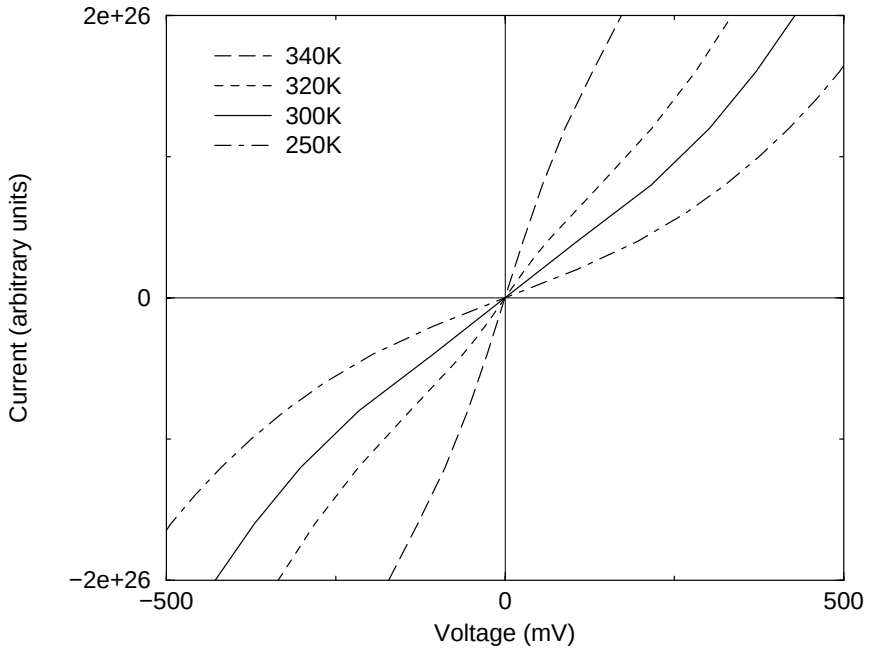

Figure 4-10: Temperature dependence of the $i(V)$ response of two tunnel junctions, Cr-oxide-Bi and Bi-oxide-Cr, in series, for 2nm oxide thicknesses.

by the tunneling model by varying the thickness of the oxide.

The temperature dependence of the $i(V)$ curves calculated using this model is also consistent with the experimentally observed temperature dependence. Figure 4-10 shows how the $i(V)$ response varies as a function of temperature. As in the experimental curve of figure 4-3, the curves become steeper and more linear as the temperature is increased. Again, the calculated results are qualitatively consistent with those observed experimentally.

4.2.2 Tunneling Contacts to Bi Nanowires

The above calculation showed that the non-ohmic behavior of the contacts can be explained by an oxide tunneling barrier. The bulk Bi density of states was assumed in this calculation. We would now like to extend this calculation to tunneling contacts to a Bi nanowire with a quantized band structure, and ask whether we can use these contacts in some way to probe the electronic properties of the nanowire. In particular,

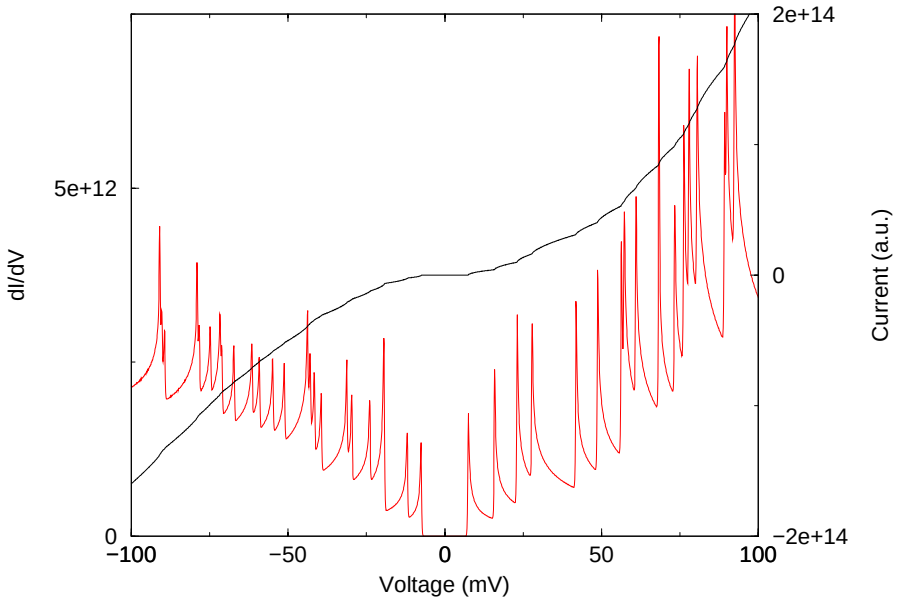

Figure 4-11: Calculated $i(V)$ response and its derivative for a single Cr-oxide-40nm diameter Bi nanowire tunnel junction at 1K, with an oxide barrier height of 2eV and thickness 2nm. The nanowire possesses a (012) crystalline orientation along the nanowire axis.

can we use these contacts to resolve the subband edges of the density of states?

In calculating the tunneling current to a Bi nanowire we need only change the density of states of Bi in the preceding calculation of section 4.2.1. All the equations of this last section are valid with the modification that the Bi density of states, $D_{Bi}(E)$, is now that of a nanowire with quantized subbands, calculated previously in section 2.3.

Figure 4-11 shows the calculated $i(V)$ response of a tunneling contact to a 40nm diameter Bi nanowire. Since the tunneling current is the integral of the density of states, its derivative is proportional to the density of states. For low temperatures, such that $k_B T <$ the width of the subbands $<$ 1meV, thermal broadening will not *smear* the subband features in di/dV. As can be seen from the figure, di/dV shows the subband structure very clearly with the same shape and energy of subbands as that of the density of states shown in chapter 2 in figure 2-4.

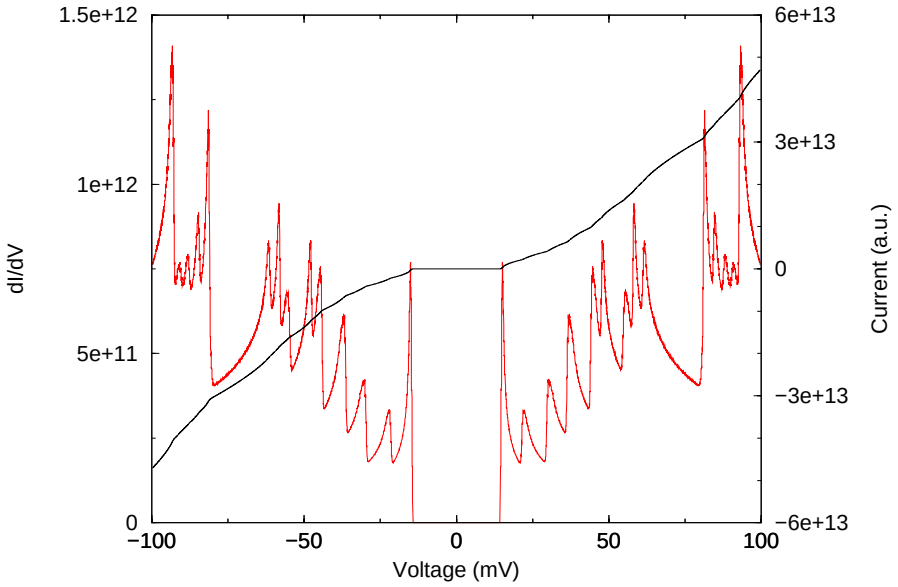

Figure 4-12: Calculated $i(V)_{total}$ response and its derivative for two tunnel junctions to a 40nm diameter Bi nanowire at 1K, with an oxide barrier height of 2eV and thickness of 2nm. The nanowire possesses a (012) crystalline orientation along the nanowire axis.

The above calculation is for one tunnel junction. As was mentioned in the previous section the series sum of the two tunnel junctions of the 2-point measurement, $i_{junct}^{\mathrm{Cr-ox-Bi(nano)}}(V)$ and $i_{junct}^{\mathrm{Bi(nano)-ox-Cr}}(V)$, must be taken to attain the total $i_{total}(V)$ corresponding to a two point measurement. The total $i(V)$ response of the 2-point measurement is shown in figure 4-12. We find that the $i(V)$ curve is symmetric, and that the energy of the peaks now corresponds to the sum of the hole and electron subband energies. Thus the first peak that occurs in $i(V)_{total}$ is at 15meV and corresponds to the bandgap between the first hole and first electron subband edges. That is, the energies of the peaks in figure 4-12 do not correspond to subband energies, but rather to energy gaps between electron and hole subband energies.

As the temperature is increased, the ability to resolve the subband edge peaks is reduced. We would like to know at what temperature thermal broadening will destroy the tunneling spectroscopy. Figure 4-13 shows the $i(V)$ response and its derivative for a 40nm diameter nanowire at 4K. The peaks are still easily recognized; however

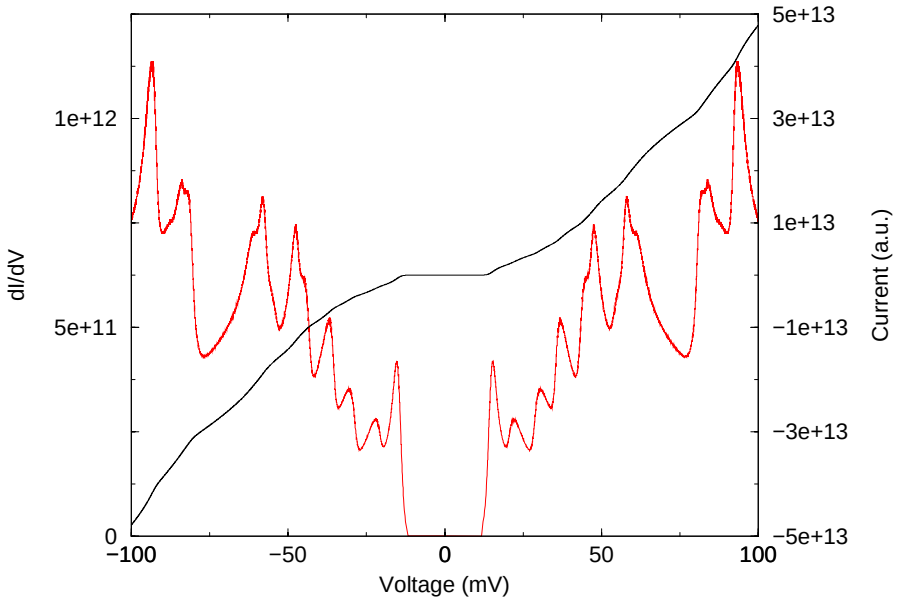

Figure 4-13: Calculated $i(V)_{total}$ response and its derivative for two tunnel junctions to a 40nm diameter Bi nanowire at 4K, with an oxide barrier height of 2eV and thickness 2nm. The nanowire possesses a (012) crystalline orientation along the nanowire axis.

the effects of thermal broadening can be seen. Although k_BT at 4K is only 0.3meV, the width of the peaks in di/dV appears to be at least ten times larger. This is because the $i(V)$ response of figure 4-13 includes two tunnel junctions, which are each broadened by the thermal energy. This increased broadening can be seen by comparing figure 4-11, the calculated response for only one tunnel junction at 1K, with figure 4-12 which is the response for 2 tunnel junctions at 1K. By comparing the figures we can see that the $i(V)$ response of one tunnel junction yields much sharper features than does the the $i(V)$ of two tunnel junctions. Also, because of the presence of $T(E,V)$ in the integrand of the equations for the current (4.1) and (4.2), di/dV is not simply equal to the density of states of the Bi nanowire.

At 77K the effects of thermal broadening have completely washed out the subband edge peaks from di/dV. The $i(V)$ response and its derivative of the same 40nm diameter nanowire at 77K are shown in figure 4-14. Normally we would expect to see some evidence for the 10.7meV band gap at this temperature (k_BT is 6.6meV).

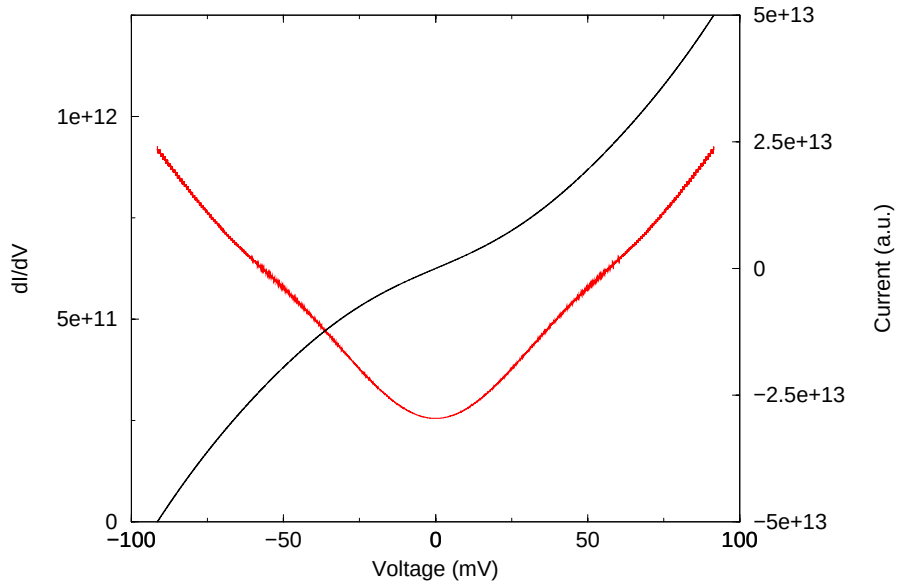

Figure 4-14: Calculated $i(V)_{total}$ response and its derivative for two tunnel junctions to a 40nm diameter Bi nanowire at 77K, with an oxide barrier height of 2eV and thickness 2nm. The nanowire possesses a (012) crystalline orientation along the nanowire axis.

However it is because of these additional *smearing* effects, discussed above, that the resulting di/dV curve appears smooth and featureless.

It has been determined that the quantized subband structure can be resolved by tunneling spectroscopy using the oxide barrier tunneling contacts. However, the temperature required for such resolution is quite low ($\sim$ 4K). Unfortunately the resistance of the contacts observed experimentally are found to increase exponentially with decreasing temperature, and no data could be taken at such low temperatures. From the temperature dependent $i(V)$s measured experimentally (see figure 4-3) we find that data could not be taken reliably below 225K.

Other possible means of measuring the van Hove singularities in the density of states of the nanowires are STM (scanning tunneling microscope), capacitance and optical measurements. Using an STM to tunnel electrons into a single nanowire, the same approach of measuring $i(V)$ and taking its derivative can be applied to measure the density of states. In capacitance measurements, insulating contacts patterned to

the nanowires can be used to measure the high frequency response of the nanowires. Since the capacitance is proportional to the density of states in the nanowire, this method can used to probe the van Hove singularities of nanowires. Since the single nanowire measurements prepared in this work were made on doped silicon substrates with a thin insulating layer of SiO_2, the large metal contact pads tended to have a very high capacitance. In order to measure the capacitance of the nanowires, care must be taken in preparing electrodes with low capacitance. Work is currently being carried out using optical methods to observe peaks in the absorption spectrum corresponding to transitions between the subbands [16].

4.3 Measurement of the Seebeck Coefficient of a Single Bi Nanowire

The Seebeck coefficient is essential in evaluating the potential of a material for thermoelectric applications. The Seebeck coefficient is measured by establishing a temperature gradient across the sample. A voltage is established across the sample as the charge carriers diffuse to the cold side. By measuring this voltage and the temperature gradient, the Seebeck coefficient can be determined, as $S = \Delta V/\Delta T$. The difficulty in measuring the Seebeck coefficient of the Bi nanowires lies in making small enough thermocouples to measure the temperature gradient over the short length of the nanowires. Since the alumina template is only 50μm thick and the smallest commercially available thermocouple is 25μm, a significant fraction of the measured temperature gradient will be across the contacts.

One way around the size limitation of the nanowires is to pattern the thermocouples on a substrate lithographically and measure a single Bi nanowire. An SEM image of this technique is shown in figure 4-15. On the left of the image there is a gold heater, which is used to establish a temperature gradient across the substrate. A Bi film has been evaporated across the top two electrodes, and serves as a reference sample to determine the temperature gradient. Since the Seebeck coefficient of the Bi

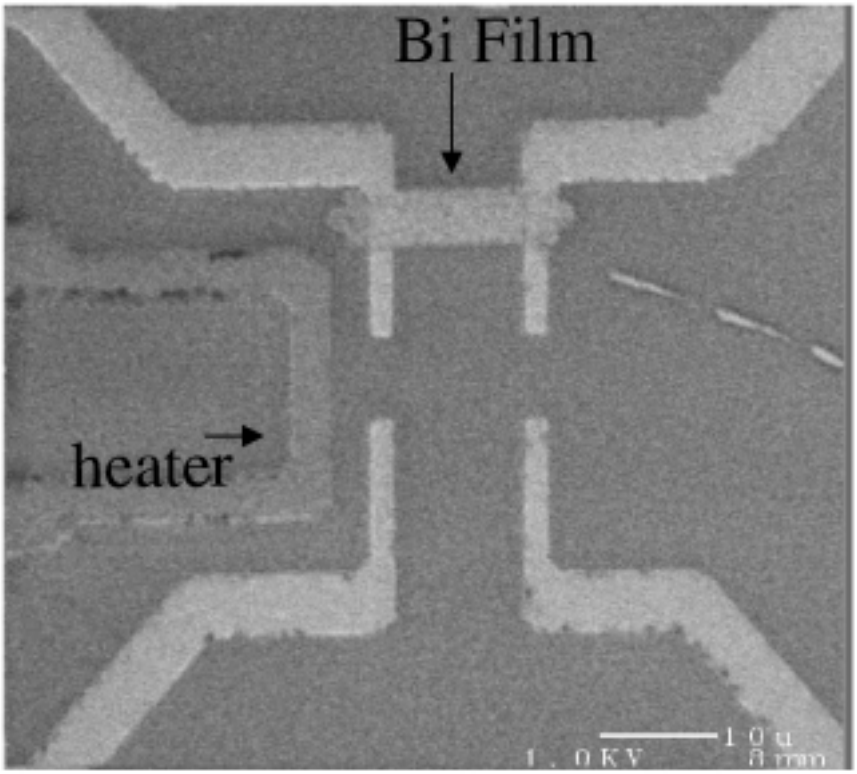

Figure 4-15: SEM image of differential Seebeck coefficient measurement scheme for measuring single Bi nanowires.

film is known, by measuring the voltage across this film and dividing by the Seebeck coefficient the temperature gradient can be determined. If the bottom two electrodes are patterned on top of a Bi nanowire (not shown in the figure), the Seebeck coefficient can be determined by measuring the voltage across the nanowire and dividing by the temperature gradient. It was found that, by applying current to the heater, a temperature gradient of 0.5K could be easily attained across the 10μm gap between the electrodes. This ΔT is sufficient for measuring the Seebeck coefficient.

This experiment was not carried out on actual Bi nanowires because the highly resistive contacts result in Seebeck voltage signals that are too noisy to measure. Instead we focused on the 4-point resistivity measurement, which has higher voltage signals, and concentrated on improving the quality of the electrical contacts. This is the topic of the next chapter.

Chapter 5

4-Point Measurements of Single Bi Nanowires

In chapter 3 we discussed how to pattern metal electrodes on a single Bi nanowire. In chapter 4 we found that an oxide layer caused the formation of poor non-ohmic contacts which prevented a reliable 4-point measurement from being made. In this chapter we discuss strategies for making good electrical contacts to oxidized Bi nanowires. Again, many of these strategies are applicable to other nanowire systems.

5.1 The Importance of 4-Point Measurements on 1D Systems

The simplest electrical measurement that can be done on Bi nanowires is to measure the whole Bi nanowire array by attaching contacts to both sides of a filled template using a thin gold wire and silver paint. This two-point measurement of a Bi nanowire array has the advantage of requiring no special equipment or handling/processing. However, because the number of nanowires contributing to the conduction is unknown, only the normalized resistance ($R(T)/R(300\text{K})$ and $R(B)/R(B = 0\text{T})$) can be measured, and not the absolute resistivity. The absolute resistivity can only be measured by determining the cross-sectional area and length of the conductors and

by eliminating the effect of the contact resistance. This can be done by performing a 4-point measurement of the resistance on a single Bi nanowire. 2-point measurements on Bi nanowire arrays have demonstrated the semimetal-to-semiconductor transition [13], discussed in chapter 2. However, to monitor the effects of doping and impurities quantitatively, 4-point measurements are essential. In bulk and 2D conductors, Hall effect measurements are the standard method for determining the carrier density and carrier scattering relaxation times. In a 1D conductor, however, Hall effect measurements are not possible and thus 4-point measurements are the most direct way of determining these extremely important quantities. Also, the determination of the absolute resistivity is essential to evaluate their potential for thermoelectric applications.

5.2 4-Point Resistivity Measurement with a Bias Current

In the last chapter (section 4.1) we showed that the oxide coating that forms on the free standing nanowires leads to very non-ohmic behavior that prevents a 4-point measurement from being taken. The non-linear $i(V)$ response of the contacts is such that the resistance is extremely high for very low currents. This non-linearity is indicated in the schematically drawn 'Contact I-V' curve in figure 5-1. Since there is very little current flowing through the inner voltage electrodes the effective resistance is extremely high, resulting in a very noisy signal. One way to overcome this limitation of the contacts is to apply a small constant current across the inner two electrodes, which will shift the $i(V)$ response of the contact away from the origin to a less resistive region. This is indicated schematically in figure 5-1. Varying the bias current results in a shift of the 4-point $i(V)$ curve by the amount $i_{bias} \times R_{contacts}$, but leaves the slope, and hence the measured resistance, unchanged. The shift of the 4-point $i(V)$ curve is indicated schematically in the bottom right of figure 5-1.

Figure 5-2 shows 4-point $i(V)$ measurements of the 70nm diameter Bi nanowire

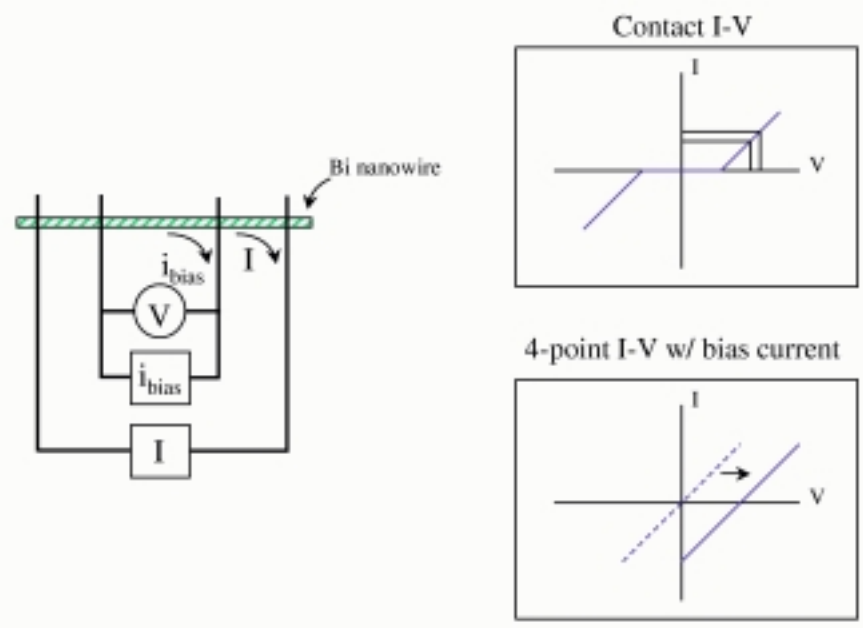

Figure 5-1: Schematic diagram of the 4-point resistance measurement with a bias current.

shown in figure 3-7. The rightmost curve (shown as squares in the figure) is data taken with a bias current of 6nA across the inner two electrodes and has a resistance of 7.8kΩ. The leftmost curve (shown as circles in the figure) is data taken with a bias current of 0nA across the inner two electrodes, that is, the current source was hooked up to the inner electrodes but set to zero current. This has the effect of stabilizing the inner voltage while running the minimum amount of current through the contact.[1] The voltage offset for this curve of about 1.5mV, is most likely due to the differing work functions of the Cr and Bi. If both electrodes were in good electrical contact with the nanowire, the difference in work functions would cancel each other. This leftmost curve has a resistance of 8.5kΩ. The distance between the inner two electrodes for this sample is 3μm. Multiplying the resistance by the cross-sectional area and dividing by the length of the nanowire we arrive at a resistivity of

[1] It may seem peculiar that the voltage is unmeasurably noisy without this current source attached, but is very stable with the current source attached and set to zero. However, the Keithley 220 current source, used in these measurements, has a small amount of current flowing at all times to check for an open circuit.

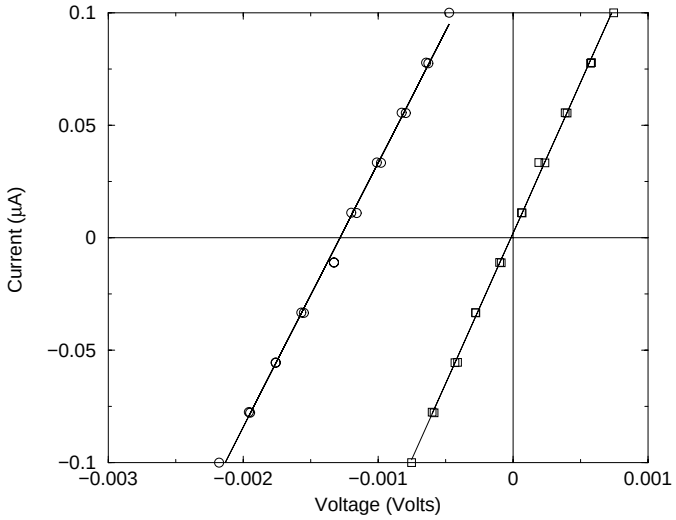

Figure 5-2: $i(V)$ curve for a 4-point measurement with bias current of 6 nA (squares) and a bias current of 0 nA (circles) for the 70 nm diameter Bi nanowire with four gold electrodes shown in Fig. 3-7.

$1.09 \times 10^{-3}\Omega$-cm, which is about nine times the bulk Bi value of $1.2 \times 10^{-4}\Omega$-cm.

Calculations based on the quantized band structure of the nanowires, described in section 2.3, show that for a 70nm diameter Bi nanowire there is no significant change in the carrier density due to the effects of quantum confinement at room temperature. Therefore, this factor of 9 increase in the resistivity with respect to bulk Bi must be due to increased scattering within the nanowire. This is reasonable since the diameter of the nanowire is smaller than the mean free path of the electrons in bulk Bi, which is on the order of 150nm at room temperature [13]. We therefore attribute the increase in the resistivity to increased scattering of carriers at the wire boundary and grain boundaries within the nanowire.

Figure 5-3 shows a 4-point $i(V)$ measurement of another 70nm diameter Bi nanowire with a bias current across the inner two electrodes of 0 nA. The deviation from the linear fit can be seen in the graph, showing that the $i(V)$ curve is not as linear as that of the figure 5-2. The fit yields a resistance of 14.6kΩ. In this sample the distance between the inner electrodes was 5μm, giving a resistivity of $1.12 \times 10^{-3}\Omega$-cm, which is about 9.4 times the bulk resistivity. Despite the non-linear behavior of this $i(V)$

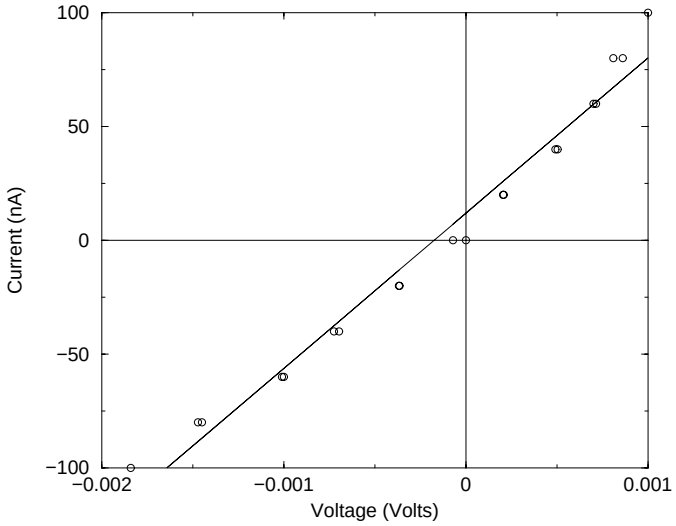

Figure 5-3: $i(V)$ curve for a 4-point measurement with bias current of 0 nA for a different 70 nm diameter Bi nanowire than is shown in Fig. 3-7 with four gold electrodes.

curve, the resulting resistivity is in very good agreement with that of the sample of figures 3-7 and 5-2.

It should be mentioned that many samples were prepared and tested in this work. Most of the samples were either completely unmeasurable due to high contact resistances, or had highly non-linear 4-point data that could not be interpreted. Figure 5-4 shows the 4-point $i(V)$ curves taken on a 70nm diameter Bi nanowire with various bias currents. The graph shows highly non-linear 4-point $i(V)$ curves that are typical. The resistances of these curves are on the order of 10MΩ, which implies an extremely high resistivity. However, because of the strange shape of the $i(V)$ curves, the effect of the bias current cannot be understood in terms of the simple model of figure 5-1.

The modification of the 4-point measurement by applying a bias current across the inner electrodes allowed us to attain resistivity measurements of two samples that were otherwise, unmeasurable. However, the vast majority of the samples were not measurable by this technique and in some cases this unconventional technique yielded unexpected results that could not be explained. In order to get reliable resistivity data, we must reduce the oxide on the nanowire. The rest of this chapter will focus

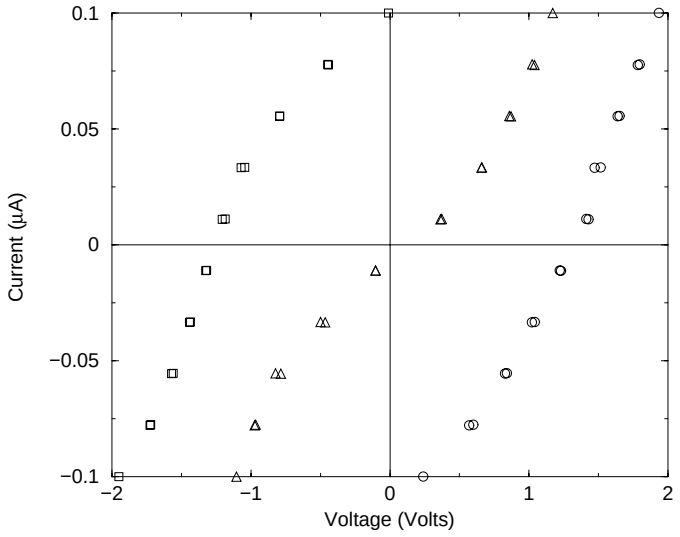

Figure 5-4: $i(V)$ curve for a 4-point measurement with bias current of -1 nA (squares), 0 nA (triangles), and +1 nA (circles) for a 70 nm diameter Bi nanowire (a different sample than those of figures 3-7, 5-2 and 5-3) with four gold electrodes.

on this issue.

5.3 Strategies for Removing Oxide from Bi Nanowires

5.3.1 Wet Chemistry

Ideally we would like to find some sort of *magical* chemical that could dissolve the oxide rapidly while leaving the Bi nanowires intact. It would also be desirable if the chemical could passivate the surface and prevent it from re-oxidizing in air. Such chemicals exist for other materials. For instance, HF acid is used to dissolve SiO_2 as well as passivate the surface of the underlying Si. Since Si oxidizes very rapidly in air, an acid dip in HF is always done before making contacts to Si. In Bi however, no such *magical* chemical is known. Moreover, the chemical reactivity and stability of Bi available in the literature is based on observations of bulk Bi, which is quite different from bismuth's behavior on the nanoscale.

In our first attempt to remove the oxide layer from the Bi nanowires, we tried to

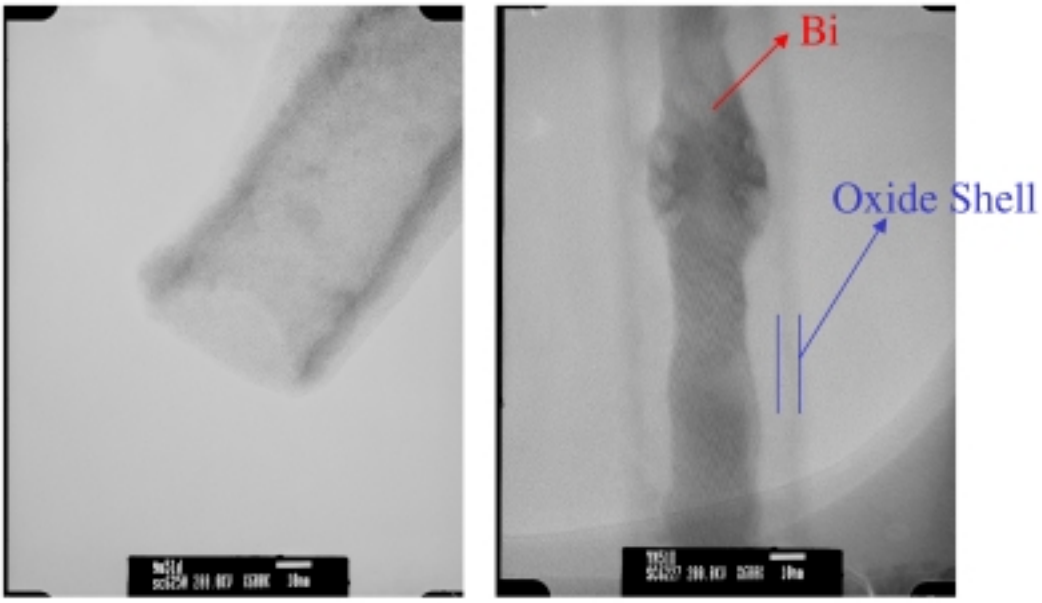

Figure 5-5: HRTEM (high resolution transmission electron microscope) image of 40nm diameter Bi nanowires after a 3 second acid dip in 10:1 diluted HCl. The left image shows the remaining empty oxide shell. The right image shows a partially dissolved Bi core inside an oxide shell.

etch the nanowires in an acid solution. Figure 5-5 shows an HRTEM image of 40nm Bi nanowires after an acid dip in 10:1 diluted HCl for 3 seconds. The image shows that the Bi was dissolved while leaving the oxide shell intact. Several other acids were tried, HF, H_2SO_4, H_3PO_4, and HNO_3, and at various concentrations, but all yielded similar results. Basic solutions of KOH and NaOH were also tried, but again were found to dissolve the Bi core and not the oxide coating. It wasn't until these observations were made that we realized the extreme chemical sensitivity of the Bi on the nanoscale and the extreme chemical resilience of its oxide coating.

Despite the fact that this is an interesting result, it did not yield clear insights for making good electrical contact to Bi nanowires. In fact this experiment reveals some rather discouraging results with regard to finding a wet chemistry solution to the oxide problem. So we investigated other strategies for removing the oxide.

5.3.2 Hydrogen Annealing

As a second attempt to remove the oxide from the nanowires, we annealed the nanowires in hydrogen gas. We used an environmental-HRTEM (environmental-high resolution transmission electron microscope) in the DuPont Research and Development Center developed by Dr. Pratibha Gai. This environmental-HRTEM system allows one to flow hydrogen gas through the sample chamber at elevated temperatures, while imaging the reaction on an atomic scale. We found that after flowing hydrogen through the sample space at 130°C for 6 hours, we were able to completely reduce the oxide. Figure 5-6 shows the HRTEM images before and after the hydrogen annealing. The left image of figure 5-6 shows crystalline bismuth, below which appears the amorphous oxide layer, as indicated next to the figure. After hydrogen annealing, shown in the right side of figure 5-6, the oxide has been successfully removed and there is a clean crystalline interface at the surface of the nanowire. The same result was also achieved when we repeated the experiment with ammonia gas instead of hydrogen gas.

From a thermodynamics standpoint, the reduction of the oxide can be understood by considering the following chemical reaction

$$Bi_2O_3 + 3H_2 \rightarrow 2Bi + 3H_2O. \tag{5.1}$$

By comparing the sums of the energies of formation of the products and reactants, we find the products to be more stable than the reactants. Therefore, there must be a high activation energy prohibiting this reaction from occurring at room temperature. From the long time required for the oxide layer to be removed (6 hours), we conclude that the activation energy is significantly larger than 35meV ($= k_B T$ at 130°C).

Although we have successfully removed the oxide from the Bi nanowires, this method must be applied to the 4-point resistance measurement. This requires that the 6 hour hydrogen (or ammonia) anneal be done right before the deposition of metal electrodes, while maintaining a high vacuum to prevent the oxide from reforming on the nanowire.

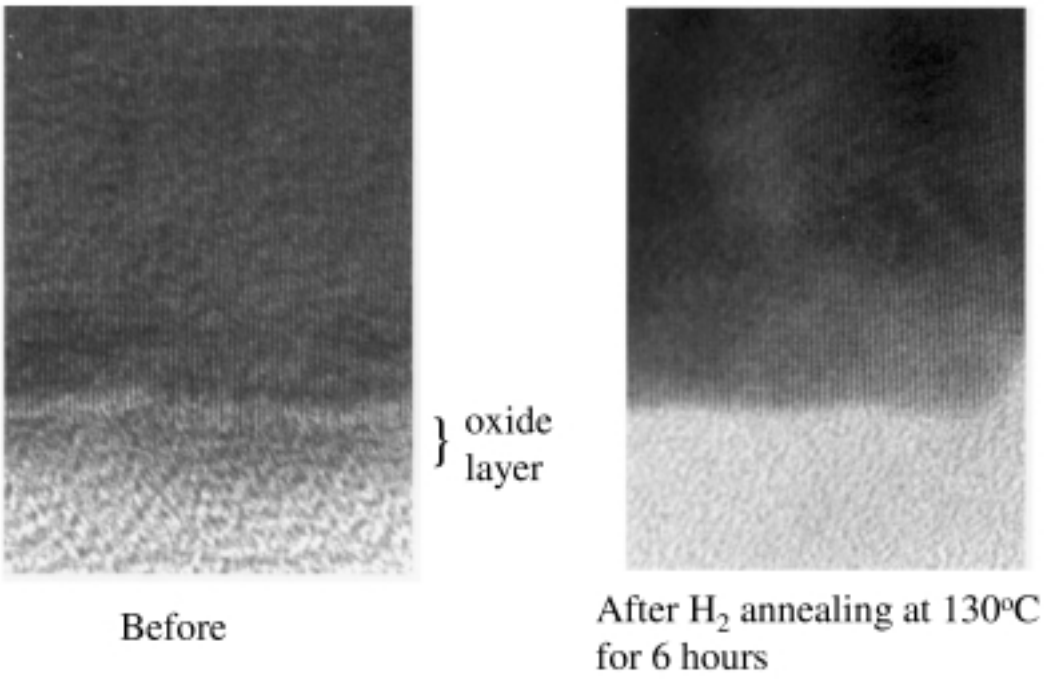

Figure 5-6: High resolution transmission electron microscope (HRTEM) image of a Bi nanowire (left) before and (right) after annealing in hydrogen gas at 130°C for 6 hours.

In this work an electron beam evaporator was modified to flow hydrogen through the sample chamber while the sample is mounted on a heated stage.[2] It was found that the lithographic mask cannot withstand the prolonged high temperatures required to reduce the oxide. That is, the lithographic process of patterning 4 electrodes on top of a Bi nanowire is incompatible with this annealing process. Several alternative lithographic processes were proposed to overcome this temperature limitation, but all were discarded because of the high chemical sensitivity of the Bi nanowires which requires that only chemicals with a pH near 7 come in contact with them.

5.3.3 FIB (focused ion beam) Milling/Deposition

Our third approach finally allowed us to make low resistance ohmic contacts to the nanowires by using a focused ion beam (FIB) to first sputter away the oxide layer with gallium ions and then deposit platinum electrodes by introducing a Pt-hydrocarbon gas in the path of the Ga ion beam. This work was done at Harvard University in collaboration with Prof. Charles Lieber and Dr. Thomas Rueckes. A schematic diagram of this technique is shown in figure 5-7. Both steps are carried out *in situ* without breaking vacuum.

Figure 5-8 shows a sequence of images of a 200nm Bi nanowire after successive scans with the Ga ion beam. The effects of sputtering can be seen as the bright oxide coating is significantly removed in going from the first to the sixth frame. The parameters used for Ga ion milling were to scan a 1.5μm x 1.5μm field 5 times with 10pA at 30kV acceleration voltage and at a rate of 1 second per scan.

This ion sputtering technique of oxide removal was repeated at four places along the nanowire in the selected areas where electrodes were to be attached. Once the oxide had been significantly removed from the nanowire in the contact areas, a small amount of Pt-hydrocarbon gas was introduced above the sample and Pt electrodes were deposited by rastering the Ga ion beam to form the pattern of the electrodes. An SEM image of a 200nm diameter bismuth nanowire prepared using this technique

[2]This work was done in collaboration with Prof. Jean-Paul Issi at the Catholique Universite de Louvain in Belgium.

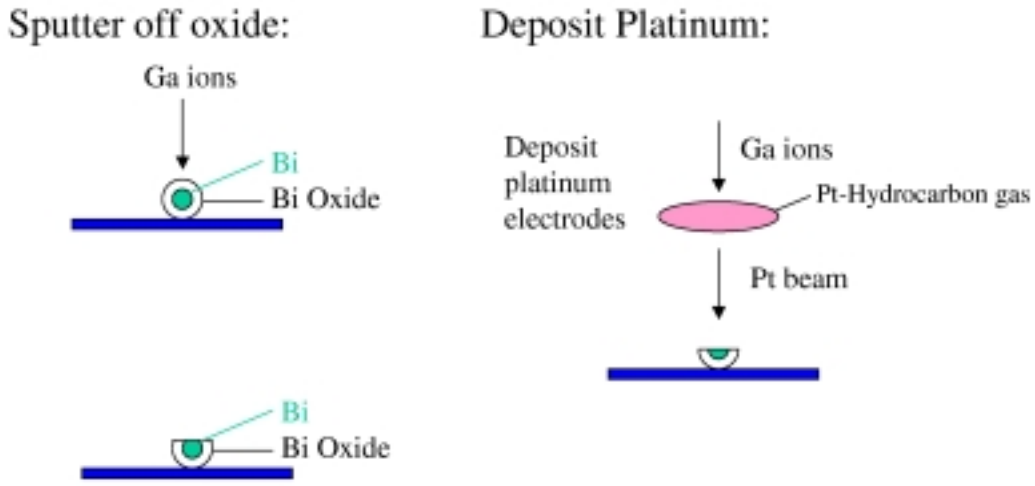

Figure 5-7: Schematic diagram of the technique used to make electrical contacts to the Bi nanowires by first sputtering with the focused Ga ion beam and then depositing Pt for the electrodes.

is shown on the right side of figure 5-9. The stick-like lines are the Pt electrodes and the wide strips attached to the Pt wires are gold electrodes, which in turn are attached to 4 large bonding pads (not shown) patterned by photolithography.

The nanowire sample of figure 5-9 has a diameter of 200nm and the distance between the inner electrodes is 6.9μm. The contact resistance was found to be 4kΩ and the sample resistance was found to be 413Ω, using this 4-point method, yielding a resistivity of 1.9x10$^{-4}\Omega$-cm. This result is only slightly higher than the resistivity of bulk Bi, 1.2x10$^{-4}\Omega$-cm, indicating that there is no significant quantum effect on the band structure and no significant increase in the scattering due to wire boundary or defect scattering relative to bulk, as expected for a wire with such a large (200nm) diameter. This very low resistivity indicates that the crystal quality of the bismuth nanowires is very high, as was also found in the atomic resolution transmission electron microscopy of figure 3-5.

Electrodes were patterned on another 200nm diameter Bi nanowire using the same technique and this particular nanowire is shown in figure 5-10. Low resistance ohmic contacts were achieved again across all four electrodes. The 4-point resistance of this

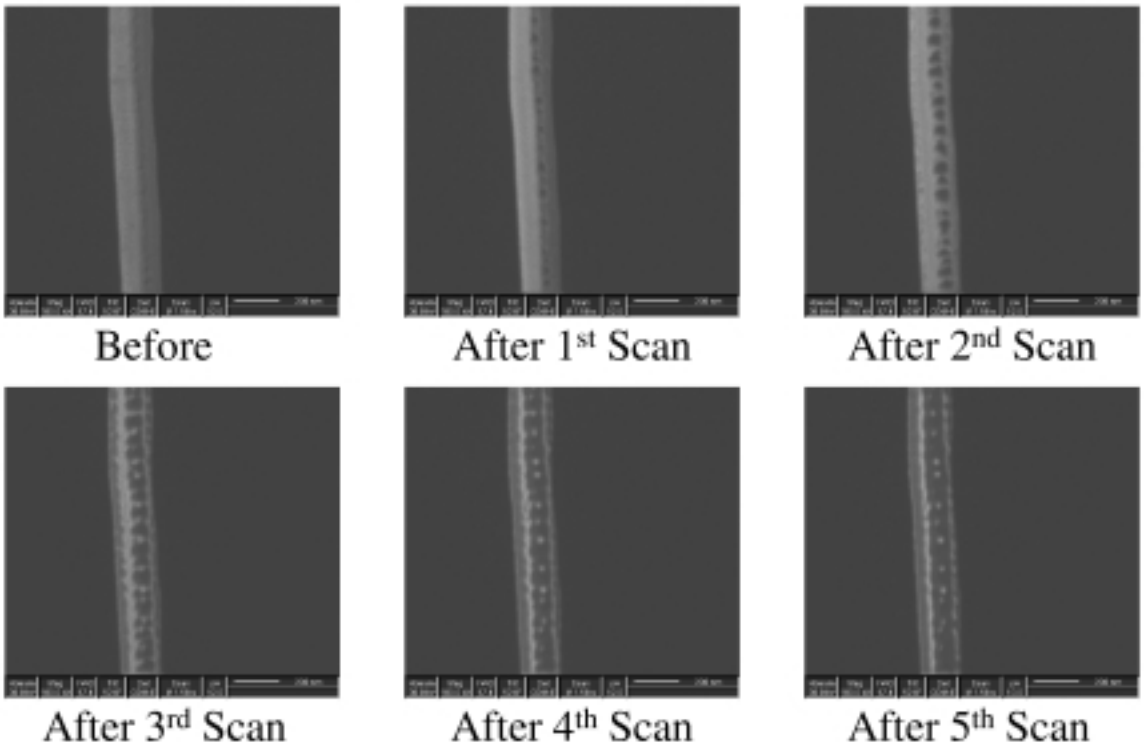

Figure 5-8: Removing the oxide coating on a 200nm Bi nanowire by successive scans with a focused Ga ion beam.

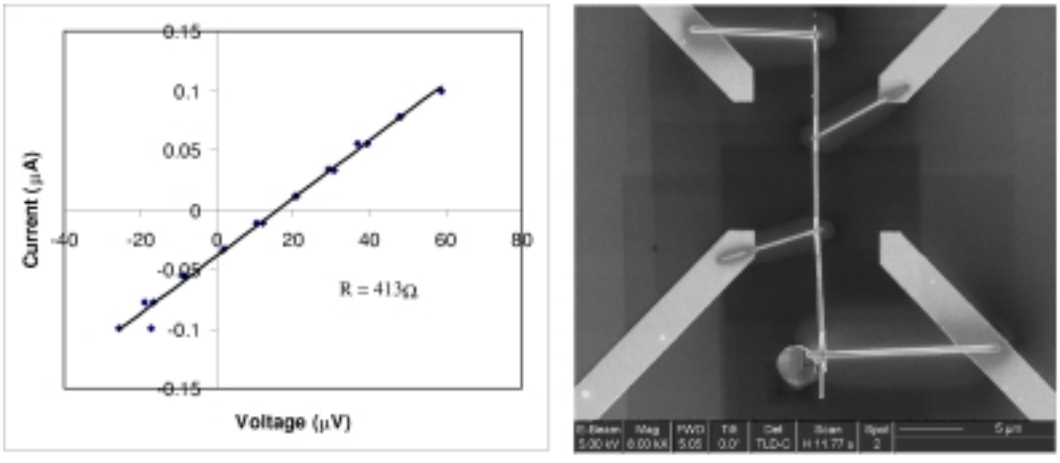

Figure 5-9: Right: SEM image of a 200nm Bi nanowire with 4 platinum electrodes prepared using FIB. Left: 4-point $i(V)$ curve taken at room temperature for the sample on the right.

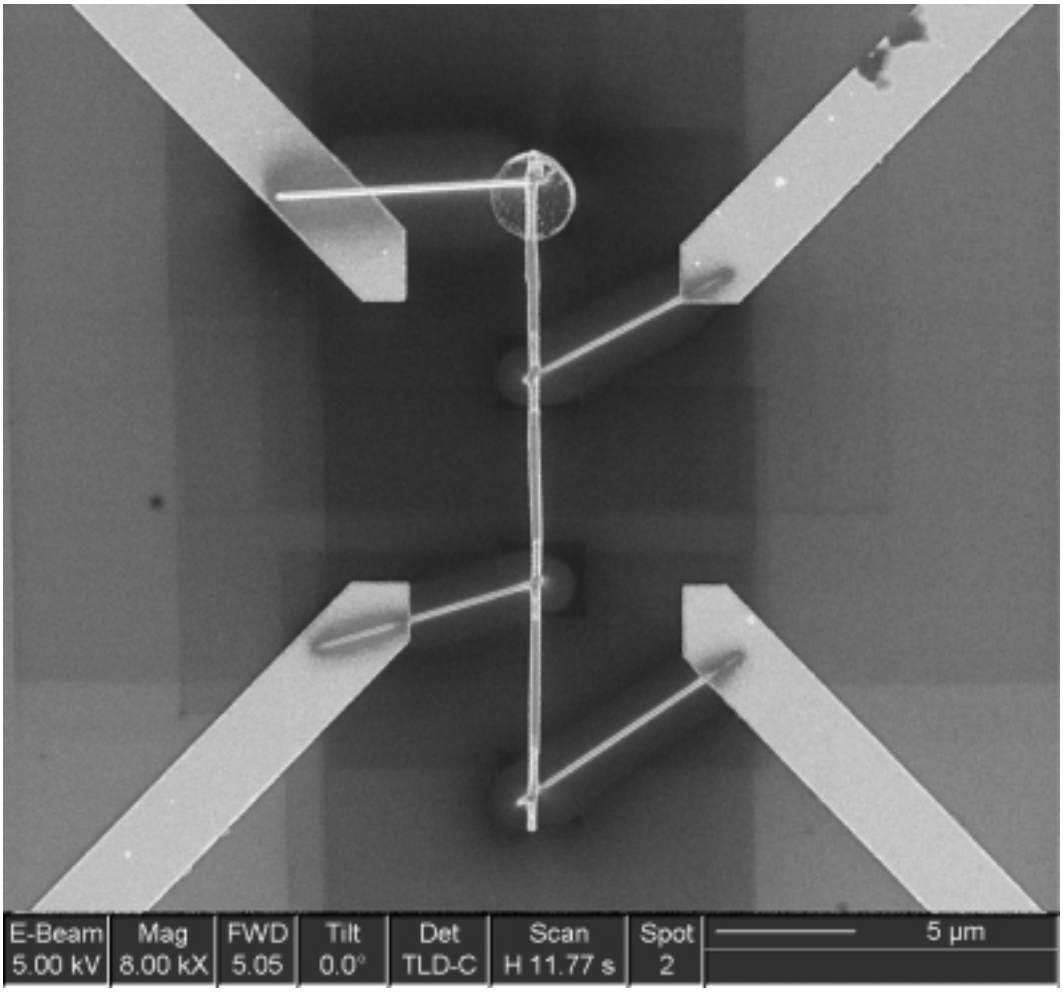

Figure 5-10: SEM image of another 200nm Bi nanowire with 4 platinum electrodes prepared using FIB.

sample was found to be 570Ω. For a diameter of 200nm and length between inner electrodes of 6.2μm, this yields a resistivity of 2.9x10^{-4}Ω-cm, which is considerably higher than the previous measurement. This raises the question of whether or not this discrepancy is due to sample to sample variation or to some systematic error in the measurement. This topic will be addressed in detail in section 5.3.5.

The same technique of Ga ion milling and then depositing Pt electrodes was used on a 100nm diameter nanowire. The results are shown in figure 5-11. The resistivity of this sample is found to be approximately 6 times larger than that of bulk Bi at

room temperature. This indicates that there is increased scattering in the nanowires relative to bulk, at the wire boundary and by grain boundaries within the nanowire. Also the temperature dependence of the resistivity is very different from that of bulk Bi. In bulk Bi, phonons are the dominant scattering mechanism which cause the resistivity to increase with temperature. In the 100nm nanowire, however, the scattering is dominated by boundary scattering, which is temperature independent. Assuming a temperature independent scattering time, τ, we can write the resistivity of the nanowire in terms of its temperature dependent quantities

$$\rho(T) = \frac{1}{ne\mu} = \frac{m(T)}{n(T)e^2\tau}. \tag{5.2}$$

In bulk Bi the effective mass is strongly temperature dependent and varies by a factor of $m(300\text{K})/m(240\text{K}) = 1.94$ over the measured temperature range. Using the quantized band structure model, presented in chapter 2, we calculate the carrier density of a 100nm Bi nanowire to vary by a factor of $n_{100nm}(300\text{K})/n_{100nm}(240\text{K}) = 2.3$ over the measured temperature range. In bulk Bi the ratio is $n_{bulk}(300\text{K})/n_{bulk}(240\text{K}) = 2.2$. Although the carrier density inside the nanowire is reduced to half that of bulk due to quantum confinement, the temperature dependence is very similar. This is because the energy overlap of the valence and conduction bands, in both bulk and in the nanowire, changes dramatically in this temperature range. And it is this change in overlap energy that dominates the temperature dependence of the resistivity. The calculated $m(T)$ and $n_{bulk}(T)$ yield a theoretically predicted value for $\rho(240\text{K})/\rho(300\text{K})$ of 1.19. This is in almost perfect agreement with the experiment value of 1.16, indicating the validity of our model.

We were unable to extend this technique of making contacts to nanowires with diameters smaller than 100nm. For small diameter nanowires ($\sim$ 40nm) the oxide is a significant fraction of the wire diameter. And since the oxide is a relatively hard material and the Bi a relatively soft material, the oxide will sputter at a much slower rate than the Bi. In the case of a small nanowire diameter, once the oxide is significantly removed, the Bi is depleted immediately.

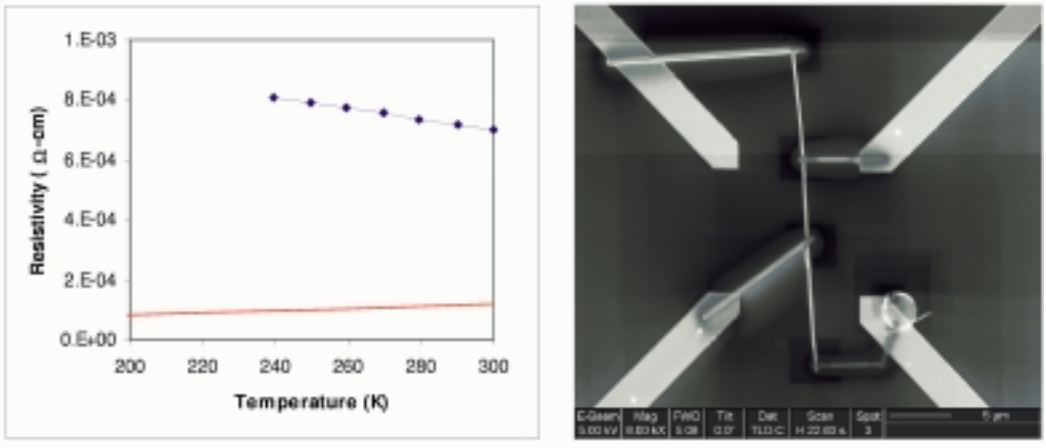

Figure 5-11: Left: The temperature dependence of the resistivity of a 100nm diameter Bi nanowire compared to that of bulk Bi. The contact failed below 240K. Right: SEM image of the 4-point electrodes patterned on the 100nm diameter Bi nanowire.

To make contacts to nanowires with diameters smaller than 100nm, we modified our technique by first patterning gold electrodes on top of the nanowire. We then ion milled a small hole in the contact region and filled the hole with Pt using the focused ion beam. Figure 5-12 shows SEM (scanning electron microscope) images of these two steps in the preparation of contacts using this technique on a 40nm diameter Bi nanowire.

This post-lithography ion milling technique was first used to measure the 4-point resistivity of a 200nm diameter Bi nanowire in the temperature range 200-350K. The resistivity data are shown in figure 5-13. The resistivity is found to be more than three times that of bulk Bi, increasing the spread in the measured resistivity of samples of the same nominal wire diameter. The resistivity is again found to be decreasing with temperature, as was the case for the 100nm diameter nanowire prepared using the previous ion milling technique. Again, we attribute this temperature dependence to be due to the increased scattering relative to bulk Bi at the wire boundary, grain boundaries and defect sites.

Figure 5-13 shows the results of 4-point resistivity measurements for samples of 70, 100 and 200nm in diameter prepared by various techniques of attaching the electrodes. The resistivity of these samples increases with decreasing diameter, as expected, since

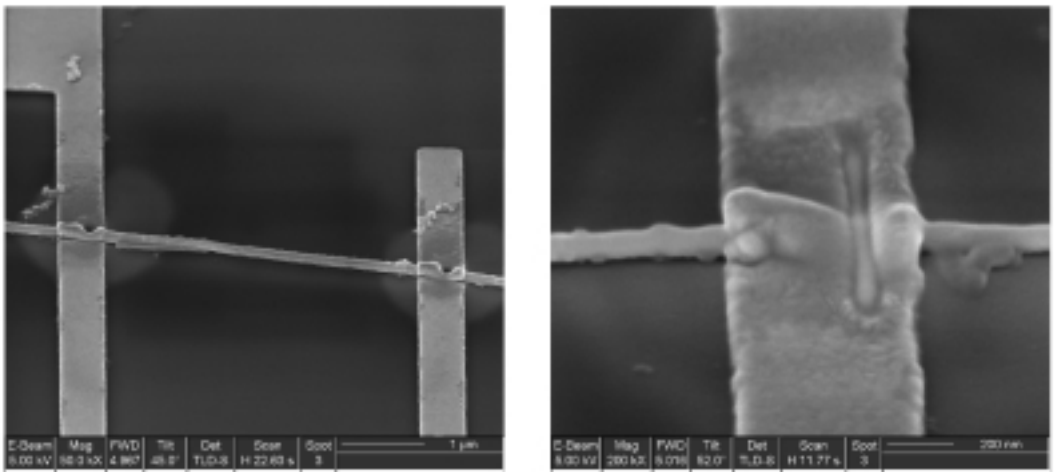

Figure 5-12: Left: Two gold electrodes patterned on a 40nm diameter Bi nanowire using electron-beam lithography after a hole has been milled in the contact region by a focused Ga ion beam. Right: A close-up of the contact region after the hole has been filled with Pt.

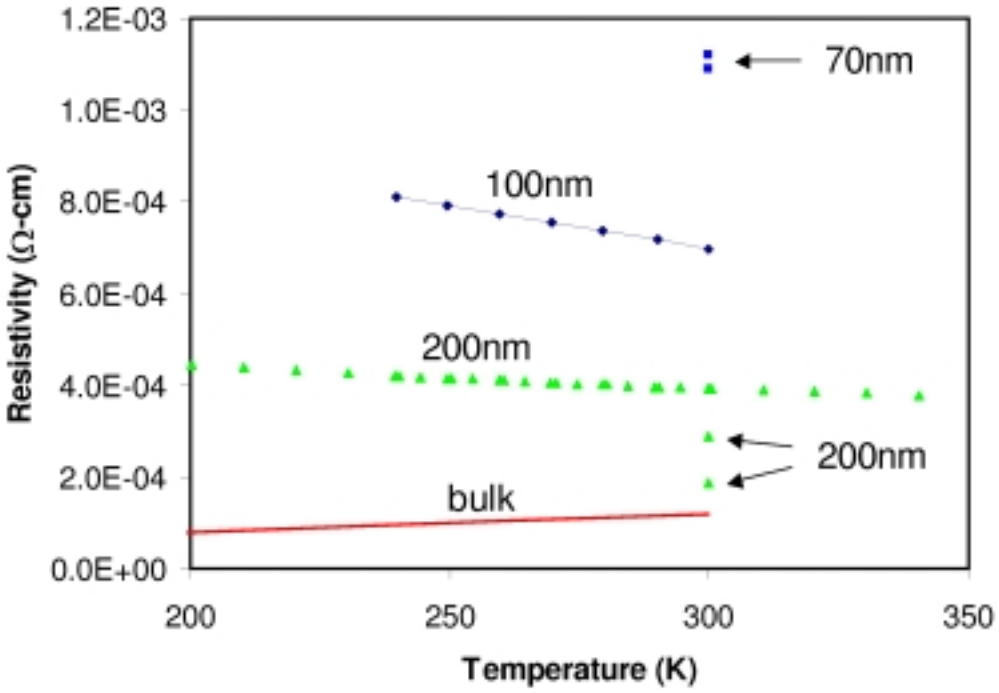

Figure 5-13: 4-point resistivity measurements of single Bi nanowires compared to that of bulk Bi.

the smaller nanowire diameters limit the electron mean free path. The effects of quantum confinement are not expected to significantly affect the band structure of nanowires of 70-200nm diameter at room temperature. The temperature dependence of the 100 and 200nm diameter nanowires are in contrast to the bulk Bi result, as expected from the change in the dominant scattering mechanism from phonon scattering to wire boundary, grain boundary and defect scattering as discussed above. However, the large spread in resistivities measured for samples of the same diameter, namely the 200nm diameter nanowire samples, questions the reliability of the measurement technique. Possible sources for this error are discussed in section 5.3.5.

5.3.4 Correction to the Nanowire Diameter for the Oxide Coating

As was shown in figure 3-5, an oxide of thickness 7nm is observed on the surface of Bi nanowires. The crystalline Bi core of a 40nm nanowire is reduced by this oxidation to a diameter of 26nm after removing it from the alumina template. The resistivities discussed thus far have been determined using the nominal diameters, that is, the diameters of the nanowires in the alumina template. However, subtracting twice the thickness of the oxide (14nm) from the nominal diameter will yield a more realistic value of the resistivity. This correction will be more significant for nanowires of smaller diameter, since the thickness of the oxide is a larger fraction of the nanowire diameter. Figure 5-14 shows a schematic drawing of the cross-section of an oxidized nanowire, indicating the corrected and nominal diameters. Table 5.1 lists the nominal and corrected values of the diameters and resistivities of the data presented in figure 5-13 at room temperature.

For the 70nm diameter nanowires, the resistivity is decreased by 36%, making the corrected resistivity only 5.7 times larger than that of bulk Bi. For the 100nm diameter nanowire the resistivity is decreased by 26%, making the corrected value 4.2 times larger than the bulk value. The 200nm diameter resistivities are found to change by %13. As shown here, a small correction in the diameter can lead to a large

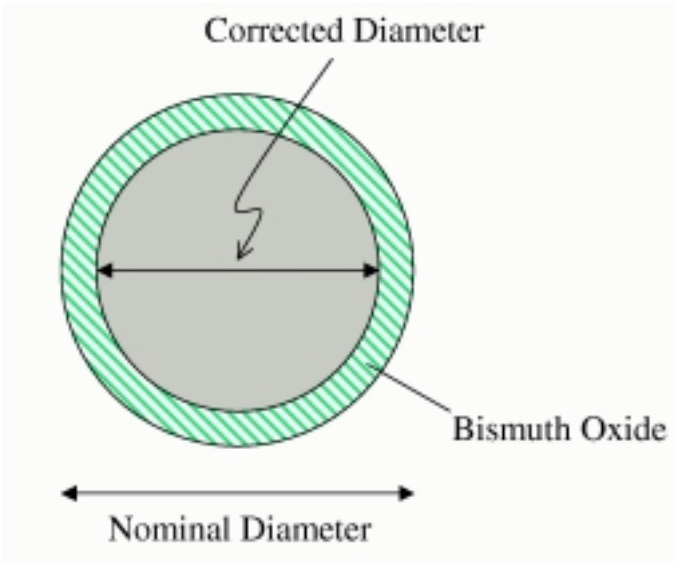

Figure 5-14: Schematic diagram showing the cross-section of an oxidized Bi nanowire, indicating the nominal and corrected diameters.

Table 5.1: Nominal and corrected Bi nanowire diameters and resistivities in nm and Ω-cm, respectively, at room temperature.

Nominal Diameter	Nominal Resistivity	Corrected Diameter	Corrected Resistivity
70	$1.09\times10^{-}3$	56	$6.98 \times 10^{-}4$
70	$1.12\times10^{-}3$	56	$7.17 \times 10^{-}4$
100	$6.98\times10^{-}4$	86	$5.16 \times 10^{-}4$
200	$3.93\times10^{-}4$	186	$3.4 \times 10^{-}4$
200	$2.88\times10^{-}4$	186	$2.49 \times 10^{-}4$
200	$1.88\times10^{-}4$	186	$1.63 \times 10^{-}4$

correction in the resistivity since the resistivity scales with the square of the diameter. From the corrected resistivity results we conclude that scattering in the nanowires is less than was previously thought. However, scattering is still found to increase as the diameter is decreased, and wire boundary and grain boundary scattering are believed to be the dominant scattering mechanisms.

5.3.5 Problems with FIB

One problem with depositing platinum using the focused ion beam is the very large spread in the beam. The Ga ion beam can be focused very finely by using charged particle optics. The Pt beam, however, is generated only slightly above the sample, and is therefore not focused. Because the Pt beam is generated by the interaction of the Ga ion beam with a stationary Pt-hydrocarbon gas, there is a large spread in the Pt beam, which leads to a thin halo of Pt deposited around the Pt written features. Figure 5-15 shows that this Pt halo can extend over 1 micron beyond the intended location of the deposition. For electrodes that are very close to one another, these halos can overlap, causing a shorting of the electrodes. In the instance of overlapping halos, we typically do post-deposition ion milling of the overlap area, as shown in the right image of figure 5-15. Although this milling does decrease the amount of shorting between electrodes, there is still an area very close to the nanowire that is not milled and will result in some slight shorting. This shorting will result in an underestimation of the nanowire resistivity.

Other sources of error in the measurements are the defects and Ga impurities along the length of the nanowire caused by the highly energetic Ga ions incident on the nanowire away from the contact areas, which causes an increase in the resistivity and results in an overestimate of the actual resistivity. In order to perform ion milling that is precisely aligned with the nanowire, the nanowire must first be imaged with the Ga ion beam, in much the same way an SEM image is produced, which requires several scans of the entire nanowire. The true extent of the damage to the nanowire is unknown, but it is believed to be significant. It is known that the resistivity of Si nanowires can be increased by 3 orders of magnitude by this Ga ion radiation. It

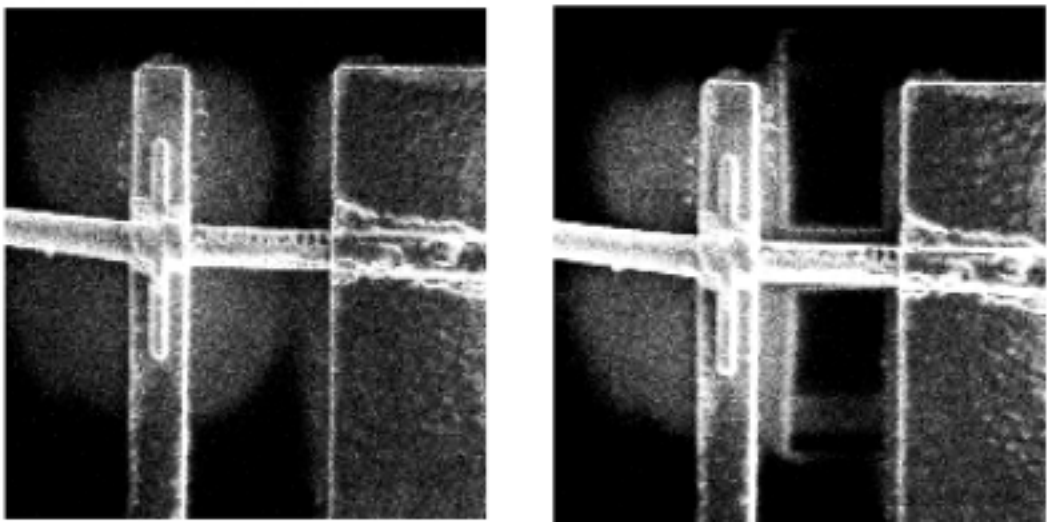

Figure 5-15: Left: SEM image of two close electrodes where the overlap of the Pt halos is significant. Right: The same contact area as on the left after ion milling of the Pt overlap area.

was also found that the photoluminescence of InP nanowires is completely destroyed, even by one scan of the Ga ion beam. I believe that it is these competing effects which cause errors in the measurements and account for the spread in the measured resistivity of nanowires with the same diameter.

Although the Ga ion radiation damage is expected to increase the resistivity of the Bi nanowires, the Bi nanowires are not expected to be as sensitive to this Ga ion radiation as the InP and Si nanowires. In a photoluminescent process in InP an electron-hole pair is created and a photon is emitted by the recombination of the electron-hole pair. The lifetime of this electron-hole pair in InP is very long, $\sim$1ns. If the electron-hole pair is scattered by a defect or impurity before it decays no photon will be emitted. It is believed that the scattering time of the electron-hole pairs in the InP nanowires exposed to Ga ion radiation is decreased below that of the lifetime for the photon to decay, thus destroying the photoluminescence. The Si nanowires, likewise, are expected to have a very high quality, defect-free crystal structure. Thus any defects or impurities introduced in the nanowires by the radiation damage will cause an increase in the resistivity. The Bi nanowires, however, are observed to have

defects and grain boundaries in their crystal structure before exposure to the Ga ion radiation. Therefore the defects introduced by the Ga ion radiation will not increase the resistivity significantly unless the density of defects is substantially larger than the pre-existing defect density. Even though the effect of the Ga ion radiation may not be as important as for the Si and InP nanowires, it could still be one reason for getting different resistivity values.

One possible solution to the problem of using FIB is to pattern a protective lithographic mask that would only expose the area of the contact region. After ion milling and Pt deposition, this mask could be removed, together with the undesired Pt halo. Although this method is yet to be tested, this protective mask could prevent the shorting of adjacent electrodes and reduce the radiation exposure along the length of the nanowire, away from the contact region. The FIB is a very powerful tool with amazing capabilities, but it's mechanisms are complex, and it is important to know what is happening at the atomic level in order to understand what it is that is being measured.

5.3.6 Alternative Chemical Dissolution of the Alumina Template

The chemical process by which the Bi nanowires are removed from the alumina templates is complex, and the mechanisms involved were not fully understood initially. The alumina template is quite resilient chemically, whereas the nanowires are very chemically sensitive. It is therefore a difficult task to dissolve the alumina template while leaving the Bi nanowires intact. In the work described above, the template was dissolved using a solution of 45g/l CrO_3 and 5 vol. % H_3PO_4. CrO_3 is known as a very strong oxidizer, and is likely the cause of the thick oxide formed on the nanowires. The 5 vol. % H_3PO_4 alone was found to dissolve the templates, but didn't yield any nanowires. This is because the CrO_3 rapidly forms an oxide on the Bi nanowires which protects them from the H_3PO_4 in the solution (see section 3.2).

It was found through some experimentation that the Bi nanowires could be suc-

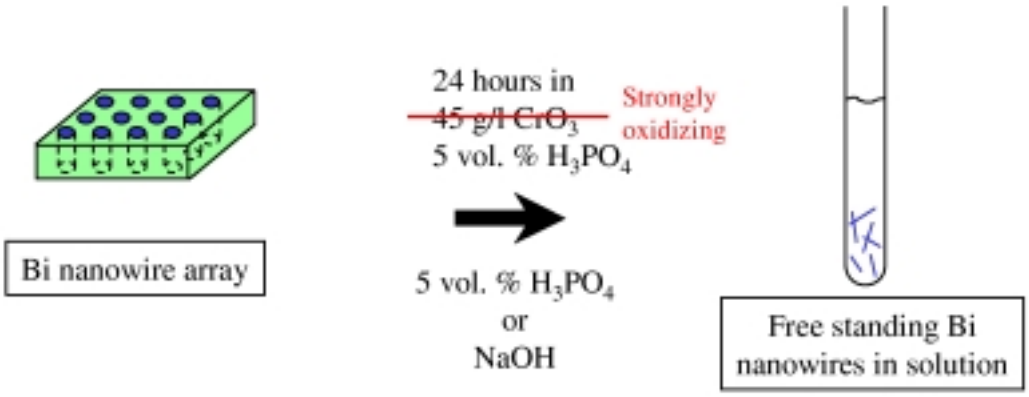

Figure 5-16: Removal of the Bi nanowires from the alumina template.

cessfully removed from the templates without using CrO_3 if the etch time was controlled critically. More specifically, the reaction should be stopped just before the alumina template is completely dissolved and there is still a thin coating of the alumina from the template protecting the nanowires. Templates were successfully dissolved in H_3PO_4 and also in NaOH. Argon was bubbled through the solutions to remove oxygen and to reduce oxidation of the nanowires in the solution. Although the nanowire yield is greatly reduced, the elimination of CrO_3 from the process significantly reduces the oxide thickness on the nanowires. Figure 5-17 shows a Bi nanowire that was removed from the alumina template without using CrO_3 and the TEM image shows the nanowire to have a 2nm oxide. This is significantly less than the 7nm oxide previously observed on nanowires prepared using the solution containing CrO_3 (see figure 3-5). Despite the reduction in oxide thickness, contacts to the nanowires still have a high resistance and non-ohmic behavior.

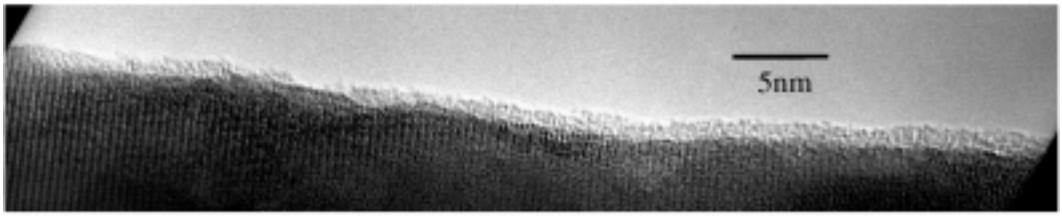

Figure 5-17: HRTEM image of a Bi nanowire that was removed from the alumina template without using CrO_3.

Chapter 6

Measurement of a Single Bismuth Nanowire Inside the Alumina Template

In chapter 5 we found that the chemical and mechanical properties of Bi made it very difficult to improve the surface conditions of the individual Bi nanowires. The very thick oxide found on the Bi nanowires was attributed to the chemical process associated with removing the nanowires from the template. In this chapter we present strategies for measuring a single Bi nanowire inside the alumina template. This approach is appealing because the template is known to protect the nanowires from oxidation.

This chapter is organized as follows. First we start by describing the basic principles of atomic force microscopy (AFM), and how this technique can be applied to measure a single Bi nanowire inside the alumina template. The later sections of this chapter focus on techniques for modifying the surface of the template, which are essential for achieving good electrical contacts to the nanowires.

6.1 Atomic Force Microscopy

The most common use of atomic force microscopy (AFM) is to image surface topography. While the resolution in the plane of the surface (x and y) is limited to the width of the AFM TIP (typically 5-10nm), the height resolution is better than 1nm. It is standard practice to image a single walled carbon nanotube with a diameter of $\sim$ 1nm using AFM. Artifacts in AFM images arise when the asperities on the sample surface are similar in size or smaller than the tip radius. In the case of a valley-like feature whose width is only slightly larger than the tip diameter, the size of the features will appear smaller. This is the case for alumina templates with pore diameters less than 40nm. Because of the finite size of the tip, these pores will appear to be less than 40nm, by roughly the diameter of the tip. In the case of a peak-like feature on the sample surface, the size of the feature will appear larger by roughly the size of the tip. This is the case for single walled carbon nanotubes. Although the true diameter of the nanotube is only 1nm, it will appear much larger because of the finite size of the AFM tip.

Typical AFM tips consist of a silicon cantilever with a very sharp point (5-10nm) at the end (see figure 6-1). The AFM tip is mounted on a platform with piezoelectric elements that can move the tip up and down (the z direction), and in the plane of the sample surface (the x, y direction). A laser, which is reflected off the cantilever, provides the mechanism for detecting when the tip is in contact with the surface. The tip is then vibrated up and down at high frequency (50-100kHz) by the piezoelectric tube. When the tip is near the surface of the sample this vibration is damped by the surface. The amount of damping is measured by the detector, which is fed to a feedback loop to control the height of the tip. As the xy position of the tip is rastered over the sample surface, the height is recorded giving a topographical image of the sample. This is known as *tapping mode* AFM.

Because of the small size of the AFM tip and the precise control over its position, one can envision using a conducting AFM tip to make contact to one of the nanowires in the alumina template, as depicted schematically in figure 6-2. In the tapping

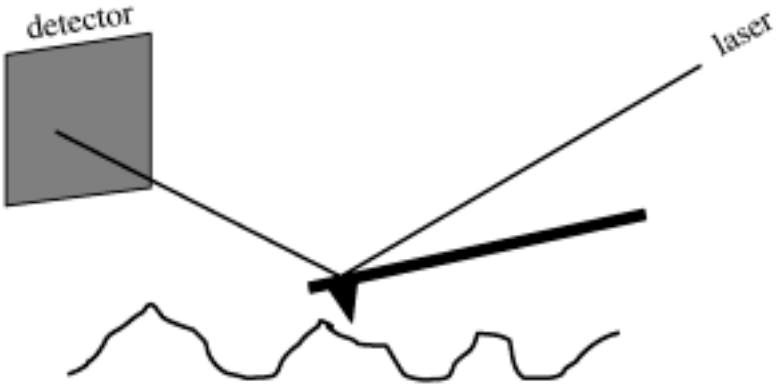

Figure 6-1: Schematic diagram of atomic force microscopy

mode, as the name suggests, the tip is constantly coming in and out of contact with the surface. This is therefore not a good approach for making stable electrical contacts. Instead, the AFM can operated in *contact mode*. As the tip is brought into contact with the surface, in contact mode, the cantilever arm bends slightly causing the reflected laser beam to be deflected. The force of contact can be controlled by increasing or decreasing the desired deflection of the beam. A feedback loop between the detector and the piezo element adjusts the height to maintain a constant deflection of the laser beam, and hence a constant force on the sample over the entire scanned area. This technique has the advantage over the tapping mode for conducting transport measurements since the tip is always in contact with the surface. The disadvantage, however, is that the tip endures more wear in the contact mode than in the tapping mode.

The effect of contact resistance in this measurement can be eliminated by polishing the Bi filled template at an angle to form a wedge shape. The resistance of the nanowires can then be measured as a function of length. The slope of this dependence will then give the resistance per unit length needed for the absolute resistivity. The intercept will give the contact resistance.

Most AFM tips are made of silicon and are insulating. Conducting AFM tips,

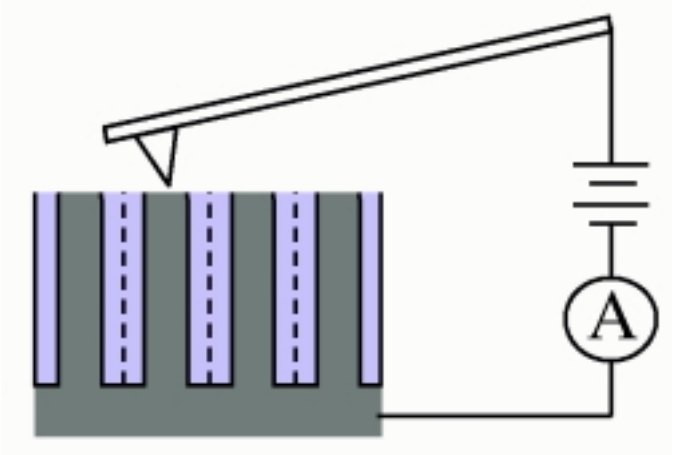

Figure 6-2: Schematic diagram of the Bi nanowires in the template and of the atomic force microscope used to measure the resistance of a single nanowire inside the alumina template.

in which a thin layer of metal is evaporated on the tip, are commercially available. In this work, MESP (magnetic etched silicon probe) tips from Digital Instruments were used. These tips are made for electric force microscopy (EFM) and magnetic force microscopy (MFM), but can also be used for conducting transport experiments. We also made our own conducting AFM tips by coating regular insulating AFM tips (TESP Tapping Mode Etched Silicon Probes from Digital Instruments) with 50$\mathring{A}$ Cr and 100$\mathring{A}$ Au. These tips are an order of magnitude cheaper than the MESP tips, and were found to perform as well as the commercial conducting tips. Some SEM images of a conducting AFM tip are shown in figure 6-3. Good ohmic contact was established using these tips to gold films and also to 2D films of Bi. The resistance of this contact was found to be on the order of 1kΩ and was quite stable for various deflection setpoints.

6.2 Surface Conditions of the Bi Nanowire Arrays

Alumina templates filled with Bi by the pressure injection method have a continuous layer of Bi on one side of the template. This layer of Bi contacts all of the wires in

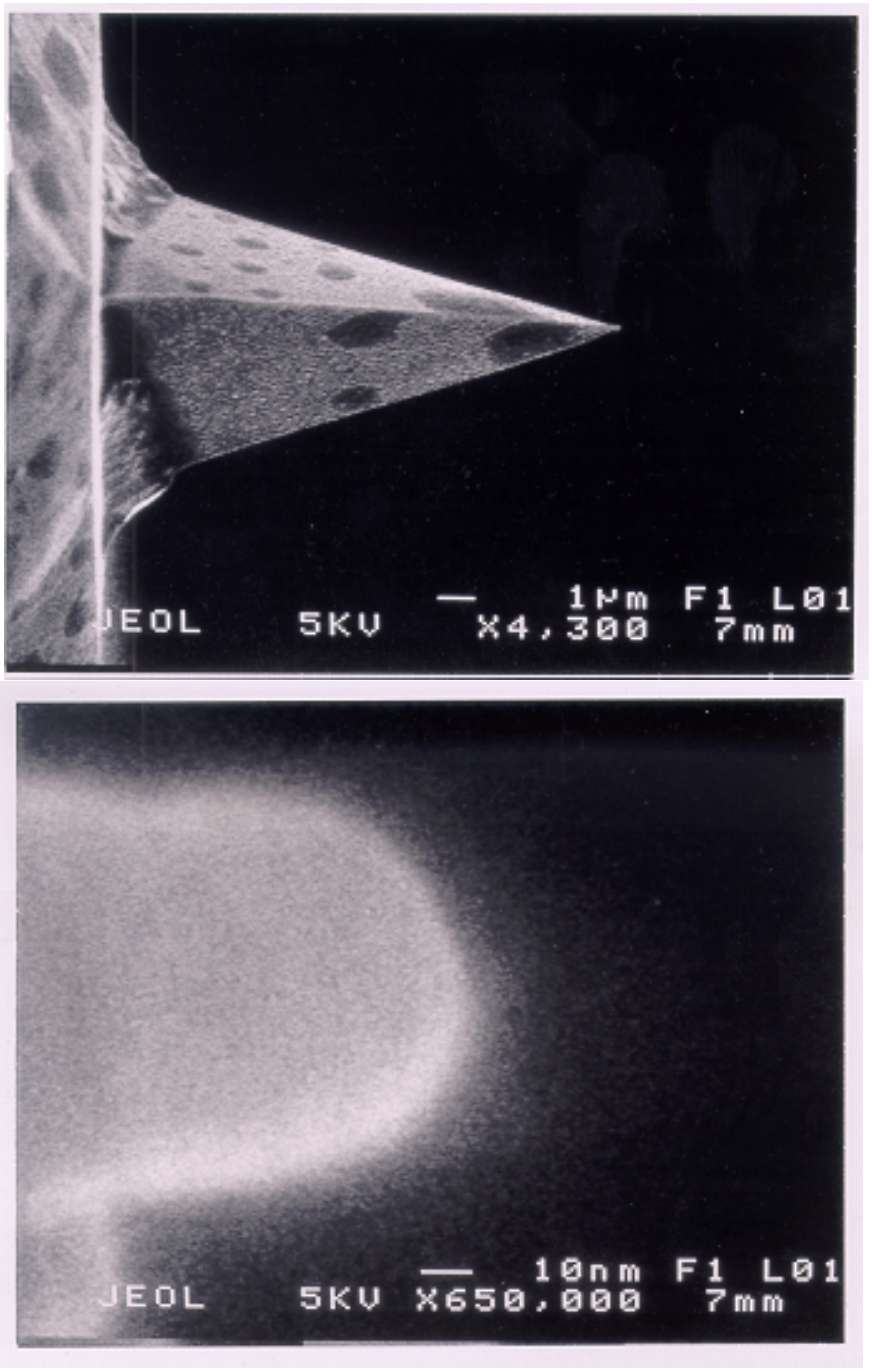

Figure 6-3: SEM images of a conducting AFM tip. The bottom image shows that at high magnification the tip is rounded with a tip radius of ∼30nm.

the template, and serves as a good electrode to one end of the nanowires. The AFM tip, in contact mode, would provide the other electrode to a single nanowire on the other side of the template, as depicted in figure 6-2. The difficulty with this approach is in the wide variability of surface conditions on the top side of the template.

Once the template is filled with Bi and the aluminum substrate is removed (in 0.2M $HgCl_2$) the template has a continuous layer of Bi on the bottom and a barrier layer of alumina on the top of the template. This is shown schematically in figure 6-4. This insulating layer of alumina must be removed in order to make good electrical contact to the nanowires. The thickness of the barrier layer is typically about half of the nanowire spacing in the template. This barrier layer can be dissolved in the 3% vol. H_3PO_4/45g/l CrO_3 solution used to dissolve the template. Figure 6-5 shows an SEM image of the template with a partially dissolved barrier layer. An AFM topographical image of an incompletely dissolved barrier layer is shown in figure 6-6 for a template with a pore diameter of approximately 40nm. At initial glance the circular hills appear to be the Bi nanowires. However, the diameters of these hills are too big to be nanowires. And in fact the surface is found to be insulating. The ridge features in between the hills indicate either the shape in which the aluminum was anodized or inhomogeneous etching of the alumina. The alumina is believed to be more dense in the area between nanowires, and therefore is expected to etch at a slower rate.

6.2.1 Chemical Etching of the Template

The alumina barrier layer can be dissolved in the 3% vol. H_3PO_4/45g/l CrO_3 solution used to dissolve the template. However, this solution also etches the nanowires, and so rather than observing the wires protruding from the template in tree-like structures, the pores appear empty in AFM images. This is in contrast to observations using SEM, where wires slightly recessed in the template can be detected. The disparity between the AFM and SEM images arises because the depth at which the AFM tip can probe the pores of the template is limited to roughly the diameter of the pore. Therefore nanowires that have slightly receded into the pores appear empty in AFM

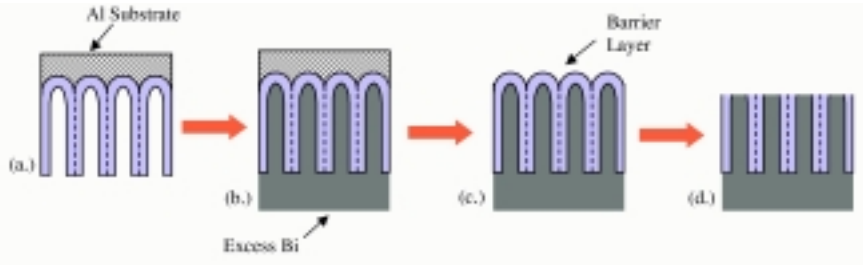

Figure 6-4: Schematic diagram indicating the various processing steps in the preparation of the surface of a Bi filled alumina template. (a.) empty alumina template, (b.) after filling with Bi, (c.) after removing the Al substrate, (d.) after removing the barrier layer.

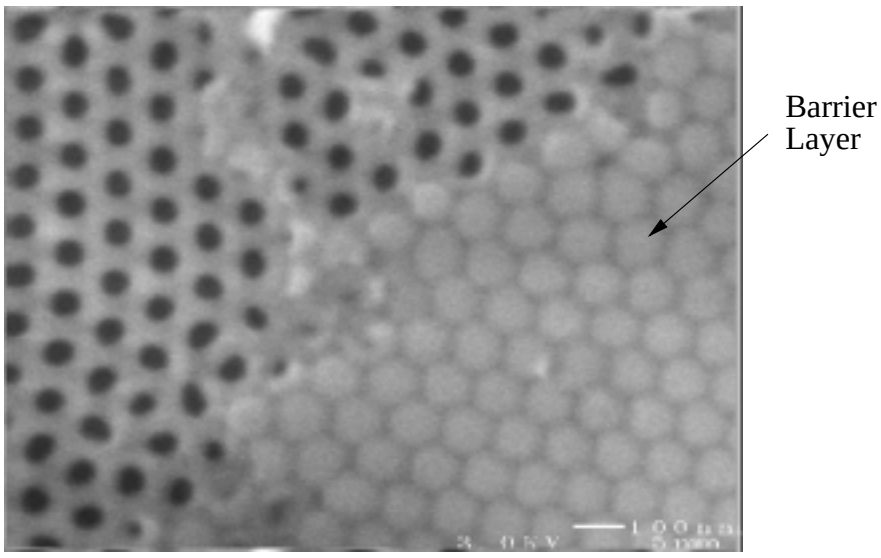

Figure 6-5: SEM image of an alumina template with partially dissolved barrier layer. Image taken from ref [2].

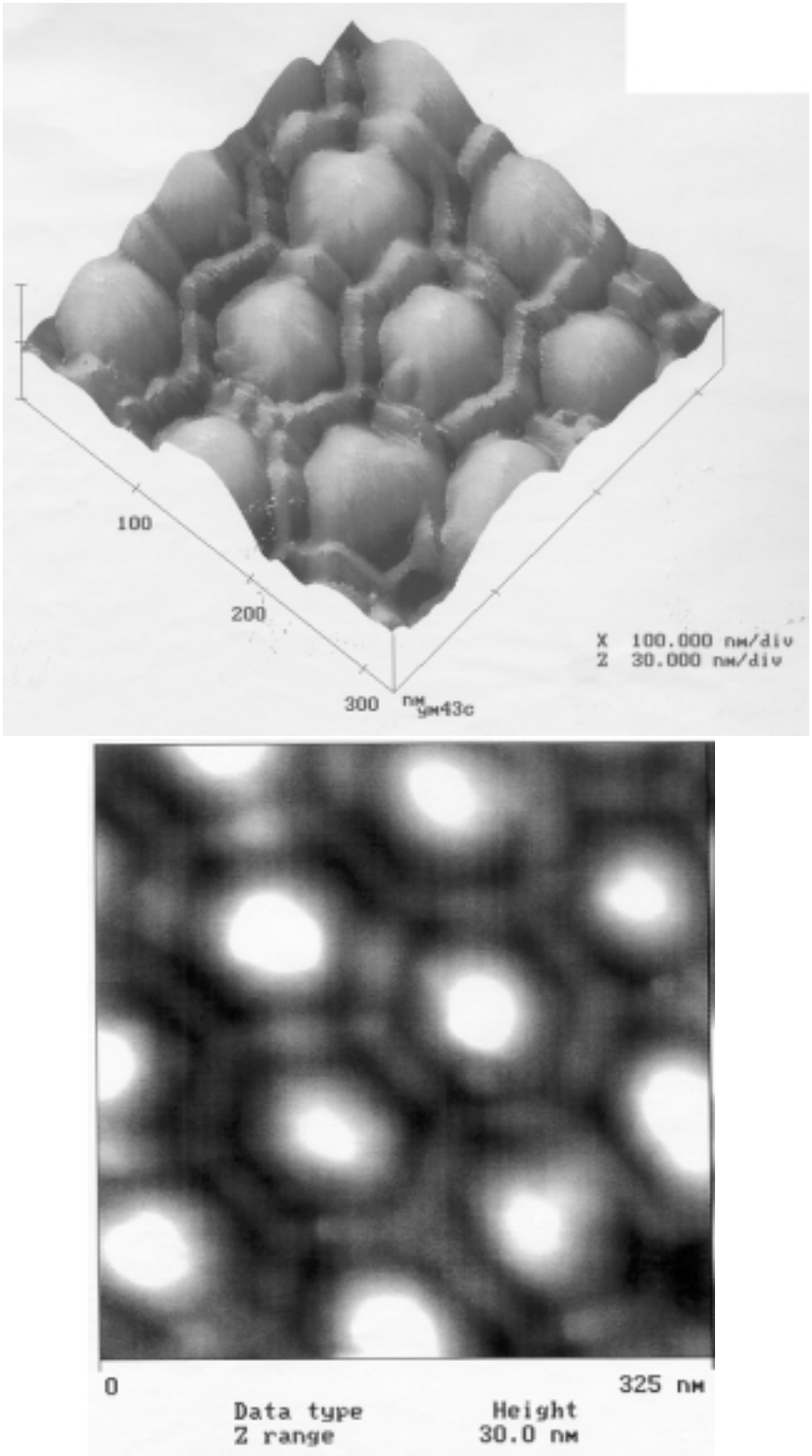

Figure 6-6: Surface plot (top) and Z-plot (bottom) of an AFM image of a 40nm diameter alumina template with barrier layer still intact.

and filled in the SEM.

These difficult surface conditions provide a possible explanation for the very low number of wires contributing to transport in the simple two point measurements. In previous 2-point measurements on Bi nanowire arrays we estimated that only 1 nanowire for every $10000\mu m^2$ was contributing to the transport. Despite the fact that there are a huge number of wires on the surface of the template underneath the contact area ($\sim 1mm^2$), the probability of wires protruding beyond the template to make electrical contact is very improbable. In addition to the unfavorable topography, oxidation may also play a role in the low connectivity of nanowires. The amount of time required to scan a $10000\mu m^2$ area with AFM would be several weeks. This is not feasible when considering the wear on the very thin layer of conducting metal on the AFM as it is dragged over this large area.

6.2.2 Ion Milling of the Template

Another technique that can be used to modify the surface of the template is argon ion milling. Ion milling (or sputtering) is a commonly used technique for preparing surfaces for microscopy. Sputtering at a low angle usually provides means of preparing very flat surfaces. The difficulty in applying this technique to the Bi filled alumina templates lies in the very different materials properties of the alumina and bismuth. Since Bi is a very soft material and the alumina is much harder, the Bi sputters at a faster rate than the alumina, as we saw in section 5.3.3. Thus the Bi recedes into the template. Figure 6-7 shows an AFM image of a template that has been ion milled by a 5kV argon ion beam at $20\mu A$ for 2 hours at an angle of 12 degrees from the surface. From this image we can see that the Bi has again receded into the template and on the surface only empty pores are visible. It is noted that many different areas on this template were surveyed but all yielded topographies similar to that of figure 6-7.

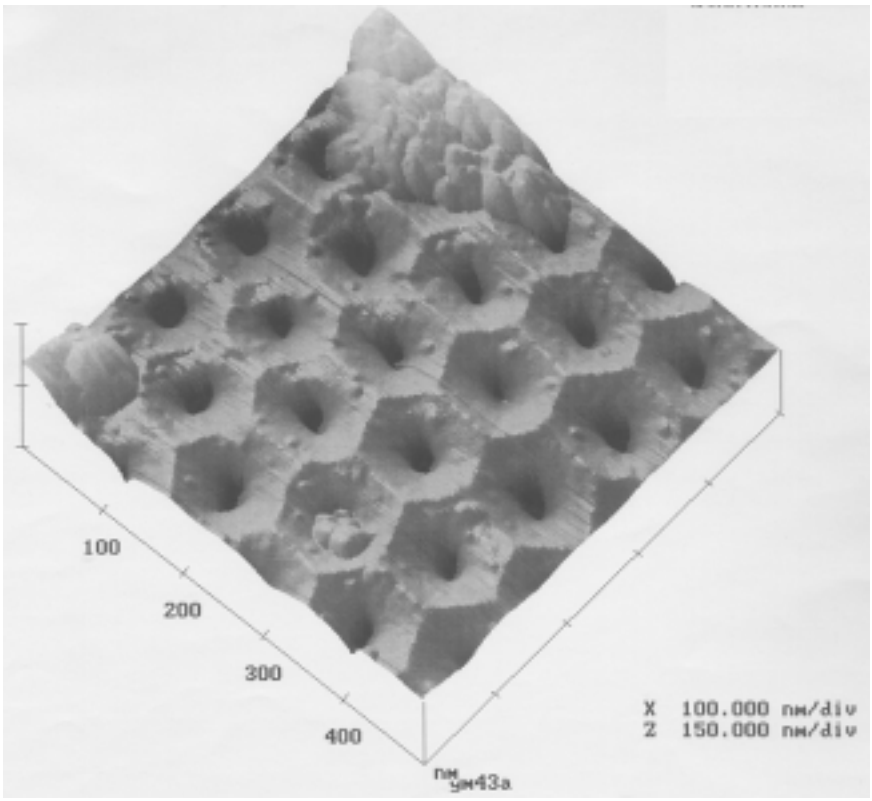

Figure 6-7: AFM image of a Bi filled alumina template after ion milling.

6.2.3 Mechanical Polishing

Perhaps the simplest way to modify the surface of the Bi filled alumina templates is to polish them mechanically. A 50nm polishing suspension was used to polish away a few microns of the template. Figure 6-8 shows AFM and SEM images of a Bi filled alumina template with 70nm diameter pores that was mechanically polished. The SEM image indicates that the pores are filled, whereas the AFM shows unfilled pores. Once again, the Bi was removed at a faster rate than the host alumina, resulting in Bi nanowires that are receded slightly from the template surface. The lines that run diagonally across the image correspond to trenches dug by the polishing suspension.

6.2.4 Mushrooms

A peculiar surface morphology that occurs in the Bi filled alumina templates are the so called *mushroom* structures. The formation of these mushrooms can occur when the Bi expands as it crystallizes, causing the Bi nanowire to break through the alumina barrier layer. Yet another atypical property of bismuth is that its liquid phase is less dense than its solid phase. Mushrooms are less common than the other morphologies discussed above, but are observed in some selected areas of filled templates. An SEM image of these mushroom structures is shown in figure 6-9. Since these mushrooms protrude from the template they may provide a way of contacting the nanowires using an AFM tip.

Figure 6-10 shows mushroom structures observed by AFM. From both SEM and AFM images, the shape of the mushrooms is observed to be irregular. Attempts to measure the resistance between a conducting AFM tip and the bottom of this sample resulted in no observable conduction. This is possibly due to an insulating oxide layer formed on the Bi mushrooms.

The sample with mushrooms was ion milled at various dosages to remove the suspected surface oxide. Ohmic contact was established to the surface of the template after ion milling briefly for 3.5 minutes. The resistance between the AFM tip and the bottom of the sample was found to be 83kΩ. However, the nanowires could not

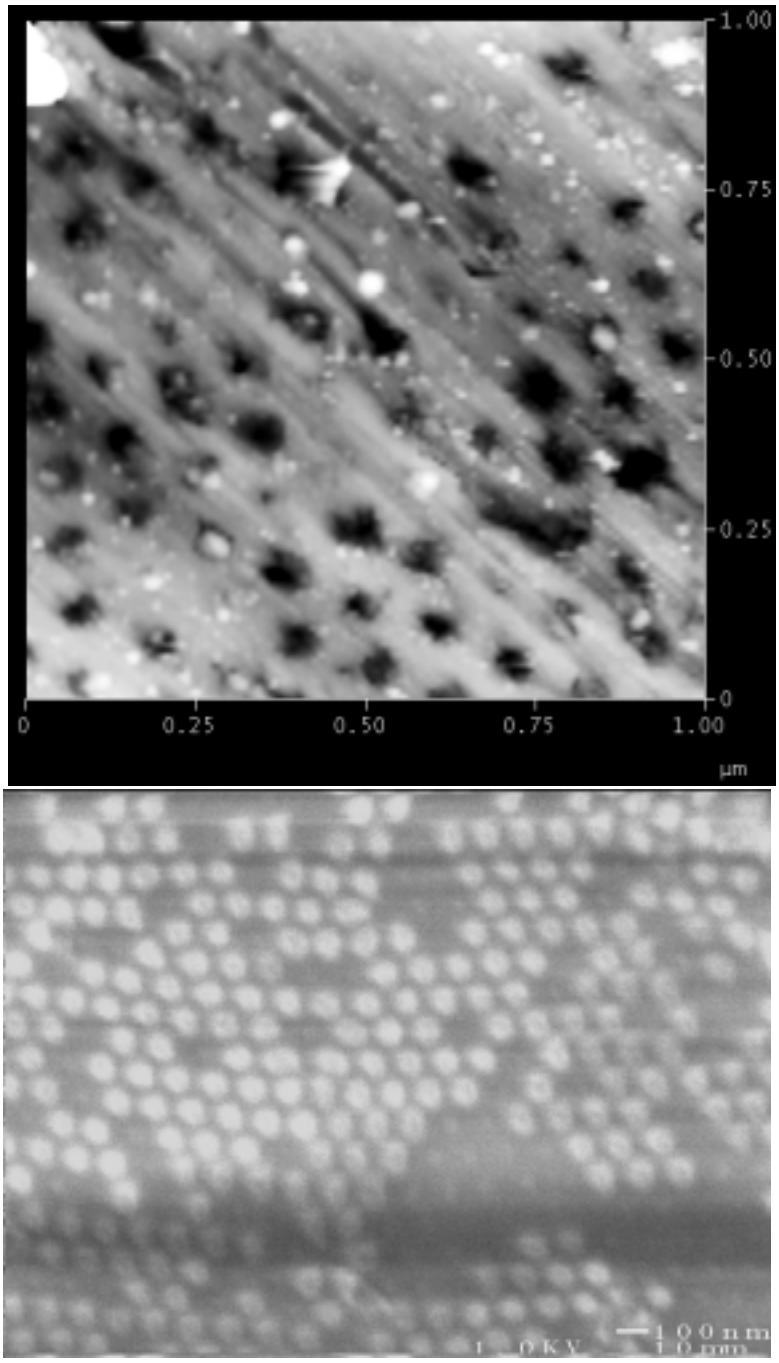

Figure 6-8: AFM topographical image (top) and SEM image (bottom) of a 70nm diameter Bi filled alumina template after mechanical polishing.

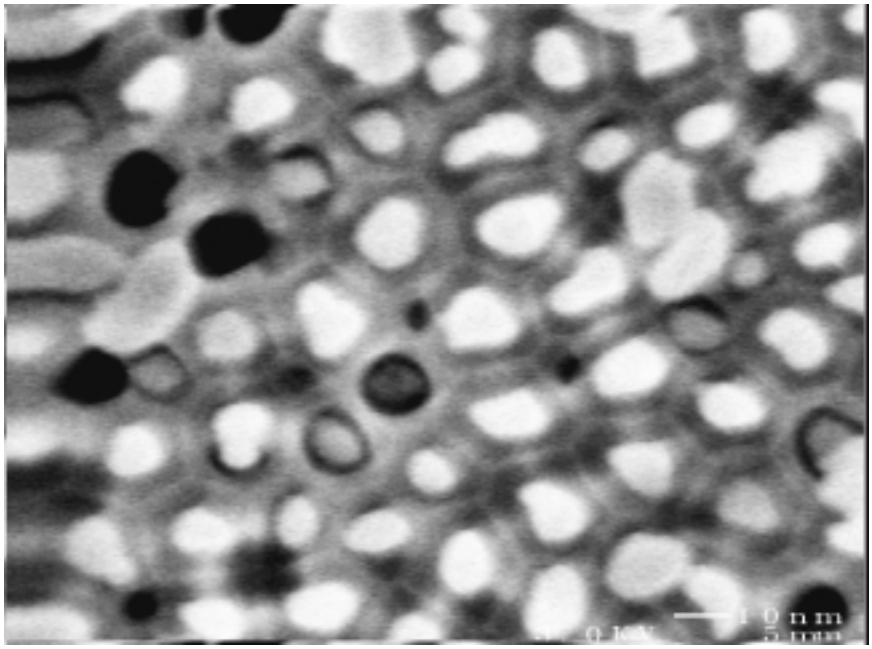

Figure 6-9: SEM image of mushroom-like structures on the surface of a Bi filled alumina template. Image taken from ref [2].

be discerned from the topographical image, shown in figure 6-11. It appears that the ion sputtering has pushed the mushrooms together, forming a thin conducting layer.

6.3 Lithographic Approach to Measuring a Single Nanowire Inside the Template

Another approach to measuring a single nanowire inside an alumina template is to use lithographic processing, rather than AFM, to limit the number of nanowires contributing to transport. Our approach is illustrated in figure 6-12. In this scheme a gold electrode is patterned on top of a Bi filled template, while the rest of the template is covered with an insulating dielectric film. On the bottom of the template there is a continuous film of Bi which ensures good electrical contact on the bottom side of the nanowire. The area of the top contact pad can be systematically decreased until only one or two nanowires are contributing to the transport. With the *resistance* of

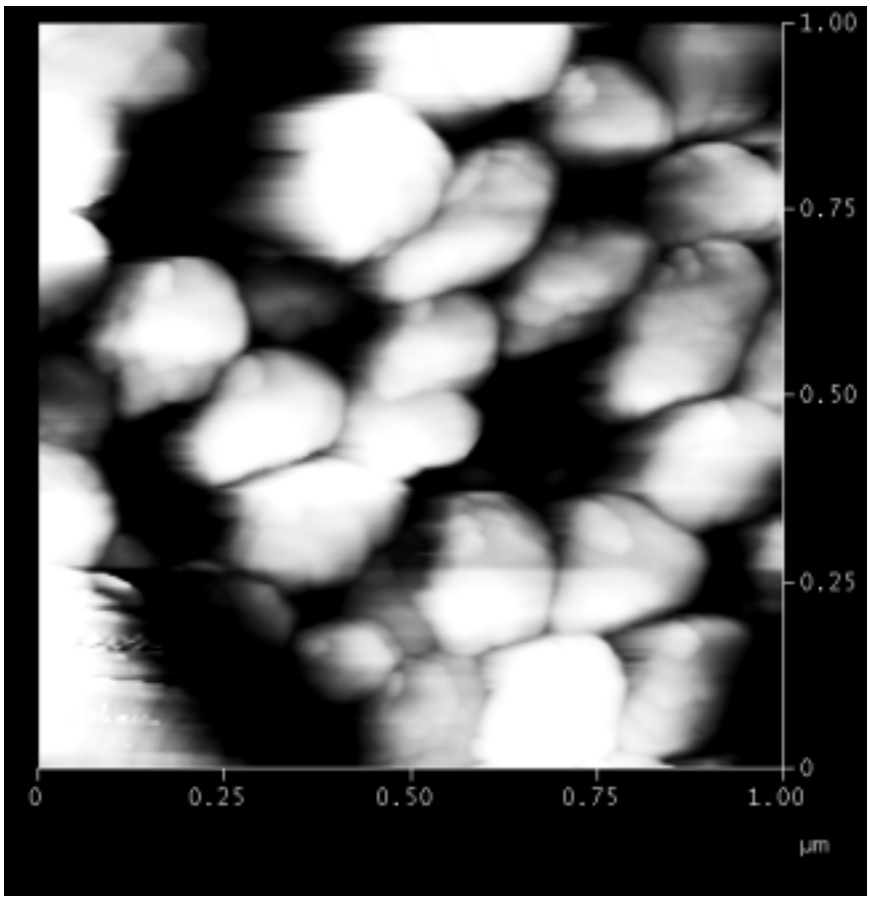

Figure 6-10: AFM image of mushroom-like structures on the surface of a Bi filled alumina template.

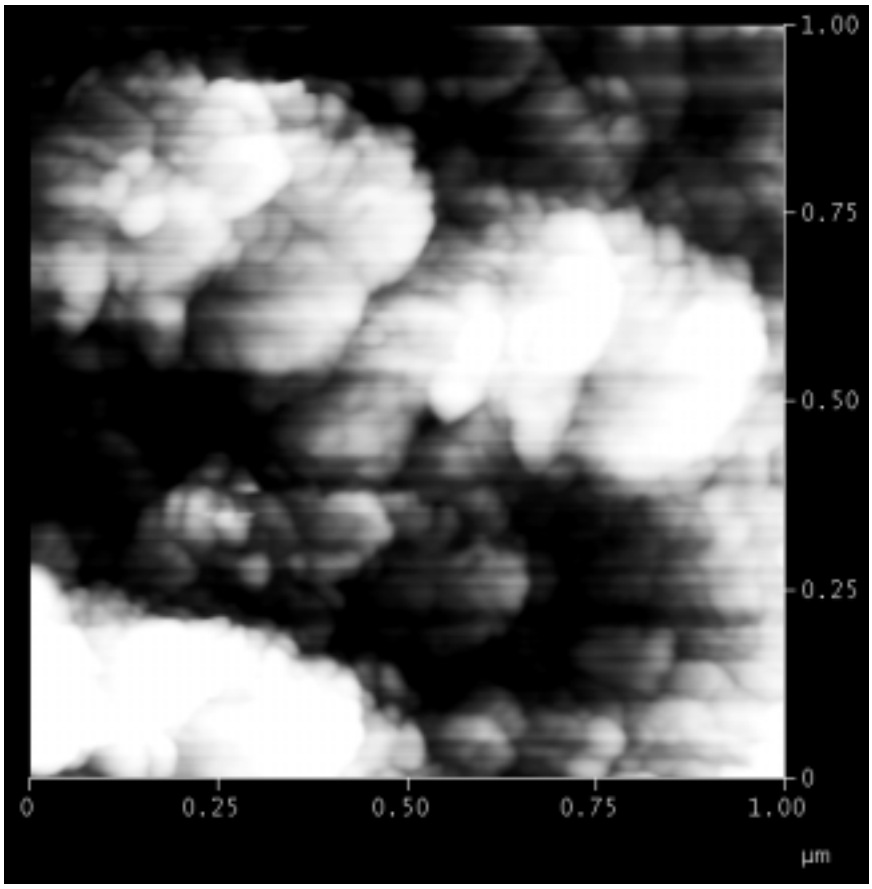

Figure 6-11: AFM image of a sample with mushrooms after brief ion milling.

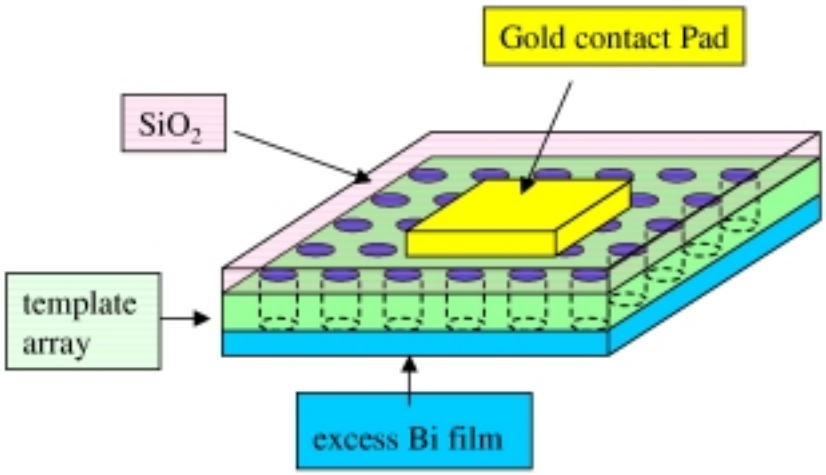

Figure 6-12: Schematic diagram of lithographically defined contact pads on a Bi nanowire array.

one nanowire known, we can determine the *resistivity* by multiplying the *resistance* by the cross-sectional area and dividing by the length of the nanowire.

In previous 2-point measurements on Bi nanowire arrays, where contacts were made by hand using silver paint, we estimated that only 1 nanowire for every $10000\mu m^2$ was contributing to the transport. This extremely low fraction is due to the difficult surface conditions, as described earlier in this chapter, as well as to oxidation of the surface. In figure 6-13 we have patterned a gold contact pad of $60 \times 40\mu m$ on a template with a wire diameter of 50nm. From the close-up image, the filled and unfilled pores of the template can be seen through the contact pad. This is because the thickness of the contact pad is only 100nm, and doesn't fill the pores.

The sample is patterned using electron-beam lithography, where the exposure is done using an SEM (scanning electron microscope). The processing steps are as follows. First an insulating layer of SiO_2 is evaporated everywhere on the top surface of the template. Then PMMA (poly-methyl methacrylate), which will serve as the electron-beam resist, is spun on. The sample is exposed using the SEM by rastering the electron beam over a specified area for a specified amount of time. Once the PMMA is developed, using MIBK (methyl ethyl iso-butyl ketone), the SiO_2 is removed in the area underneath the contact pad using HF (hydroflouric acid). Then

gold is evaporated, using a thin Cr adhesion layer. And finally the remaining PMMA is lifted off using acetone leaving the structure shown in figure 6-12.

In order for this technique to yield reliable results, this approach will require many measurements to assure convergence. After fabricating several devices it was found that the number of nanowires varies significantly for different areas on the template. Therefore convergence is unlikely.

The problems associated with measuring a single Bi nanowire inside the alumina template are reminiscent of the problems of measuring a single free standing nanowire described in chapter 5. In both cases the mechanical as well as the chemical properties of Bi limit the possible modification of the sample surface.

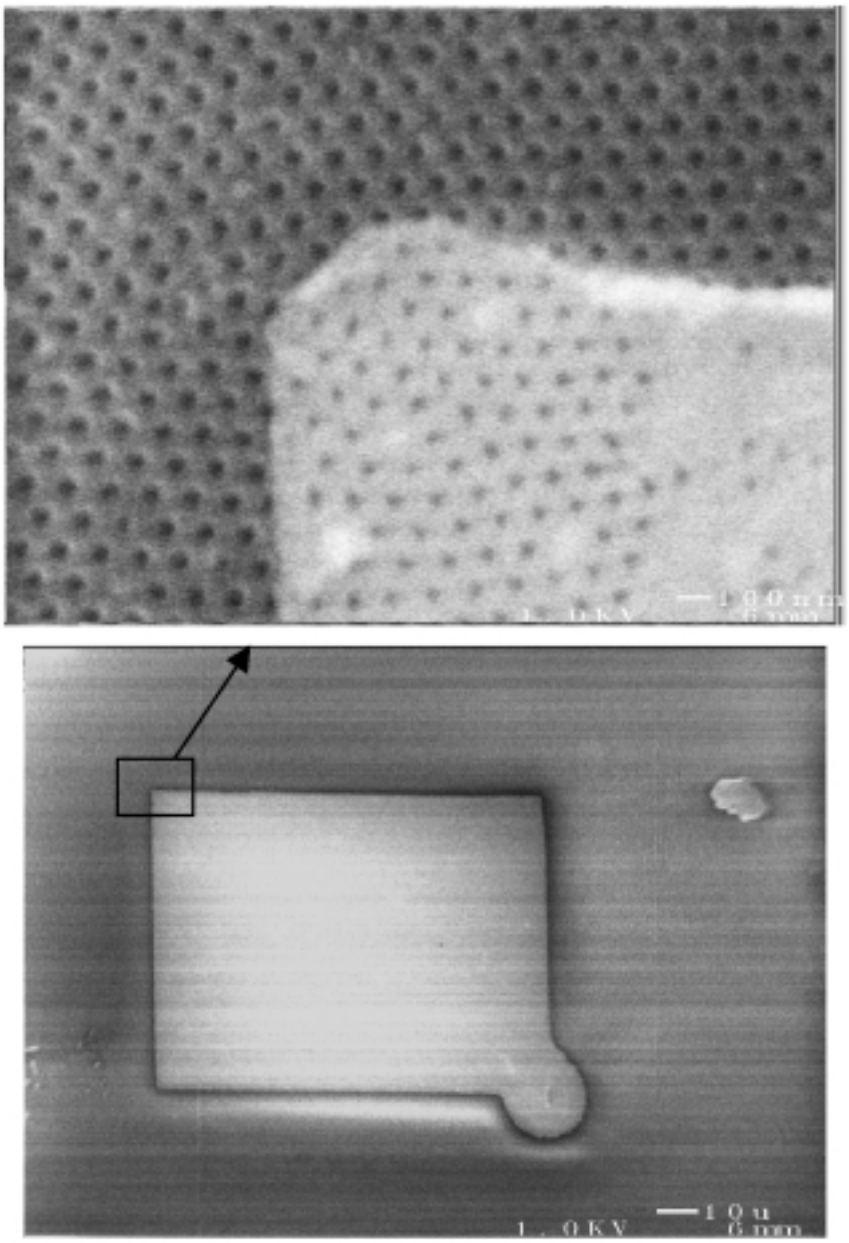

Figure 6-13: SEM images of a $60 \times 40 \mu$m gold contact pad on top of a Bi nanowire array with a wire diameter of 50nm.

Chapter 7

Conclusions and Future Directions

7.1 Conclusions

In spite of the rather unfavorable materials properties of bismuth nanowires, we have established a technique for making ohmic contacts to nanowires with a very thick oxide. Although carried out on Bi, the techniques developed in this thesis are general and can be applied to other nanowire systems. A significant accomplishment of this work is the detailed materials research which provides a comprehensive understanding of the chemical and mechanical properties of the surface of the Bi nanowires on the atomic scale.

State of the art focused ion beam (FIB) techniques were used to first sputter through the oxide and then deposit metal contacts on the nanowires. Combining the FIB techniques with electron beam lithography we achieved contacts stable from 300K to 2K for nanowires less than 100nm in diameter. Resistivity data of nanowires are reported for various wire diameters. The temperature dependence of the nanowire resistivity is understood on the basis of a theoretical model of the quantized electronic band structure and considering wire boundary and grain boundary scattering that is not present in bulk.

Annealing in H_2 and also in NH_3 environments was found to reduce the oxide on the nanowire completely, however the high temperatures required for this high temperature reaction are not compatible with the lithographic techniques. A method

for preventing the burnout of nanowires by electrostatic discharge was also developed. A lithographic scheme for measuring the Seebeck coefficient of a single Bi nanowire was devised. Techniques were also developed for measuring a single Bi nanowire inside the template.

7.2 Future Directions

All of the techniques developed in this work for reducing the oxide to improve the electrical contacts to the nanowires resulted in various other problems that prevented the transport measurement from being carried out reliably. Much of the difficulty is derived from the alumina template synthesis. Although the alumina template assisted fabrication is attractive in that it yields highly crystalline nanowires, many of the difficulties in making good electrical contacts could be avoided if the nanowires were fabricated using a different technique. For instance, if the nanowires were grown in polymeric templates that could be dissolved in neutral solvents, the initial oxidation of the nanowires could be greatly reduced. Also, patterning a Bi nanowire from a thin Bi film using nanolithography would allow one to fabricate contacts from the same continuous film as the nanowire.

Recently, Bi nanowires doped with Te to vary the carrier concentration have been fabricated [2]. Bi nanowires have also been alloyed with Sb [17] to provide an alternate means of varying the energy overlap/bandgap between the electron and valence band. The extent to which the nanowires are in fact doped and alloyed has not yet been determined. A systematic study of the resistivity of these nanowires would provide quantitative information on the doping and alloying of the nanowires.

Segmented nanowires can be fabricated by depositing alternating layers of different materials in the alumina template. This system could be interesting both electrically and thermally, if the two materials have a band offset. In this case one material can be treated as a quantum well and the other as a barrier. If the energy of the electronic wavefunction is below the energy of the barrier material there will be quantum confinement within the well and the wavefunction, which is already

confined in the direction perpendicular to the nanowire, will have a zero-dimensional density of states. Such segmented nanowires would have electronic properties that are very different from any bulk system, and therefore would be interesting for advancing scientific knowledge, as well as for potential device applications.

Bibliography

[1] Y. M. Lin, X. Sun, and M. S. Dresselhaus, Phys. Rev. B **62**, 4610 (2000).

[2] Yu Ming Lin. *Fabrication, Characterization and Theoretical Modeling of Te-doped Bi Nanowire Systems for Thermoelectric Applications.* PhD thesis, Massachusetts Institute of Technology, Department of Electrical Engineering and Computer Science, June 2000.

[3] H. J. Goldsmid, *Thermoelectric Refrigeration* (Plenum, New York, 1964).

[4] D. Schiferl and C. S. Barrett, J. Appl. Crystallogr. **2**, 30 (1969).

[5] H. R. Verdun and H. D. Drew, Phys. Rev. Lett. **33**, 1608 (1974).

[6] R. T. Isaacson and G. A. Williams, Phys. Rev. **185**, 682 (1969).

[7] B. Lax and J. G. Mavroides, in *Solid State Physics*, page 261, (Academic Press, New York, 1960).

[8] J. Heremans and O. P. Hansen, J. Phys. C **12**, 3483 (1979).

[9] M. P. Vecchi and M. S. Dresselhaus, Phys. Rev. B **10**, 771 (1974).

[10] C. F. Gallo, B. S. Chandrasekhar, and P. H. Sutter, J. Appl. Phys. **34**, 144 (1963).

[11] Z. Zhang, D. Gekhtman, M. S. Dresselhaus, and J. Y. Ying, Chem. Mater. **11**, 1659–1665 (1999).

[12] Zhibo B. Zhang. *Fabrication, characterization and transport properties of bismuth nanowire systems.* PhD thesis, Massachusetts Institute of Technology, Department of Physics, February 1999.

[13] J. Heremans, C. M. Thrush, Y.-M. Lin, S. Cronin, Z. Zhang, M. S. Dresselhaus, and J. F. Mansfield, Phys. Rev. B **61**, 2921 (2000).

[14] A. J. Yin, J. Li, A. J. Bennet, and J. M. Xu, Appl. Phys. Lett. **79**, 1039 (2001).

[15] J. Goodberlet, Appl. Phys. Lett. **76**, 667 (2000).

[16] M. R. Black, Y.M. Lin, S. B. Cronin, O. Rabin, and M. S. Dresselhaus, Phys. Rev. B **66**, in press (2002).

[17] Yu-Ming Lin, S. B. Cronin, O. Rabin, Jackie Y. Ying, and M. S. Dresselhaus, Appl. Phys. Lett. **79**, 677–679 (2001).